FINAL REPORT

An EM System With Dynamic Multi-Axis Transmitter and Tensor Gradiometer Receiver

SERDP Project MR-1534

JUNE 2011

David C. George
D.D. Skip Snyder
G & G Sciences Inc.

SERDP
DOD ▪ EPA ▪ DOE

REPORT DOCUMENTATION PAGE

Form Approved
OMB No. 0704-0188

1. REPORT DATE *(DD-MM-YYYY)* June 30, 2011	**2. REPORT TYPE** Final, Technical	**3. DATES COVERED** *(From - To)* 2006 - 2010

4. TITLE AND SUBTITLE
An EM System with Dynamic Multi-Axis transmitter and Tensor Gradiometer Receiver

5a. CONTRACT NUMBER
W912HQ-06-C-0050

5b. GRANT NUMBER

5c. PROGRAM ELEMENT NUMBER

6. AUTHOR(S)
David C. George
D.D. Skip Snyder

5d. PROJECT NUMBER
MM-1534

5e. TASK NUMBER

5f. WORK UNIT NUMBER

7. PERFORMING ORGANIZATION NAME(S) AND ADDRESS(ES)
G&G Sciences Inc.
873 23 Road
Grand Junction, CO 81505

8. PERFORMING ORGANIZATION REPORT NUMBER

9. SPONSORING/MONITORING AGENCY NAME(S) AND ADDRESS(ES)
Strategic Environmental Research and Development Program (SERDP)
901 North Stuart Street
Suite 303
Arlington, VA 22203

10. SPONSOR/MONITOR'S ACRONYM(S)
SERDP

11. SPONSOR/MONITOR'S REPORT NUMBER(S)

12. DISTRIBUTION/AVAILABILITY STATEMENT
Distribution is unlimited.

13. SUPPLEMENTARY NOTES
Snyder Geoscience Inc., 671 Crescent Court, Grand Junction, CO 81505-1071

14. ABSTRACT

The objective of the work was to demonstrate that sensor pairs could be used to adequately approximate the spatial gradients of the vector dB/dt field and to test if the use of sensor differences improved or degraded the quality of data compared to conventional measurements. An array of four, small, three-component sensors was shown to be useful to approximate the spatial gradient tensor when the target was not exceedingly close to the sensors. Computations using the gradient tensor are simpler and faster than conventional computations and offer opportunities for improved target resolution and separation of multiple overlapping signatures. Efficient computations were implemented and tested. Subtracting signals from pairs of sensors decreases signal and also decreases noise, so signal to noise ratio can be better. Measurements showed that differences signals improved signal to noise ratio in situations that are typically encountered in target detection surveys but neither improved nor degraded SNR in situations typically encountered in cued identification and characterization surveys.

15. SUBJECT TERMS
Electromagnetic Induction (EMI); Unexploded ordnance (UXO)

16. SECURITY CLASSIFICATION OF:			**17. LIMITATION OF ABSTRACT**	**18. NUMBER OF PAGES**	**19a. NAME OF RESPONSIBLE PERSON**
a. REPORT	**b. ABSTRACT**	**c. THIS PAGE**			David George
U	U	U	UU	83	**19b. TELEPHONE NUMBER** *(Include area code)* (970) 263 9714

Contents

Acronyms

AOL: Advanced Ordnance Locator

BUD: Berkeley UXO Discriminator

CMRR: Common Mode Rejection Ratio

DAQ: Data Acquisition Computer

EM: Electromagnetic

EMI: Electromagnetic Induction

ESTCP: Environmental Security Technology Certification Program

FWHM: Full Width Half Maximum

ID: Identification

LF: Low Frequency

MM: Metal Mapper

MTADS: Multi-sensor Towed Array Detection System

Rx: Receive

SAM: Sub Audio Magnetic

SERDP: Strategic Environmental Research and Development Program

SNR: Signal-to-Noise Ratio

TEM: Time-domain Electromagnetic induction

Tx: Transmit

UXO: Unexploded Ordnance

VLF: Very Low Frequency

Figures

Acknowledgements

This project was a collaborative effort between G&G Sciences Inc. and Snyder Geoscience. D.D. “Skip” Snyder of Snyder Geoscience was responsible for most of the modeling and computations. David George of G&G Sciences was responsible for all of the hardware development and implementation and most of the experimental measurements.

Funding for this project was provided by the Strategic Environmental Research and Development Program Office. We wish to express our sincere appreciation to Dr. Jeffrey Marqusee, Dr. Anne Andrews, Dr. Herb Nelson, and staff of the SERDP Office for providing support and funding for this project.

Executive Summary

Objective: The original objective of this project was to demonstrate that the measurement of both the vector secondary EMI field and the elements of the tensor gradient using three or more transmitter antenna configurations, would substantially increase the probability of detection of UXO, improve target characterization, and provide a first attempt to differentiate multiple overlapping signatures from UXO targets.

That original objective was refined as the project progressed and as foreseen and unforeseen elements were learned and studied. Two particularly important topics became important.

1. Development of computations and modeling to determine and demonstrate whether measurements made with physical realizable sensors could be used to adequately estimate true gradients and if so, to demonstrate with numerical models whether the gradient method provides improvements in performance when compared to conventional methods.
2. Fabricate components and conduct experiments to verify computations, to demonstrate that useful data can be acquired with realizable hardware, and to collect demonstrative data in real-world situations where mitigating factors are often more complex than can be computed and modeled.

Performance: The project was originally planned in three phases: Phase 1 was to formulate and perform simple model calculations and to perform simple experiments to test whether physically realizable sensors were capable of estimating the tensor gradient and whether those estimates were useful. Phase 2 was to perform more complex computations and modeling, to fabricate multiple sensors and a complete data acquisition system, and to perform more extensive tests. Phase 3 was to perform a full-scale demonstration at one or more sites selected by the SERDP program office. Each phase was separated by a Go/No-go decision for continuing on to the next phase. Work was terminated at the end of Phase 2.

Results:

Early computations showed that finite difference sampling of whole fields, using pairs of whole-field sensors, was sufficient to estimate gradients as long as the distance to the target was more than 2xB, where B is the baseline distance between the pairs of sensors in the gradiometer. Computations showed that other errors, principally signal-to-noise (SNR) considerations, rotation and positioning errors, and sensitivity errors, could be reasonably met with conventional fabrication and electronics.

Later computations showed that, using the gradient tensor method, multiple targets could not be separated unless the targets are separated by a distance of 4 times their burial depth.

The gradient method was shown to be useful for “dipole mapping,” a method used to track magnetic targets approximated by a magnetic dipole. The method was shown to have significant applicability for surveys where it is necessary to track a target as it passes under a sensing array. It is not useful for static or Cued ID surveys where typically a 20-60 second observation is made over a target, and where non-linear computations (inversions) are made to establish the location and characteristics of the target.

Physical experiments showed that a gradient sensor array provides significant improvement in SNR. Noise is reduced more than signal by the action of subtracting signals from closely spaced sensors, so SNR improves. The experiments amplified the expectation that the characterization of SNR in this case is complex. It is function of external factors (environmental EM noise), internal factors (balance and thermal noise generated by electronic amplifiers), and finally bandwidth, where bandwidth is itself a function of data acquisition parameters. Importantly, the experiments showed that SNR is usually improved for wideband observations. But the experiments also showed that SNR is usually not improved for narrower band observations such as those made in cued ID observations (long-time, static, in-place measurements, with wide-window gating functions).

The computations and observations showed that the tensor gradiometer methods could be useful for any survey where data acquisition and computation speeds are important, such as dynamic surveys made for target detection and mapping. At the same time, the computations and observations showed that the tensor gradiometer methods are neither superior nor inferior to conventional methods for surveys where data acquisition and computation speed is less important, such as typical static Cued ID surveys made for target characterization and classification.

1 Project Objectives

Objective: The original objective of this project was to demonstrate that the measurement of both the vector secondary EMI field and the elements of the tensor gradient using three or more transmitter antenna configurations, would substantially increase the probability of detection of UXO, improve target characterization, and provide a first attempt to differentiate multiple overlapping signatures from UXO targets.

That original objective was refined as the project progressed and as foreseen and unforeseen elements were learned and studied. Two sub-parts to the final objective became important parts to this project.

Firstly, gradients must be measured or estimated by physically realizable sensors. True gradients of the magnetic field cannot be measured using the sensors proposed for this project. Gradients must be estimated by observing the field at two or more points where those points are separated by physically reasonable distances (the “baseline”) and where the measurement of the field itself is not exactly a point measurement but is an average of the field value over the area enclosed by the sensor. To sense the magnetic field we used our previously developed and extensively tested small loops that are 10cm square area. With these data we computed simple differences between pairs of sensors. Since estimation of true gradients is sensitive to many factors, one sub-objective became the optimization and selection of a physical configuration for the hardware, together with the development and implementation of numerical techniques to process the data. A related element was to model performance in order to test whether the proposed methods and physical implementations were viable.

Secondly, we knew from the outset that subtraction of two signals from a pair of sensors would reduce the amplitude of the signal with the consequence that it might reduce signal to noise ratio (SNR) and decrease maximum depth of investigation. However, we also knew that subtraction of two signals also reduces noise to the extent that the noise is coherent in both, with the possibility that resulting SNR might actually be improved. Therefore a second objective was to experimentally demonstrate that state-of-the-art sensors are sufficiently sensitive for gradient measurements, and that the resulting data are useful for computations.

2 Background

The basis for this project was the belief, on the part of its principal investigators, that there is a better way to make electromagnetic induction measurements for UXO than the conventional method being used industry wide. The proposed method envisioned sensor pairs measuring a spatial difference in dB/dt instead of individual sensors that sense dB/dt fields. Such measurements approximate a *gradient* (or *difference*) measurement rather than a *whole field* measurement. The belief that this method is better is based in part on parallelism with the passive magnetics method wherein gradient measurements are commonly used for certain surveys, and in part on the belief that the signal-to-noise ratio (SNR) can be improved, rather than decreased, by the differencing of sensor pairs.

This project was funded on June 27, 2006. Work was slow to begin because the principal investigators had other commitments and because funding for the second year of the project was delayed upon request by the program office.

The project was designed with an initial Proof-of-Concept phase with a Go/No-Go decision upon its completion. The first phase constituted the first year’s funding and the first year’s work. This phase consisted of both a computational phase to estimate performance and physical requirements for a gradient sensor, and an experimental phase to test and demonstrate that physical sensors performed as needed. This phase was completed and an interim report was submitted in January 2007. The result was a decision to continue the project into the second phase.

The second phase was to develop and fabricate hardware and software for a full scale system capable of being used for a *local field test*. This local field test was to be a rather complete local test followed by a second Go/No-Go decision for the project. The hardware was fabricated, computational methods were developed, and initial local tests were made. But the results of more extensive modeling showed that the method did not provide the expected improvements in differentiation between multiple targets and overlapping signatures. And results of physical experiments showed that the method did not improve SNR and data quality for the measurements typically used for Cued ID static measurements for target characterization and classification. Contrarily, the experiments showed that the method did improve data quality for dynamic surveys typically used for target detection and mapping. Given that the most important attribute of a new system would be an improvement in target characterization, and that this new system did not offer a high pay-out in that area, a decision was made during a project review in February 2009 to halt further work. Thus we did not complete the complete suite of local field tests, nor did we plan and conduct a full scale demonstration as originally proposed.

3 Materials and Methods

Hardware for this project was both fabricated and borrowed from previous projects. In particular, a complete data acquisition system consisting of processor and transmitter was available, and a sufficient number of 3D *cube* sensors were also available from the Navy's Advanced Ordnance Locator (AOL) system developed previously by G&G Sciences (G&G Sciences Inc., 2008). This left only the following components to be fabricated with funding on this project:

1. An antenna array consisting of transmitter loops and provisions for precise placement of existing receiver loops: We fabricated transmitter loops that were similar in most respects to those used in the AOL system.
2. Preamplifiers and aliasing filters: Designs were optimized for flexibility in placement, for sensor-pair subtraction, for exceptional gain stability, and for best-possible noise performance.

3.1 Antenna Assembly

Pictures of the antenna assembly during and after fabrication are shown in Figure 1. The horizontal axis loops ("Y" and "X" transmitting loops) were similar but improved versions of the horizontal axis transmitter loops fabricated for the AOL system. The Z (vertical axis) loop was fabricated specifically with an open center. This was done to allow placement of sensors

Figure 1: Pictures of the antenna assembly during and after fabrication.

anywhere we chose within that area. A plywood base was installed and marked for placement of sensors. We used plywood because wood has a small thermal coefficient of expansion, thus providing good geometric stability.

3.2 Preamps and Anti-Aliasing Filters

Given that one part of demonstrating performance of the gradient method was to demonstrate that it can reject noise when compared to non-gradient systems, we decided to change the organization of system components for this project. In the AOL system, we placed antialiasing filters on the same circuit board as the preamplifiers and placed that board near the cube sensor, as would be normal for a preamplifier. A block diagram of the AOL configuration is shown in the top part of Figure 2. A potential problem with the AOL configuration is that signal cables within the long umbilical cable between sensors and data acquisition system can pick up noise that is not filtered before reaching the DAQ. For this project, we implemented the method shown in the bottom part of Figure 2. In this method, any out-of-band noise introduced into the umbilical will be filtered before the signal is digitized.

A picture of a cube and receiver and two preamplifiers is shown in Figure 3 and a picture of the antialiasing filters is shown in Figure 4. These circuits were neither fabricated for long-term field use nor for moisture resistance or other environmental difficulties. They were designed to be just sufficient to complete local field tests.

3.3 Integration with AOL Data Acquisition System

A picture of the AOL data acquisition system is shown in Figure 5. The cart was used in essentially the same configuration as it had been used in the AOL system except for the placement of anti-aliasing filters as mentioned above.

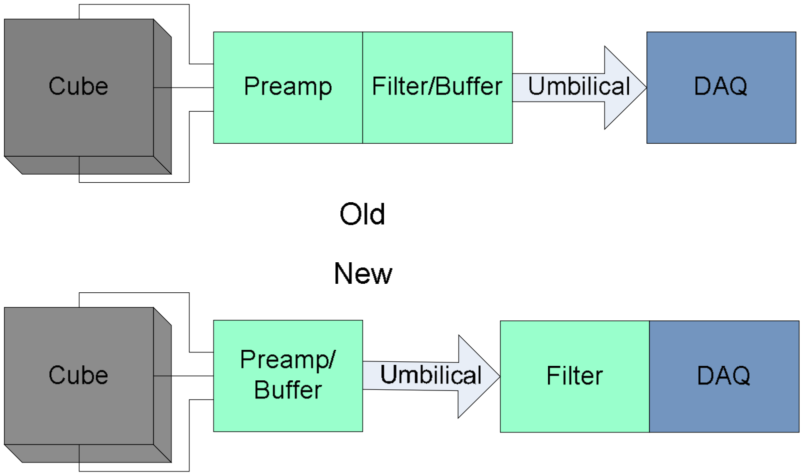

Figure 2: Block diagram showing configuration changes in new system compared to configuration of AOL system.

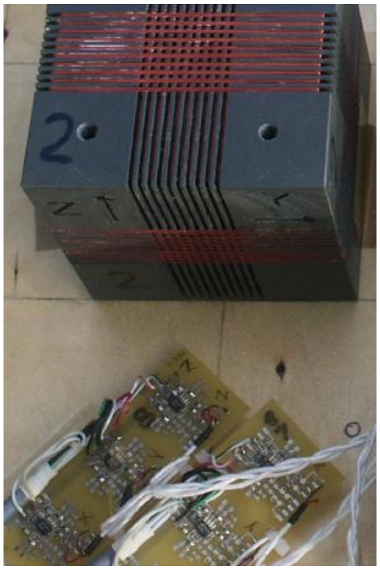

Figure 3: Cube and preamplifier for local tests phase

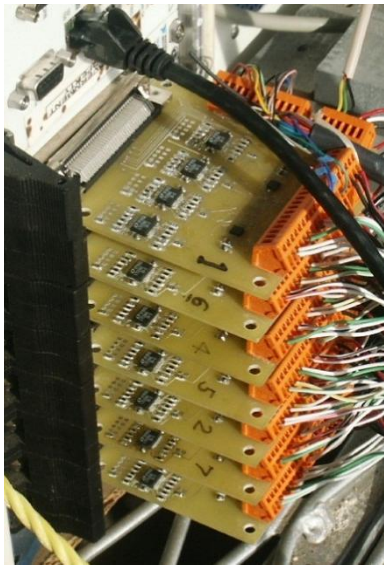

Figure 4: Anti-aliasing filters for local tests phase

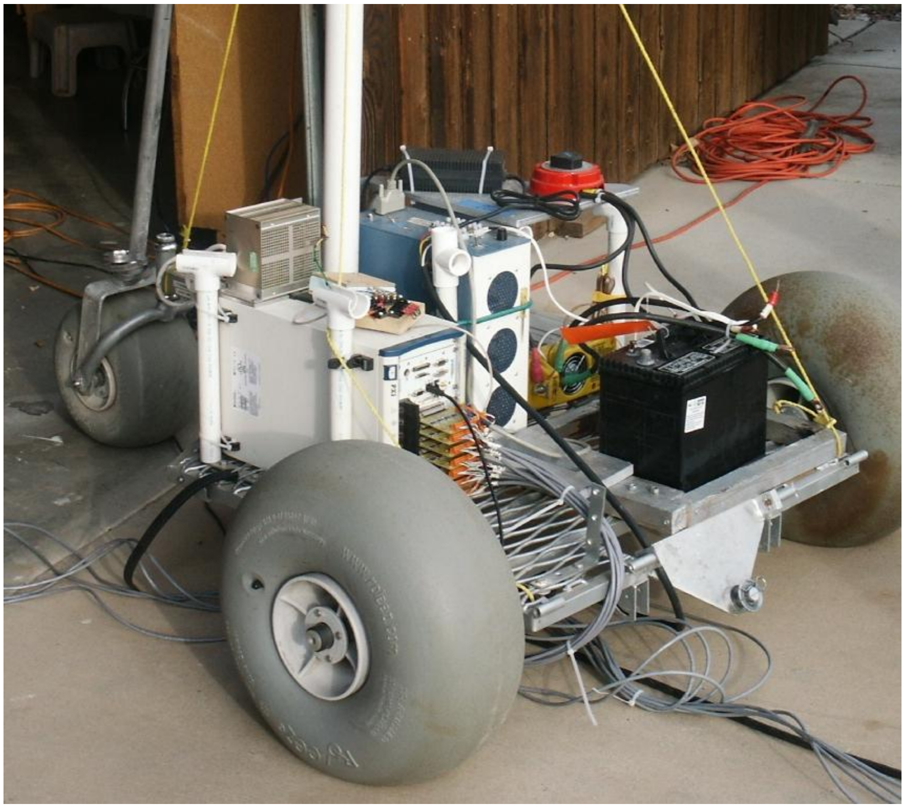

Figure 5: AOL Data acquisition system.

4 Studies, Modeling, and Computations

4.1 Finite Difference Sampling to Estimate Gradients

4.1.1 Finite Difference Sampling of Gradients

In this section we approximate the independent components of the gradient tensor by measuring field differences over a finite distance (h) that we term the gradient ***baseline***. From basic calculus, we know that in the limit as the baseline grows infinitesimally small the difference in the values a continuous function of an independent variable over the baseline is the derivative of the function

$$\frac{df\left(x\right)}{dx} = \lim_{\Delta x \to 0} \frac{f\left(x + \frac{\Delta x}{2}\right) - f\left(x - \frac{\Delta x}{2}\right)}{\Delta x} \tag{1}$$

In the context of our study here, we wish to answer questions about the baseline requirement for gradiometer given the distance (R) from its center point to the target position.

A tensor gradiometer can be constructed by placing tri-axial sensors at each of the four cardinal directions and displaced from the central location by small but finite distance. In Figure 6, we illustrate such a gradiometer. The distance of each sensor from the center location is $h/2$, half the baseline distance of h. In Figure 6, for reasons that will become apparent later in this paper, we have provided for a fifth tri-axial sensor that is used to measure the vector field. With the definition of the baseline (h) together with the radius vector (**R**) directed from the target position to the center of the gradiometer array, we can write a relation for the finite gradient tensor, one that in the limit of small baseline distances converges to the theoretical gradient tensor as written in equation A-5(see Appendix).

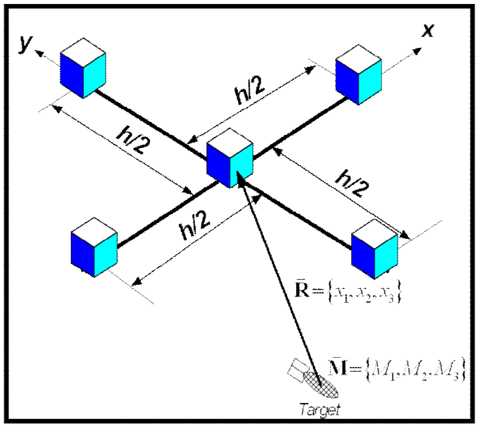

Figure 6: A simple realization of a finite tensor gradiometer. The cubes represent tri-axial field receivers. The center receiver is used to measure the vector field. The other receivers are used in pairs to measure field differences over a baseline distance of h.

$$\Delta B_{i,k} = \mu_0 \frac{G_{ij}\left(x_1 + \frac{h}{2}\delta_{1k}, x_2 + \frac{h}{2}\delta_{2k}, x_3 + \frac{h}{2}\delta_{3k}\right) - G_{ij}\left(x_1 - \frac{h}{2}\delta_{1k}, x_2 - \frac{h}{2}\delta_{2k}, x_3 - \frac{h}{2}\delta_{3k}\right)}{h} M_j \qquad (2)$$

$$\Delta B_{i,k} = \mu_0 \ \Delta_h G_{ij,k}\left(x_1, x_2, x_3\right) M_j$$

In equation 2, we have defined the finite gradient Green's function ($\Delta_h G_{ij,k}$), which is the finite analog to equation (A-4). We state without proof that, in the limit of infinitesimally small *h*, $G_{ij,k} = \lim_{h \to 0} \ \Delta_h G_{ij,k}$. The extent to which this finite gradient tensor represents a good approximation of its theoretical counterpart (equation A-4) determines how well the finite gradiometer array estimates the true gradient. In the rest of this section, we shall try to quantify the errors in the gradient from a finite difference baseline. Secondly, we will estimate the gradient errors that arise as a result of the imperfect realization of a device in which the theory presented thus far presumes perfect alignment.

4.1.1.1 *Finite Gradient Models*

We have used equation 2 (together with equations A-1a and A-3) to estimate the gradient tensor

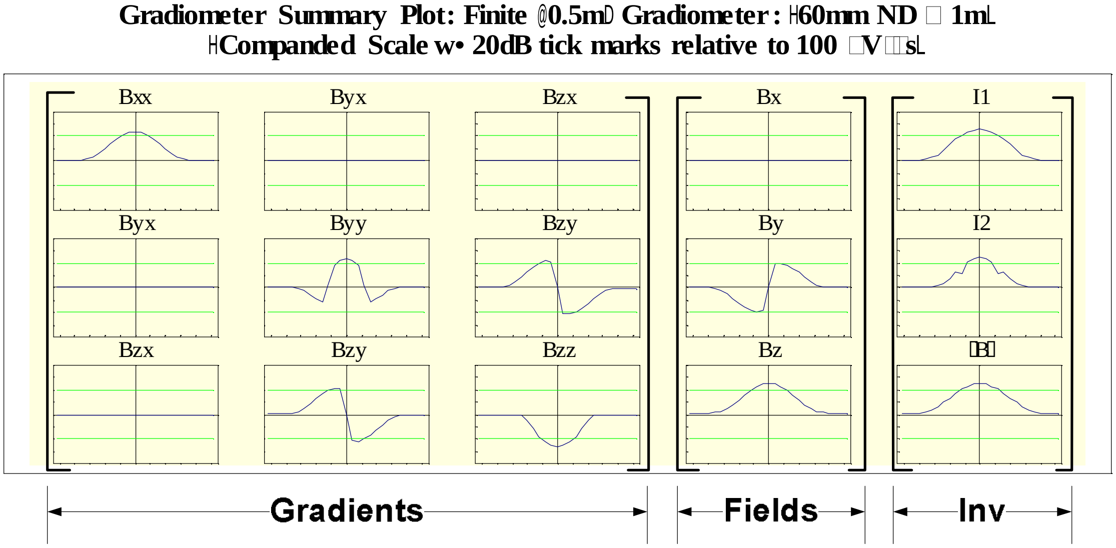

Figure 7: Summary plot showing finite TEM gradient profiles over a 60mm test target buried 1m beneath the plane of the transmitter coil and receiver coils. The profile ranges from –2.6m to + 2.6m. The vertical tick marks represent a companded scale that approximates a bipolar logarithmic scale for signal levels greater than the indicated threshold [100 (µV·µs)]. The green lines represent the 40dB (for each polarity) signal level.

from a standard 60mm target.[1] The sensor array for our computations is shown in Figure 6. In the context of the gradiometer sensor array shown in Figure 6, we evaluate equation 2 only for index values $k=1$ and $k=2$. This is because all sensors lie in a plane (the x-y plane for example) and, therefore we have no way of measuring differences along the coordinate axis perpendicular to the plane of the sensors (i.e., $k=3$ or the z-axis). Excluding the center receiver, which we have included to measure the vector field at the center of the array, we can measure only 6 field differences (i.e., 3 components along 2 orthogonal directions). The other elements of the gradient tensor must be inferred using the fact that the gradient tensor must be symmetrical and its trace[2] must be zero. Figure 7 and Figure 8 are the summary plots corresponding to Figures A-1 and A-2 that were generated using the theoretical gradient relations. We have chosen a baseline length of $h=50cm$**.** This length represents half the depth to the target dipole, a figure generally accepted to be a practical value for the Nyquist sample interval for the magnetic field over a buried magnetic dipole (Reid A. , 1980). Moreover, it approaches the practical limit on the spacing we can accommodate with the constraint of a 10cm cube receiver shape.[3]

It is a problem to summarize errors for curve or map sets such as those shown in Figures A-1, A-2 (See Appendix), Figure 7 and Figure 8. Some gradient and field components are identically 0, while others are bipolar and have zero-crossings. However, notice that the three invariants (I_1, I_2, and |B|) are never 0. So we have chosen to normalize the error difference between the values calculated using the finite gradiometer array and those from the theoretical gradiometer array by the peak value of the invariant I_1. Similarly, we have normalized the differences in the field values by the peak of field magnitude (|B|). These errors are expressed in units of percent.

---

[1] Refer to section A.1.2 for a discussion of the "standard 60mm target.

[2] The trace of a square matrix is defined as the sum of the elements along its main diagonal. Under the assumptions we have made regarding the nature of the induced secondary field, it is a potential field. Therefore, the divergence of the secondary field must vanish (div B_s =0).

[3] Physically, we can configure an array with h=30cm. However, with the edge of receiver coils within 5cm of the center coil there is some question about whether the small fields produced by the currents in the receivers may induce measurable effects in receiver loops in close proximity.

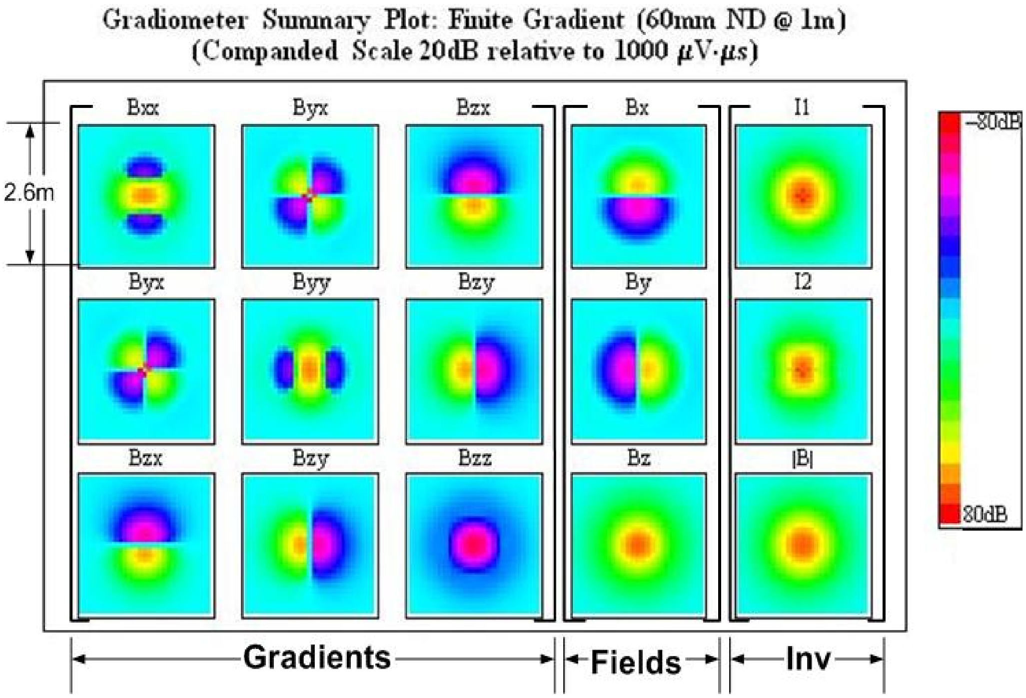

Figure 8: Summary plot showing theoretical TEM gradient maps over a 60mm test target buried 1m beneath the plane of the transmitter coil. The maps cover a 5.2m x 5.2m area centered over the target. The color scale represents the companded values and approximates a bipolar logarithmic scale for signal levels greater than the indicated threshold [100μV·μs].

Using the normalization scheme outlined in the previous paragraph, we have computed errors for the curves and maps corresponding to theoretical and finite gradient modeling for the test case. These errors are summarized for the profile and map cases in Figure 9 and Figure 10 respectively.

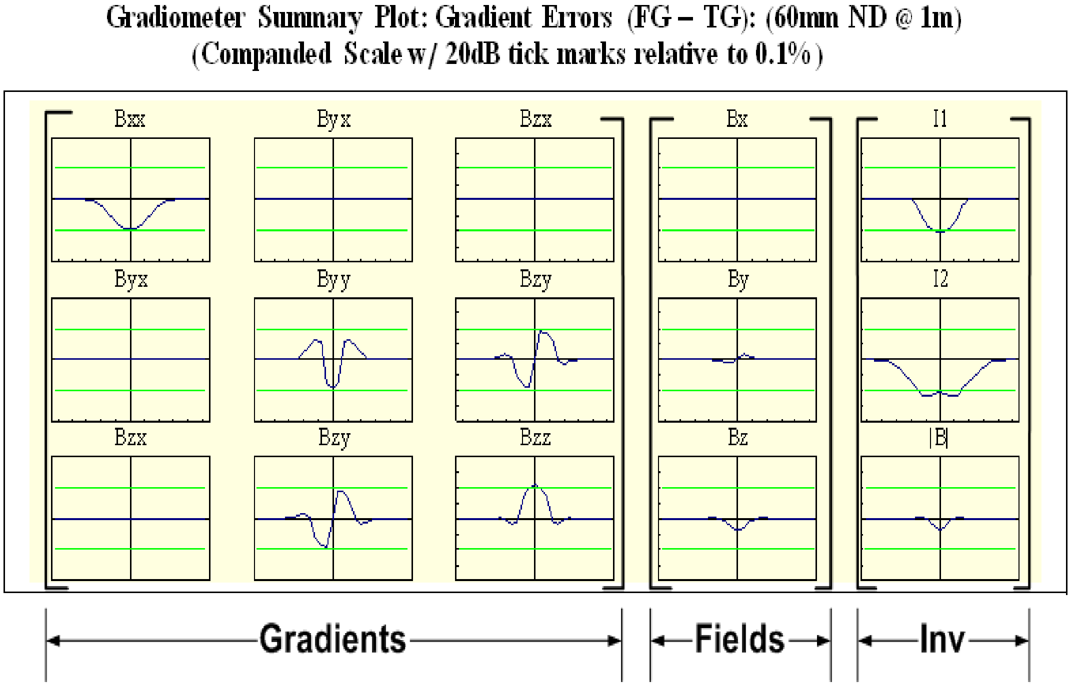

Figure 9: Summary error plot showing gradient errors and field errors for the 60mm test model at 1m depth. The errors, expressed as a percentage of peak value of either I_1 or |B| as appropriate have been companded using the bipolar companding formula in equation A-10. The companding generates a logarithmic scale for the ordinate expressed in units of dB relative to the reference value (0.1% for this case).

The careful reader might wonder why there is a difference between the fields calculated during the theoretical gradient calculations and those we calculate during the finite gradient calculations. If the fields were calculated using the same algorithm, there should be no difference. However, in the interest of keeping the finite gradient modeling as realistic as possible, the modeling software accounts for variations in the secondary field over the finite area (i.e., 10cm x 10cm) of each of the receiver coils. This "nuance" is not included in the algorithm used to calculate the theoretical gradients. Instead, the voltages are calculated using the appropriate field component calculated at the center of each of the receiver coils and then scaled by the appropriate effective area for the coil. It is clear from these results that even small 10cm x 10cm receivers remain "finite" when viewed on the scale of most UXO targets of interest.[4] These errors are small (<1%) and the modeling study we have performed in the sections that follow (particularly Figure I-14) suggest that their effects on interpretation are second order compared with the effect of the finite baseline.

---

[4] The author of this section (Snyder) debated about whether to either exclude the curves/maps for the field components from the summary plots, force the differences to be 0, or show the results. In the end, he decided to report these results since they emphasize the fact that even receivers as small as 10cm x 10cm remain observably finite in the context of UXO detection and classification.

Because it is difficult to quantify the errors in the color maps, Figure 9, which quantifies errors along a centerline profile, is the more instructive figure. As we indicated in the Appendix while discussing Figure A-1, the green horizontal lines are at the 40dB level and represent 10% error (100*0.1%). So the figure shows that we can expect maximum gradient errors on the order of 10% relative to the peak anomalous gradient value. Errors in the field values are irrelevant to this discussion since they relate only to the approximation of the response of a finite loop receiver with point values of the secondary field. However, they are less than 1% and therefore are not a significant contributor to the gradient errors summarized in the Figures. We conclude from these results that high fidelity gradient measurements (e.g., errors of ≤1%) will require baselines of somewhat less than twice the minimum distance to the target.

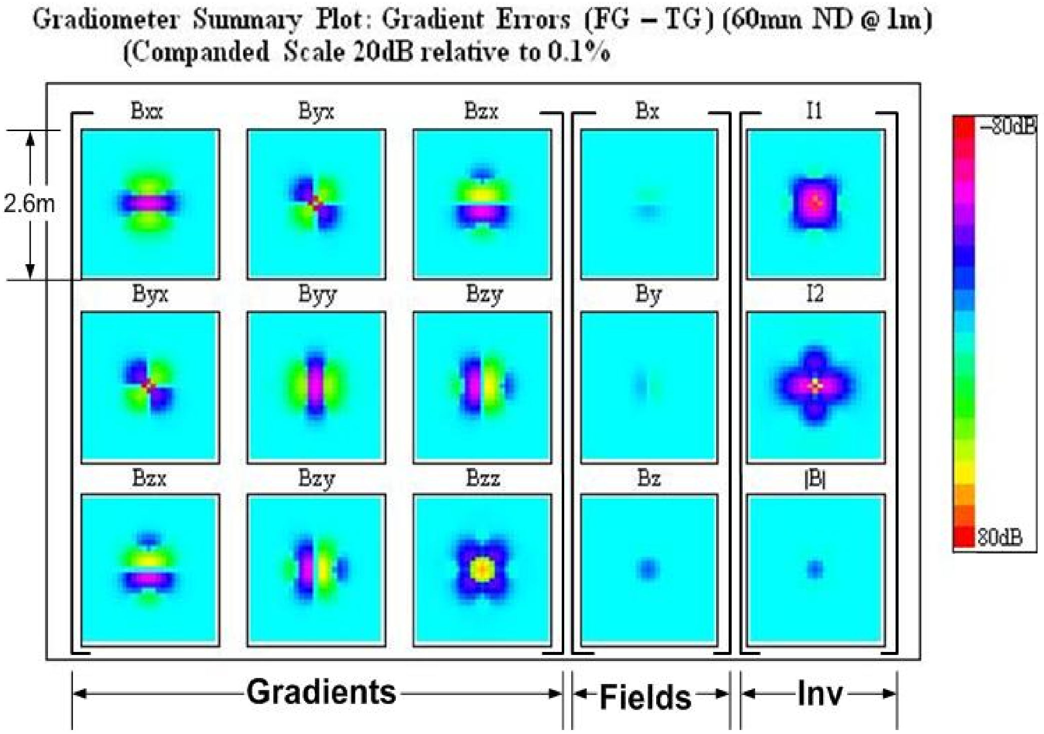

Figure 10: The map view of gradient and field errors corresponding to the profiles summarized in Figure I-4 above.

As a final modeling exercise, we studied the gradient error as we varied target depth directly beneath the sensor array. Since the profiles of gradient components with depth for those components that are non-zero exhibit a monotonic attenuation of response with target depth, we have dispensed with showing the actual response and show here only the errors as a percentage of the theoretical value companded onto a logarithmic scale. In Figure 11, we have again summarized the plots in the same manner as we have in the previous Figures. However, in this case we have set the depth on the vertical axis while the bipolar companded error is plotted horizontally. We have located vertical green lines on each plot to indicate the 40dB (10%) error level for each polarity. The horizontal red line indicates the depth of 1m, which is twice the length of the gradiometer baseline. Figure I-6 confirms in a slightly different way that we can expect gradient errors of approximately 10% for dipole targets at a range of twice the gradiometer baseline.

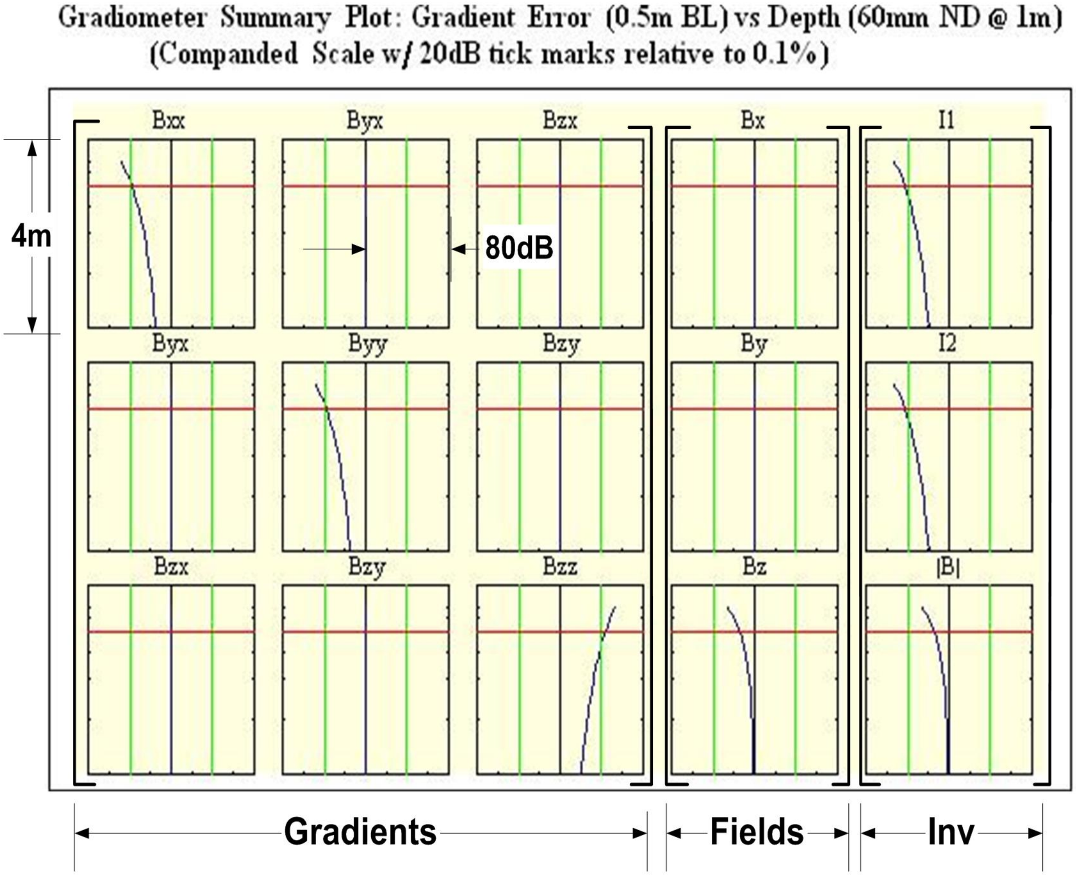

Figure 11: Error summary for finite gradient measurements as a function of target depth. The vertical scale is depth, while the horizontal scale for each plot approximates a logarithmic (dB) scale for a bipolar signal. The vertical green lines represent 10% error. The horizontal redline is at the depth of 1m.

4.1.1.2 *Balance and Alignment Errors*

The foregoing discussion deals only with the fact that we cannot accurately measure a magnetic gradient arising from a dipole source with a finite baseline gradiometer unless the source is located at a range of perhaps as large as four times the baseline. Apart from the length of the baseline, however, the accurate measurement of field differences also depends on precise balance and alignment of the individual sensor cubes. The realization of a tensor gradiometer system from four individual tri-axial sensors is subject to numerous sources of systematic error, the most important of which are (Bracken & Brown, 2006):

1. **Orthogonality Error:** The axes of the individual sensors are not precisely mutually orthogonal.

2. **Sensor Position and Alignment:** The relative position and alignment of the four-sensor array is subject to errors in their absolute position and alignment.
3. **Sensor Sensitivity:** Although designed to have identical sensitivities, each of the 12 sensor coils comprising the four tri-axial cube receivers has a slightly different sensitivity. Each coil will in fact have a different sensitivity due to mechanical and electronic tolerances. Moreover, these sensitivities will change with temperature as a result of thermal expansion and the temperature coefficients of electronic components comprising the coil preamplifiers.

4.1.2 Noise, Gradient Errors, and Interpretation

To this point, we have simply examined the difference between an ideal point gradiometer and one implemented by measuring finite spatial differences with small but observably finite loop sensors. Using a target buried at a depth of twice the finite gradiometer baseline, we have determined that approximating the gradient with a divided difference of the field values along a directed baseline can result in errors a large as 10% of the corresponding theoretical gradient value. In this section, we ask two slightly different questions. First, we want an estimate of the gradient noise levels that we can tolerate in our gradient measurements while retaining the ability to make useful estimates, in particular, of target position. Secondly, we want to determine the point at which we must abandon potentially useful (and simpler) interpretation techniques that involve the true gradient and return to more complicated interpretation methods that consider the finite geometry of the sensor array.

4.1.2.1 *Gradient Noise*

The perfectly balanced and aligned finite gradiometer will be insensitive to EMI noise (i.e., infinite common mode rejection). However, to the extent that our gradiometer is afflicted with the three major imperfections identified in section 4.1.1.2, some fraction of the ambient EMI noise will leak into the difference measurements and appear as (systematic) gradient noise. However, we expect that the noise amplitude will be significantly attenuated. For the purpose of this study, we will call this ability to attenuate the ambient EMI the common mode rejection ratio (CMRR). We know from the experience of others that, with care, it is practical to expect as much as 30dB (Becker, 2006).

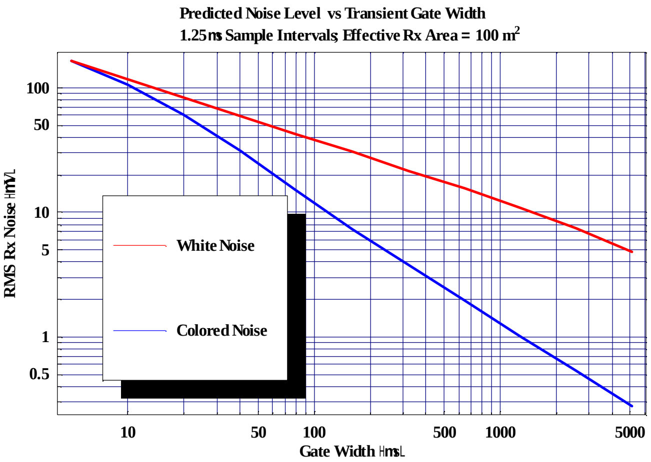

Figure 12: Predicted EMI noise level as a function of transient gate width. The red curve for white noise falls off with a slope of –1/2. The blue curve is for a colored noise model based on average curves published by Meloy (Meloy).

To study how this gradient noise can degrade interpretations, we have generated a few noisy data sets using the standard target and profile discussed in the Appendix. The noise-free data are summarized in Figure A-1. We first estimate the level of ambient EMI noise that might be present in our 500 μs detection gate. Based on an average spectra published by Meloy (Meloy), we have developed a colored noise model that we use to predict the order of magnitude of the ambient EMI noise as a function of gate width. Figure 12 shows how the noise level is attenuated by a simple gated average. The red curve is for white noise and falls off at the predicted rate of $1/\sqrt{t_w}$ where t_w is the gate width. This model shows that we can expect the EMI ambient noise levels to be on the order of a few microvolts or, equivalently, the integrated gate noise to be on the order of 1000 μV• μs. Noise levels can be further reduced by stacking if measurements can be taken under static conditions. In any case, this noise level is consistent with the AOL data we have acquired on demonstrations at Blossom Point and Indian Head (Snyder & George, Deployment of a Dual-Mode (EM and Magnetic) System for Detection and Classification of UXO at Blossom Point, MD, 2004).

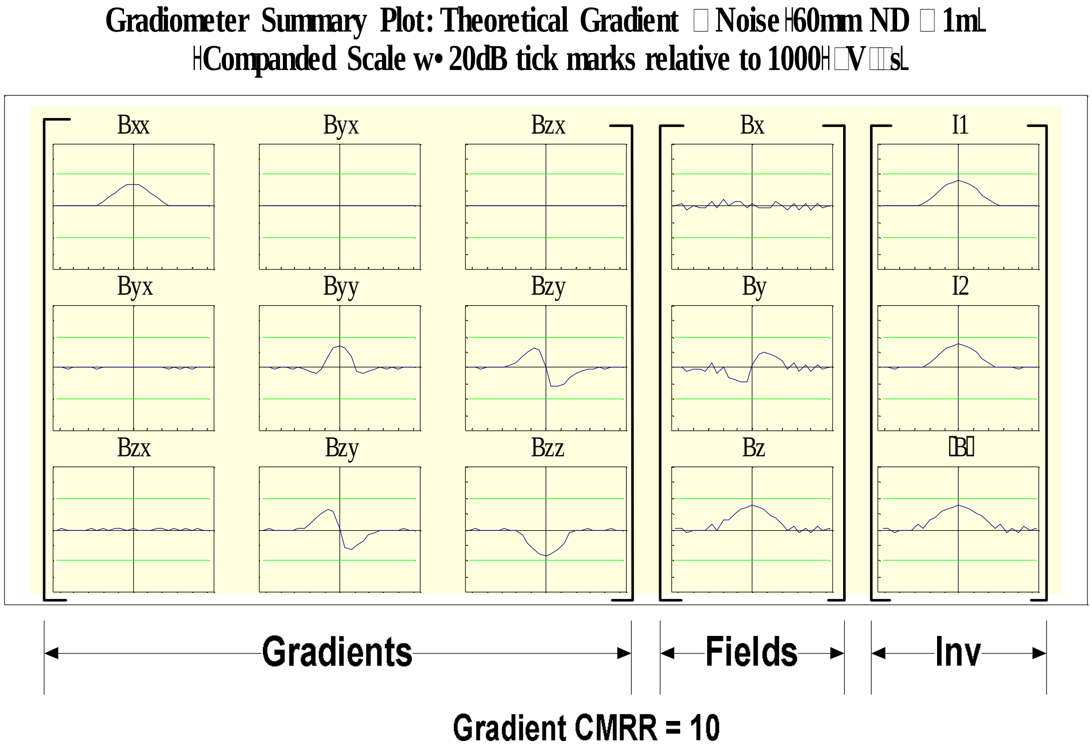

Figure 13: Gradient summary plot showing a centerline profile over a 60mm target buried at depth 1m. Gaussian random noise having a standard deviation of 1000 μV·μs has been added to the field components. The gradient noise is set to the field noise attenuated by the CMRR=10.

We generated noisy gradient data by adding Gaussian random noise with a standard deviation of 1000 μV• μs to the theoretical gradient data summarized in Figure A-1. To arrive at a noise level for the gradient components, we assumed a CMRR for attenuating the noise before adding it to the gradient data. Thus, a noisy model with CMRR=100 signifies that noise of 10 μV• μs was added to the gradient components. In Figure 13, we summarize profile data for the standard target model assuming that gradient measurements have a CMRR=10.

In Figure 13, there is obvious noise in the field components. Less obvious is the corresponding noise in the gradient components because of the CMRR for a pair of sensors. Note that we have changed the companding reference value to 1000 μV-μs so that now, the horizontal green lines (at 40dB relative to 1000 μV-μs) give us an estimate of the SNR for the field values. In this case, the peak SNR for the field components is 20-30dB, which is at the threshold required for acceptable physics-based interpretation. We have plotted the gradients using the same noise threshold. However, the noise is actually 32dB lower and hence the peak gradient SNR actually exceeds 40dB.

4.1.2.2 *Dipole Tracking Interpretations*

The ability to measure the tensor gradient together with the corresponding vector field affords the opportunity for a simplified interpretation. Termed ***dipole tracking*** by Wynn, et. al. (Wynn, Frahm, Carroll, Clark, Wellhoner, & Wynn, 1975), the method as we apply it here is based on two different relations. As noted by Wynn, we can combine equations (A-4) and (A-5) to obtain the following:

$$\begin{aligned} B^s_{i,k} = \frac{\partial B_i}{\partial x_k} &= \mu_0 \left[\frac{3M_j}{4\pi R^4}\right]\left(\delta_{ik}n_j + \delta_{jk}n_i + \delta_{ij}n_k - 5n_i n_j n_k\right) \\ &= \mu_0 M'_j \left(\delta_{ik}n_j + \delta_{jk}n_i + \delta_{ij}n_k - 5n_i n_j n_k\right) \\ M'_j &= \left[\frac{3M_j}{4\pi R^4}\right] \end{aligned} \tag{3}$$

In equation 3, we have introduced the vector *M'* , called the ***reduced moment***. The equation shows that the gradient tensor, which has 5 independent elements, is a non-linear function of 5 independent variables (i.e., 3 components of the reduced moment *M'*, and 2 elements of the unit vector *n* that indicates the direction to the target). We refer the reader back to Wynn, et. al. for the details of the analytic solution of equation 3. Suffice it to say here that there is an analytic solution to the equation that yields values for the unit vector. There is one slight complication with the solution proposed by Wynn. It involves the calculation of the roots of a quartic polynomial and therefore there are, in general, 4 unique solutions. Simple screening for solutions that lie in the lower half-space are sufficient to eliminate 2 of the solutions. However, there remains a “ghost” solution that is paired with the real solution that sometimes cannot easily be eliminated.

Having found the direction to the target together with its reduced moment, we need only to calculate the range value *R* to obtain the complete solution. Finding *R* requires an additional piece of information. We get that information by measuring one or more of the components of the secondary magnetic field. There are several ways to solve for *R* from the field vector *B*. We use the Euler relation (Thompson, EULDPH: A new technique for making computer assisted depth estimates from magnetic data, 1982), a well known relationship between the gradient and the corresponding magnetic field that is often applied in the detection and interpretation of passive magnetic anomalies. Using the nomenclature we have introduced in this report, the Euler relationship relating the tensor gradient to the corresponding field can be written as

$$n_k B^s_{i,k} = -\frac{3}{R} B^s_i \tag{4}$$

Each of the 3 elements in equation 4 provides a relationship between the range value R and a ratio of a component of the secondary magnetic field to the corresponding directional gradient of that field component according to the equation

$$R = -3\frac{B^s_i}{n_k B^s_{i,k}} \quad \text{(no implied sum on index } i\text{)} \tag{4a}$$

The term ***dipole tracking*** as we apply it here consists of the process of solving equation 3 and then using Euler's relation (4a) together with n_i and B^s to locate the dipole. In Figure 14, we show the results of applying this process to the noise-free gradient profile data that we summarized in Figure A-1. As one might expect, the method yields the correct solution for the target position at each of 27 field points along the profile. The addition blue/red vectors that arise from field points in the center of the profile represent the ghost solutions arising from the analytic solution. These solutions were not screened out with the simplified screening inequality constraints that we applied.[5]

The green ellipse in the figure represents a distorted circle with a radius of 10cm. In this particular case, there are 28 solutions that fall within a sphere of radius 1cm.[6]

We have applied the dipole tracking methodology to 5 noise-corrupted data sets similar to that summarized in Figure 13. In these data sets, we have used the CMRR as the parameter that allows varying the amount of noise that is allowed to "leak" into the gradient

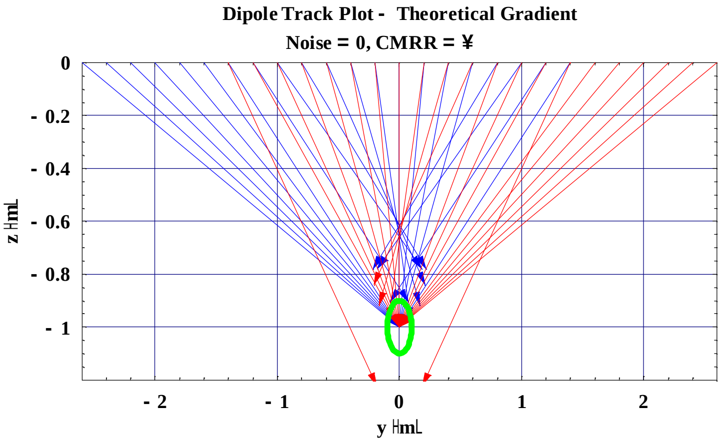

Figure 14: Dipole tracking plot showing feasible target position solutions along a 27-pt profile. The data used were calculated for from theoretical gradient and field relations with no noise added. The blue and red vectors where arising from a common field point represent the actual and "ghost" solution provided from the analytic solution of equation 3.

---

[5] A more sophisticated screening process that "tracks" the movement of the target relative to corresponding movements in the antenna platform will easily separate the "ghosts" from the actual target.

[6] At the field point directly above the target, the true solution and its "ghost" are indistinguishable. To within numerical round-off errors, they in fact represent a 2nd order root of equation 12.

components from a constant noise source (1000 μV μs integrated gate noise for a 500 μs gate width). Figure 15, corresponding to a CMRR = 50, is typical of these results. The results of these calculations show that the target position is correctly estimated to lie within the 10cm sphere at only 10 of the interior points. This is to be expected since the SNR is well below the minimum necessary for reliable physics-based modeling at horizontal distances greater than 1m from the target center (see Figure 13).

The results from Figure 14 and Figure 15 together with similar calculations made for other values of gradient CMRR are summarized in Figure 16. Here, we have plotted the number of correct position estimates as a function of the error radius (i.e., the size of the green sphere). There are no real surprises here. The results show that for reasonable noise values, we can expect good solutions for position only for field points lying within a short horizontal radius (<1m) of the target position. Naturally, these are the points where the SNR is the highest. Naturally, the quality of position estimates (and hence other target properties) will obviously improve by considering estimation and parameterization using as many of the interior points as possible. However, this analysis demonstrates that tracking or mapping a single target in real time from measurements at a single field point is practical.

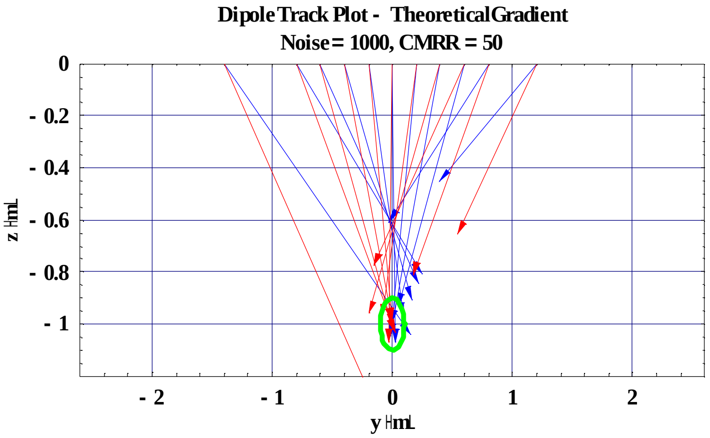

Figure 15: Dipole tracking plot showing feasible target position solutions along a 27-pt profile. The Gaussian distributed noise with a standard deviation of 1000 μV·μs has been added to the secondary magnetic field. The same noise but attenuated by the CMRR (50) is added to the gradient components.

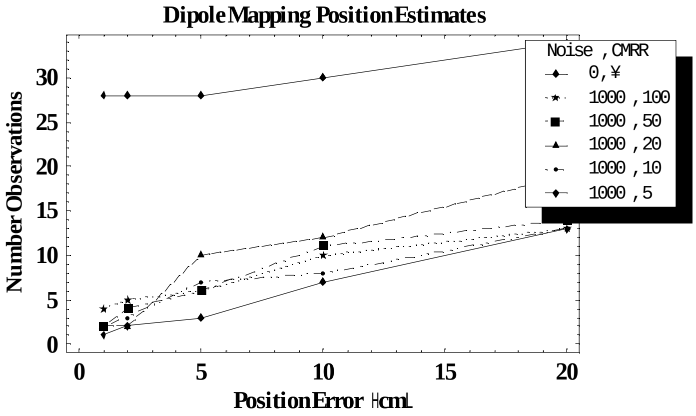

Figure 16: Dipole tracking solution efficacy as a function of allowable position error shown parametrically as a function of gradient errors. The noise-free case (top trace) is shown for reference.

4.1.2.3 *Gradient Errors*

The preceding study suggests that, provided our gradiometer has a sufficiently small baseline so that the resulting field differences are "good" estimates of the gradient field, we can derive useful interpretive information by treating the differences as gradients and thereby benefit to a certain degree by the resulting simplification of the problem. We learned, however, in section 4.1.1.1 that for the standard test object at a depth of 1m we can expect errors in the gradient estimates on the order of 10% when using a gradiometer baseline distance of 0.5m. We can, of course, decrease the baseline moderately and expect a commensurate improvement in the quality of the gradient estimates. However, we must keep in mind that a smaller gradient baseline while insuring better approximations of the gradient field from proximate targets also increases the level of gradient noise since the real gradient noise is proportional to the ratio of voltage difference noise to gradient baseline.

We can study the effect of the gradient errors on interpretation, in the same way that we studied the effect of noise. We calculated 5 profile data sets using the gradient baseline distance as a parameter. No noise has been added to the field data and therefore, to the extent that the quality of the dipole mapping solutions varies from that shown in Figure 14 and Figure 16 (Noise = 0, CMRR = ∞), the difference in the quality of the position estimates must be attributed to the gradient errors as they become significant in the region near the target. Figure 17 and Figure 18 show the results of applying the dipole tracking algorithm to finite gradient data calculated for baselines of 0.25m and 0.5m, respectively. With a baseline of 0.25m, ¼ the depth of the target, the results in Figure 17 are very similar to those for theoretical gradients with no noise (Figure 14). That is, the estimates of target position fall within an acceptable radius of the true target position at nearly all of the 27 field points examined.

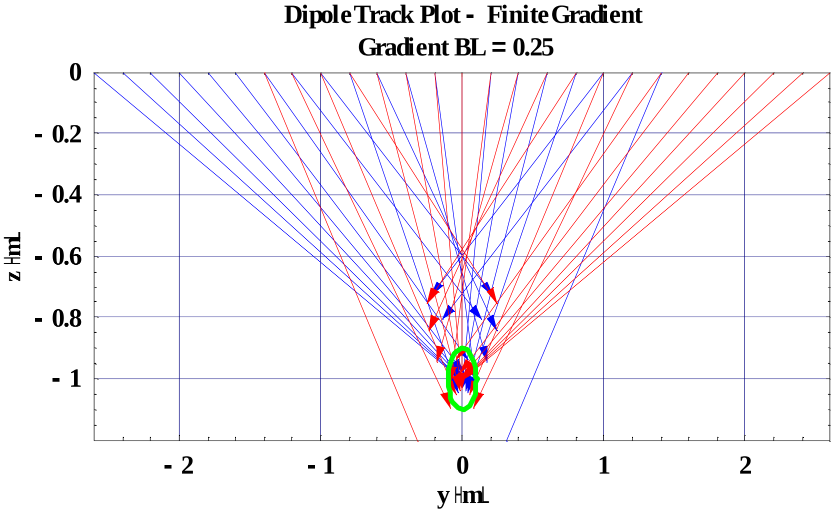

Figure 17: Application of dipole tracking algorithm to target location using synthetic finite gradient data. The data represent calculations over a baseline of 0.25m, representing ¼ of the depth to the target.

The results in Figure 18 summarize the analysis of data for a finite gradiometer with a baseline of 0.5m. It is interesting to note that target position estimates are better for field points where |y| > 1. The estimates from field points in the range –1< y < 1, where the ratio of the distance to the target (*R*) to the length of the gradient baseline (*l*) lies in the range 2 ≤ *R/h* ≤ 2.8, predict that the target lies rather uniformly too deep. Likewise, the horizontal range to the target is systematically underestimated.

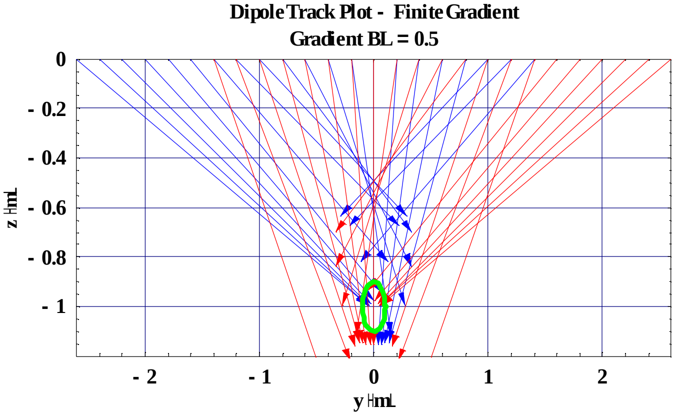

Figure 18: Application of dipole tracking algorithm to target location using synthetic finite gradient data with a 0.5m baseline or ½ of the depth to the target.

We summarize the results derived from Figure 17 and Figure 18 together with similar results for 3 additional baseline lengths (0.30m, 0.35m, 0.40m) in Figure 19. For reference, we have reproduced the results for the theoretical gradient (no noise) and labeled it with the parameter “TG”.

4.1.2.4 *Remarks*

The finite baseline experiment clearly demonstrates that approximations to the gradient tensor from a finite baseline gradiometer will be most useful for interpretation at ranges that are greater than 3 times the baseline length (*R/h > 3*). When this rule is violated, the quality of the position estimates (and also estimates of moments) degrades significantly. Nevertheless, the results show that the algorithms we employed (i.e., *dipole tracking*) continue to produce useful estimates of target information even when *R/h* < 3. Because of its numerical efficiency, it is feasible to employ the *dipole tracking* algorithm in real time as a means for target location and to provide preliminary parameterization. The results we

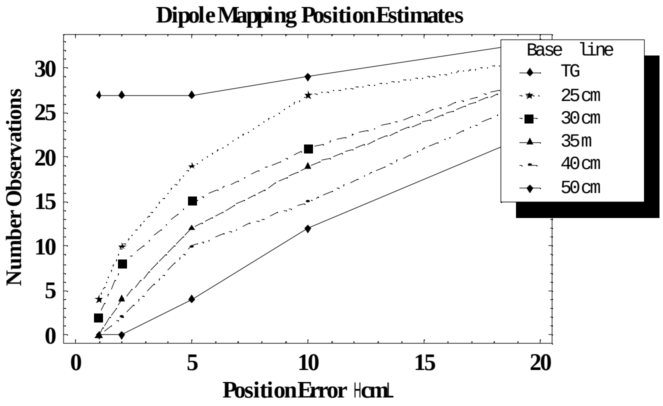

Figure 19: Dipole tracking solution efficacy as a function of allowable position error for a finite baseline gradiometer. The parameter is the length of the baseline.

have presented here confirm the contention we made in our proposal for this project that dipole tracking can play an important role as a means of target parameter extraction, particularly as the process of UXO target detection and characterization evolves in an attempt to reduce the need for costly target reacquisition following post acquisition analysis of compiled map data.

As we have shown earlier, gradient noise caused by leaking of common-mode EMI noise into the difference data from sensor imbalance and alignment errors, reduces the SNR at long range to the point where neither the field data nor the gradient data are useful for interpretation. Based on the experiments with theoretical gradients plus noise as well as our own practical experience with the AOL system and other EM systems, the area over which the SNR of the EM anomalies for most buried UXO is sufficiently high for useful quantitative interpretation typically lies within a circle of radius 1m centered on the target location. Within this same area, gradient errors from the difference approximation degrade the solution for target position when the target range to baseline distance ratio (*R/h*) is less than 3. Therefore, precise estimates of target parameters will require the application of traditional inversion methods involving the analysis of static data from multiple data points using a forward modeling algorithm that considers the finite dimensions of the antenna array.

4.1.3 The Realization of a Practical Finite Gradiometer

The preceding sections provide general guidelines that we must apply to the realization of a finite gradiometer:

1. **Baseline**: Direct interpretation of gradient data provides accurate estimates of the parameters from isolated targets provided the range-to-baseline ratio (*R/h*) is greater than 3. Interpretations for *R/h* < 3 degrade significantly. However, for 2 < *R/h* < 3 we have established that gradient estimates using finite differences can yield rapid semi-quantitative estimates of target parameters. In this range the estimates of the gradient depart from theoretical values by as much as 10%.
2. **Noise:** As with conventional systems**,** random EMI noise arising from distant sources shortens the effective range of the gradiometer. Using a realistic value for random EMI receiver voltage noise (O[2μV] = 20 nT/s), and assuming a common mode rejection ratio (CMRR) of 50, the results in Figure 15 show that the useful lateral range of the gradiometer is approximately 1m from the target center. The SNR of the 60mm target at these noise levels is approximately 30dB. We conclude, therefore, that the CMRR of the gradient coil pairs must be in the range of 50-100.[7]
3. **Systematic Errors:** The errors that arise in using a finite difference approximation for the actual gradient are systematic errors. As we alluded in number 1. above, these errors can be as high as 10% (when *R/h* = 2) and still provide a useful semi-quantitative interpretation. Other systematic errors are produced by imperfect geometry and coil sensitivity (balance). A useful design specification therefore is to keep systematic errors for these sources to < 1% of the theoretical anomaly (i.e. << maximum error from the finite baseline).

---

[7] A CMRR in the range of 50-100 is consistent with that achieved in the LBL BUD system (Alex Becker, personal communication).

In the remainder of this section, we will try to translate the last guideline (i.e., systematic errors < 1% of theoretical anomaly). To do this, we have modeled a realization of a finite gradiometer system such as illustrated in Figure 6 that includes the 3 main sources of mechanical and electronic error (Bracken & Brown, 2006). In section 4.1.1.2, we enumerated these sources. Here, we attach a realistic value to the specification and calculate the noise levels that arise from this hypothetical gradiometer. The specifications are:

1. Orthogonality Error: < ±0.5º
2. Positioning Error: < ±1mm
3. Sensitivity Error: < ±1%

These three specifications can be met, we believe, with available materials and electronic components provided that reasonable care is exercised in machining and fabrication so that the specifications are not compromised. If we accept that these specifications can be met, we now seek to determine whether the systematic gradient errors and the noise errors that will arise in a gradient system that meets these specifications are significantly less than the gradient errors arising from using a finite baseline. In that context, we have noted that even gradient errors as high as 10%, as occur with a 0.5m baseline gradiometer in the presence of a target at depth 1m, we are still able to do rough quantitative work using gradients. Therefore, we assert here that a reasonable threshold for these other errors would be 1% of the peak anomaly for our standard target. That would require that the errors from these 3 major sources of gradiometer error to be 1/10th those arising from the finite baseline itself.

We used the specifications given above as the standard deviations for randomizing the 3 types of errors that are common to gradiometers. Then, we calculated the gradiometer output for two types of inputs:

1. Standard Target (i.e., 60mm target at 1m depth)
2. Uniform Gaussian field noise of 1000 μV-μs (equivalently 2 μV, or 20nT/s).

The results of the first experiment are summarized in Figure 20. Here, we have plotted the gradient and field errors as a percentage of the corresponding theoretical values for the standard target (Figure A-1). As in previous figures we have companded the profiles in order to emphasize low-level errors. Here, we use a companding threshold value of 0.01%. The green horizontal lines represent the 40dB amplitude level for each polarity of the error. We can see from the plot that systematic gradient errors are less than or equal to 1% of the maximum I1 gradient. Thus, systematic errors are indeed much smaller than the errors from a finite baseline.

The results of our second experiment are shown in Figure 21. In the Figure, we report the random noise arising in the gradiometer from sensitivity imbalance and orthogonality errors along the standard profile without the presence of a target. In effect, we are assuming that the random noise process is ergodic so that as we move from one station to the next, we get a new noise sample. The statistics of the profile thus represent the statistics of the noise process. As before, we have normalized the results by the theoretical gradients and fields for the target involved (Figure A-1) and reported the results on a companded scale. This result shows that the level of random noise that leaks into the gradient components is about 0.1%.

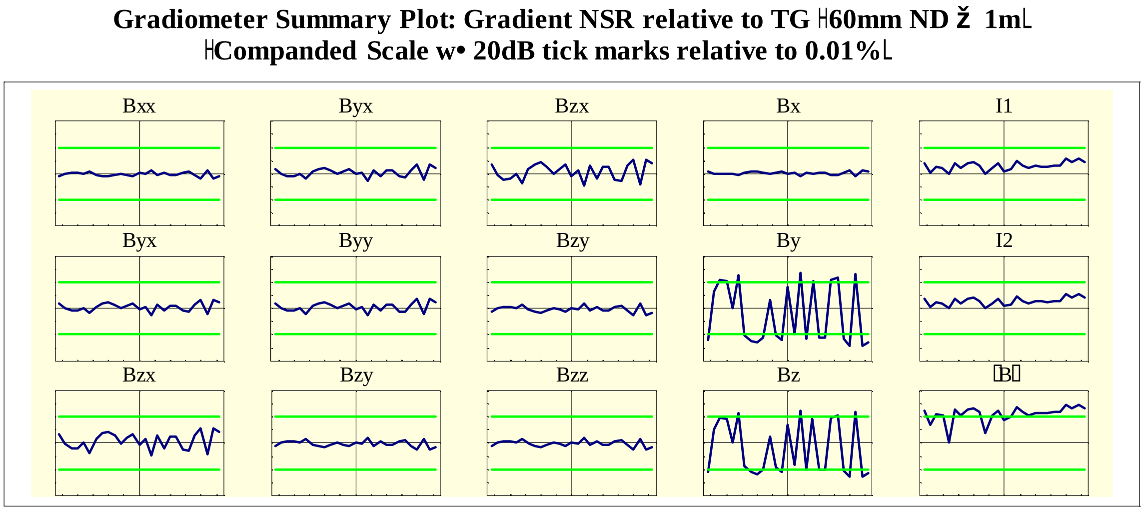

Figure 21: Random gradient noise from a finite gradiometer with ±0.5º Orthogonality, ±1mm Positioning, and ±1% sensitivity balance. Errors in dB relative to the theoretical peak values of I1 (gradient) and |B| (field) are scaled in dB relative to 0.01% for each polarity. The green lines represent the 1% error threshold. The standard deviation of the noise for this experiment was 1000 µV· µs.

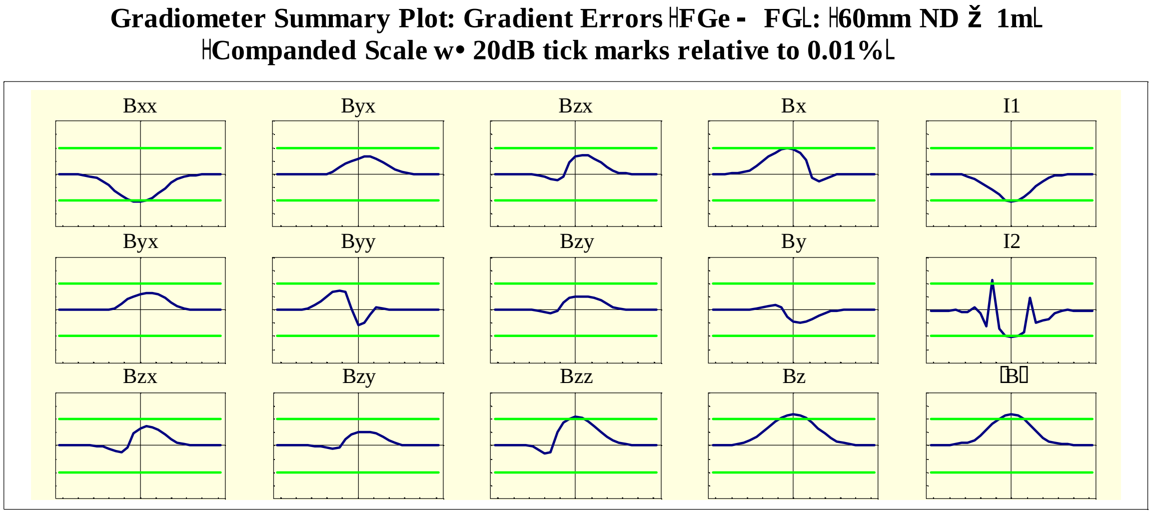

Figure 20: Systematic errors arising from a realistic implementation of a 5-sensor finite gradiometer having a specification of ±0.5º Orthogonality, ±1mm Positioning, and ±1% sensitivity balance. Errors are reported as a percentage of the anomaly peaks, respectively of I1 and |B| for the theoretical curves for a point gradiometer. The figure is based on a ½-m

4.2 Target Resolution with EM Gradient Measurements

Improved resolution of magnetic sources is often listed as one of the main advantages of measuring passive magnetic gradients for shallow subsurface mapping (Schmnidt & Clark, 2006) (Slack, Lynch, & Langan, 1967). Because the theory for calculating the EMI response of UXO is closely related to calculating the passive magnetic anomalies of small objects (Das, McFee, Toews, & Gregory, 1990), we quite naturally listed “improved” target resolution as a likely advantage of measuring the gradient of the induced secondary EM field arising from buried conductors such as UXO.

In this section, we present the results of numerical experiments that we conducted in an effort to demonstrate that our proposed gradiometer will indeed provide improved resolution and thus help to identify and/or clarify situations where it is difficult to determine whether an anomaly arises from a single source or is the result of 2 or more interfering sources.

4.2.1 The Standard Target Object

We used the polarizability response of a prolate spheroid with a diameter of 60mm and a length of 180mm (3:1 aspect ratio) as our target object. The conductivity of the spheroid was set at 10^7 S/m and its relative magnetic permeability was set to 180 (typical for common carbon steel). The principal polarizability transients for the target are shown in Figure 22. Since we are interested only in the shape of the resulting spatial anomalies, our models use polarizability values representing the average values over a 500 µs time gate from $400 \leq t \leq 900$ µs. This gate is similar to that of an EM61 MkII (3rd standard time gate centered at 660 µs).

4.2.2 Target Resolution: Single Targets

When dealing with single targets, resolution is usually measured by the size of the anomaly footprint when dealing with maps. When dealing with a profile, the anomaly size is usually measured either by the anomaly width at half its maximum (FWHM) or, alternatively, the anomaly width at the two points of inflexion[8] on the sides of the main anomaly lobe (Pedersen & Rasmussen, 1990). Here, we will use the point of inflexion rule to compute anomaly width.

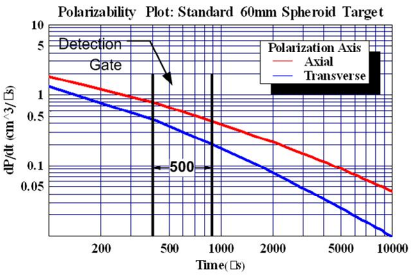

Figure 22: Principal polarizability transients for a standard 60mm spheroidal target. The EMI response of the target is similar to that of a 60mm mortar.

4.2.3 On Tensor Invariants

The invariants of a vector (a tensor of rank 1 – e.g., $\mathbf{B}^s$) or a tensor of rank 2 (e.g., $\nabla\mathbf{B}^s$) are of interest because they are scalars that are independent of the coordinate system in which their corresponding tensor is expressed. Here, we adopt the notation used in Pederson (Pedersen & Rasmussen, 1990) identify three invariants that we calculate from the magnetic field and its gradient:

---

[8] A function *f(x)* has a point of inflexion where the second derivative the function $\frac{df^2(x)}{dx^2} = 0$

$$\begin{aligned}
&\mathbf{B} = B_x\hat{\mathbf{i}} + B_y\hat{\mathbf{j}} + B_z\hat{\mathbf{k}}; \qquad |\mathbf{B}| = \sqrt{B_x^2 + B_y^2 + B_z^2} \\
&\nabla\mathbf{B} = \begin{bmatrix} \dfrac{\partial B_x}{\partial x} & \dfrac{\partial B_x}{\partial y} & \dfrac{\partial B_x}{\partial z} \\ \dfrac{\partial B_y}{\partial x} & \dfrac{\partial B_y}{\partial y} & \dfrac{\partial B_y}{\partial z} \\ \dfrac{\partial B_z}{\partial x} & \dfrac{\partial B_z}{\partial y} & \dfrac{\partial B_z}{\partial z} \end{bmatrix} = \begin{bmatrix} B_{xx} & B_{xy} & B_{xz} \\ B_{yx} & B_{yy} & B_{yz} \\ B_{zx} & B_{zy} & B_{zz} \end{bmatrix}; \; \nabla\mathbf{B}' = \nabla\mathbf{B} \\
&I_0 = \mathrm{trace}(\nabla\mathbf{B}) = 0 \\
&I_1 = B_{xx}B_{yy} + B_{yy}B_{zz} + B_{xx}B_{zz} - B_{xy}^2 - B_{yz}^2 - B_{xz}^2 \\
&I_2 = \det(\nabla\mathbf{B}) = |\nabla\mathbf{B}| = B_{xx}\left(B_{yy}B_{zz} - B_{yz}^2\right) + B_{xy}\left(B_{yz}B_{xz} - B_{xy}B_{zz}\right) \\
&\qquad\qquad + B_{xz}\left(B_{xy}B_{yz} - B_{xz}B_{yy}\right)
\end{aligned} \tag{5}$$

Note that the gradient tensor is symmetric and its trace is zero.

In the plots that follow, we have taken the square root of I_1 and the cube root of I_2 in order that the invariants have the same units as their associated tensor elements. Moreover, in the maps we have *companded* the data to provide logarithmic-like compression of the dynamic range. The companding algorithm can handle bipolar data and is scaled so that the output approximates the data amplitude scaled in dB relative to an arbitrary threshold. The data companding is useful for plotting. However, it distorts the profile and the color pattern in a way that tends to obscure a subjective determination of target resolution relative to other possible mapping components. Therefore, to determine resolution we must use (and plot) the relevant data on a linear scale.

Pedersen (Pedersen & Rasmussen, 1990) notes that the invariant I_2 provides better anomaly resolution than I_1 and, for dipole fields induced by a uniform field, the resolution improvement when using I_2 relative to using B_z is approximately 50%. Thus, in graphics where we do not display every gradient and field component, we have chosen to display B_{zz}, B_z, and I_2. These components all exhibit a peak response for field points located directly over the target.

4.2.3.1 *Excitation: Finite (horizontal) loop versus uniform field*

The theory for computing the EMI response of buried conductive and permeable targets is based magnetostatic principles wherein the effect of the (usually) low conductivity of the host is ignored and the totality of the eddy currents that have been induced in the highly conductive target can be approximated by a point dipole. Although there are exceptions, the approximations are valid for conductive and permeable targets that are small relative to the distance from the transmitter and receiver antennae, and the conductivity of the host is less than 1 S/m (Baum, 1999) (Pasion, 2007).

For the purposes of this discussion, we can ignore the fact that the secondary magnetic fields we measure arise from decaying eddy currents rather than the polarization of magnetic particles. Thus, the main difference between the spatial behavior of target anomalies measured with a magnetometer and those we measured with an EM system is in the nature of the primary field. With passive magnetic measurements as well is with EM detection methods such as sub-audio magnetic (SAM) the stimulating magnetic field is uniform in space and therefore the target properties (i.e., the magnetic moment) has a constant direction and magnitude. In general, on "metal detection" EM instruments such as the EM61 the stimulating magnetic field at the target varies both in direction and magnitude as the instrument passes over the target (Figure 23).

To study differences in resolution as it pertains to passive magnetic surveys (and often by inference to EM surveys), we have modeled the response of our standard 60mm target to a primary field generated by a 1m x 1m horizontal transmitter loop (EM61) and to a uniform (vertical) field.[9]

Figure 24 below shows maps of each of the 9 components of the secondary gradient tensor ($\nabla\mathbf{B}^s$), the 3 components of the secondary fields ($\mathbf{B}^S$), and three tensor invariants. The two panels (A & B) relate to the attitude of the target. The horizontal target (top panel) is oriented so that the target axis is parallel with the y (vertical) axis of the maps. Note the obvious elongation of the anomaly foot print in the direction of horizontal heading of the target. When we deal with a vertically oriented target, Figure 24B, the anomaly footprint is no longer elongated in the y-direction. And finally, note that in both cases (horizontal and vertical attitudes) the footprint of the gradient maps is perceptibly smaller than those of the field maps (compare Bzz with Bz). Thus, these maps certainly provide qualitative evidence of improved resolution.

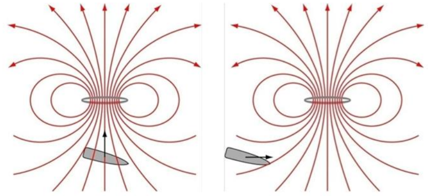

Figure 23: Figure illustrating the change in amplitude and direction of the stimulating field at the target as the antenna array passes over it.

Figure 25 show results of target stimulation with a uniform vertical field. The target is the same (60mm target at 60cm depth, horizontal/vertical attitudes). In this case, the anomaly footprint over the horizontal target is no longer elongated because the target is always polarized with a vertical field. Comparing Figure 24 and Figure 25, it appears that the spatial resolution with uniform field polarization is better than that what we see for stimulation with the 1m x 1m loop transmitter.

Finally, in Figure 26 we have plotted center-line profiles in the y-direction over the same 60mm targets. To simplify the figure, we show only the vertical gradient (Bzz), the vertical field (Bz), and the I_2 invariant of the tensor gradient field. In each of the panels, there are two profiles corresponding to stimulation with the finite loop and the uniform field, respectively. Note that the Bz profile with finite loop stimulation (Figure 26B) displays the double hump anomaly pattern that is characteristic of EM anomalies over elongate targets with a horizontal attitude. The profiles also show the extended width of the anomaly in the direction of the target heading

---

[9] A uniform field is approximated by using a very large (1000m on a side) horizontal transmitter loop. The amplitudes of the transmitter fields have been normalized so that the fields at the target when the 1m x 1m loop is centered over the target are the same.

for the horizontal target attitude when the stimulated by the finite loop source. However, there is no significant difference in anomaly width for the different types of stimulation for a target with a vertical attitude Figure 26D, Figure 26E, and Figure 26F. Finally, there is a clear difference in resolution when we compare the vertical gradient curves (Bzz –Figure 26A and Figure 26D; I2 – Figure 26C and Figure 26F) with the vertical field profiles Figure 26B and Figure 26E). We have quantified that difference for the finite loop transmitter case in Figure 27. These figures show a quaisi-linear relationship between target depth and anomaly width for both the horizontal and vertical targets. Roughly speaking, the ratio of anomaly width between Bzz and Bz is approximately 0.75 for a target at a depth of 0.6m. Thus, Bzz has about 25% better resolution than Bz for targets at that depth. Regardless of target orientation, the resolution ratios (width Bzz/width Bz, width I2/width Bz) remain relatively uniform over the depth interval we studied with mean values of (approximately) 0.8 and 0.65, respectively, for Bzz and I2. In general terms therefore we can say that the resolution of targets is improved by about 20% when we use Bzz as a mapping parameter and 35% when we use I_2 as a mapping parameter.

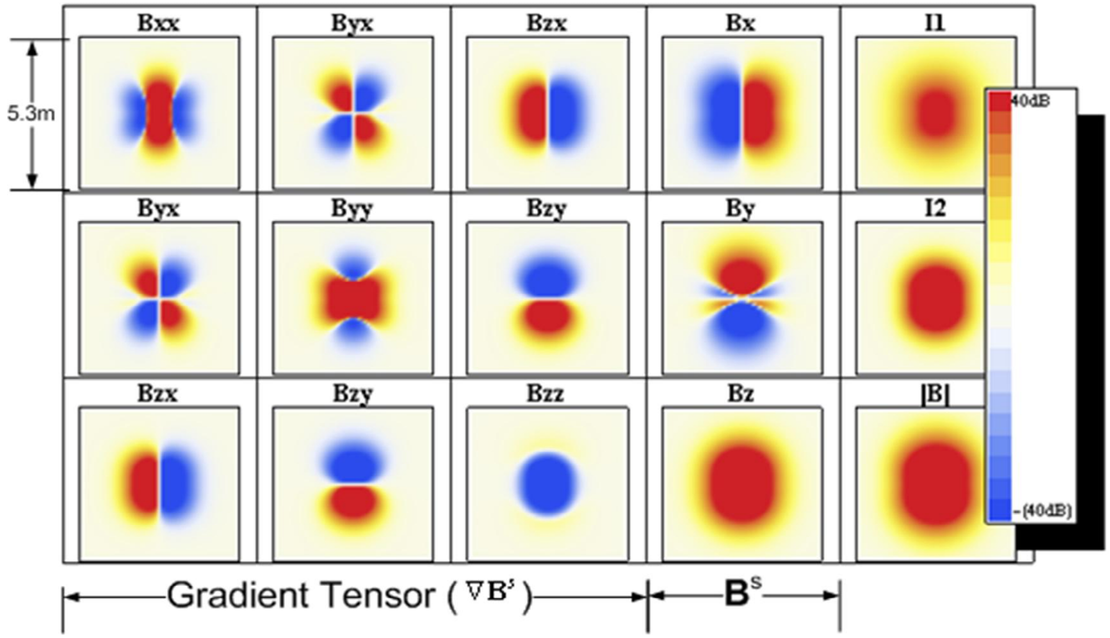

A) Finite loop excitation (1m x 1m), horizontal target

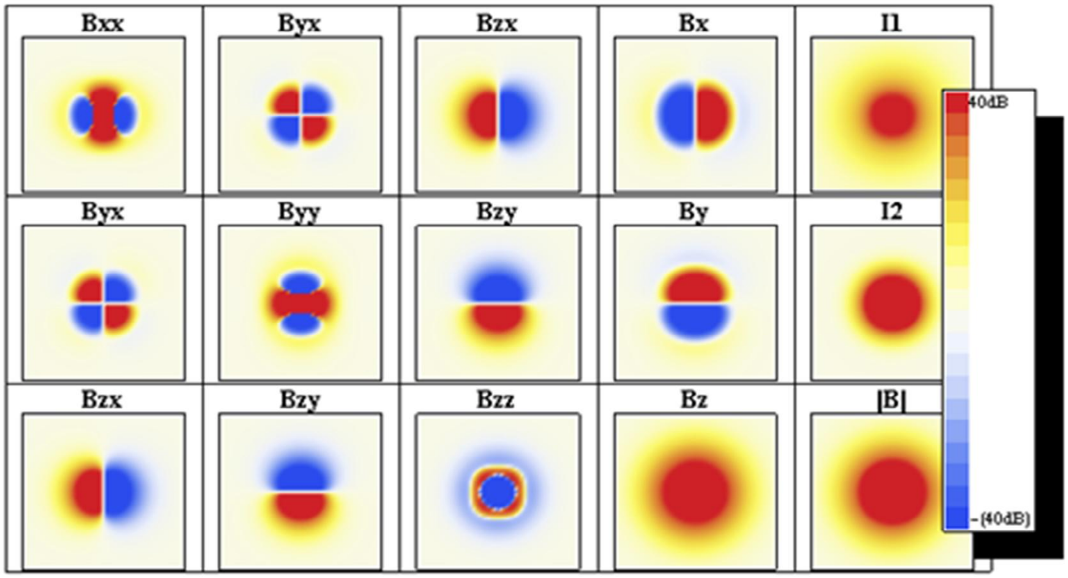

B) Finite loop excitation (1m x 1m), vertical target

Figure 24: Summary plot showing false color images of the gradient tensor elements (cols 1-3), the fields (col 4), and the field invariants (col 5) calculated for a 60mm target located at a depth of 60cm beneath the plane of the transmitter. The two figures correspond to target attitudes of horizontal (A) and vertical (B).

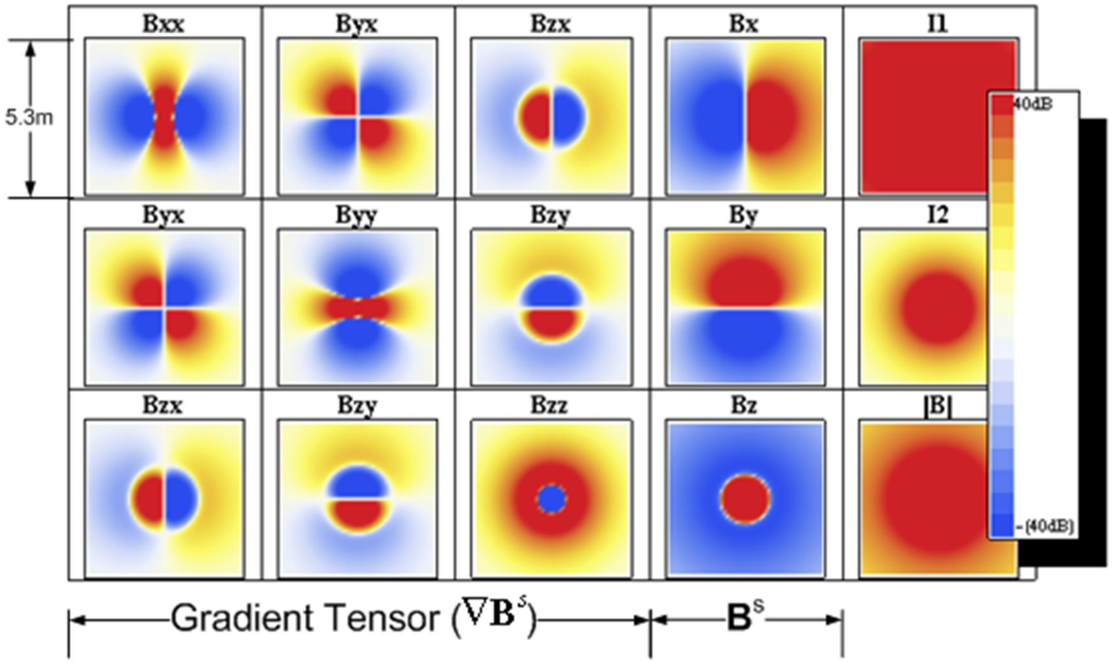

A) Uniform field excitation, horizontal target

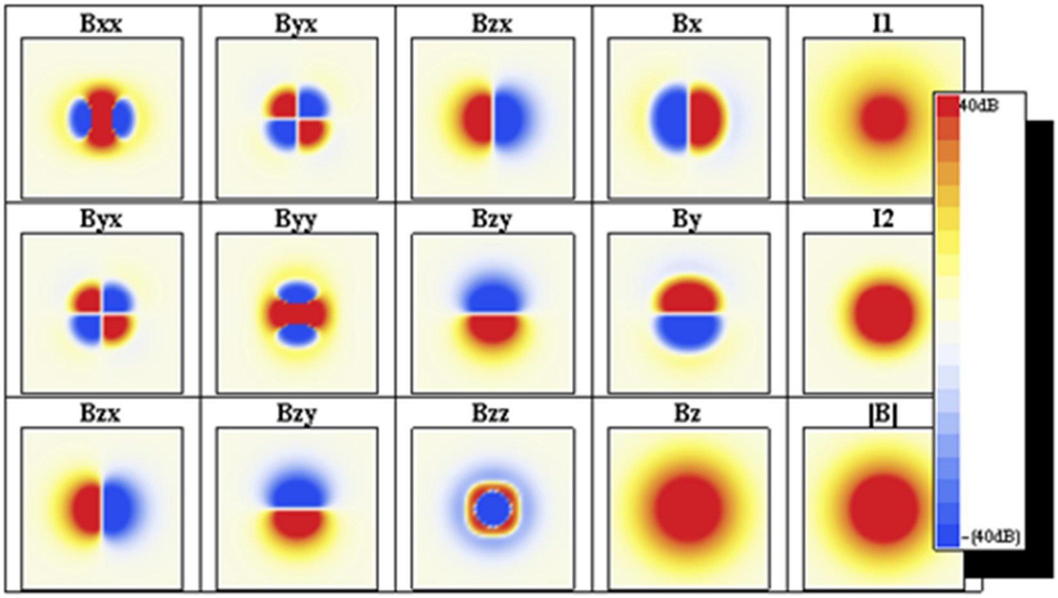

B) Uniform field excitation, vertical target

Figure 25: Summary plot showing false color images of the gradient tensor elements (cols 1-3), the fields (col 4), and the field invariants (col 5) calculated for a 60mm target located at a depth of 60cm beneath the sensor. The primary field is a uniform vertical field. The two figures correspond to target attitudes of horizontal (A) and vertical (B).

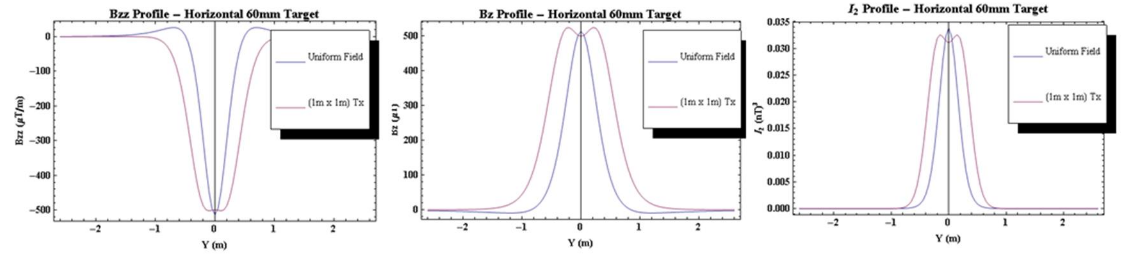

A) Bzz – horizontal target (z = 60cm) B) Bz – horizontal target (z = 60cm) C) I2 – horizontal target (z = 60cm)

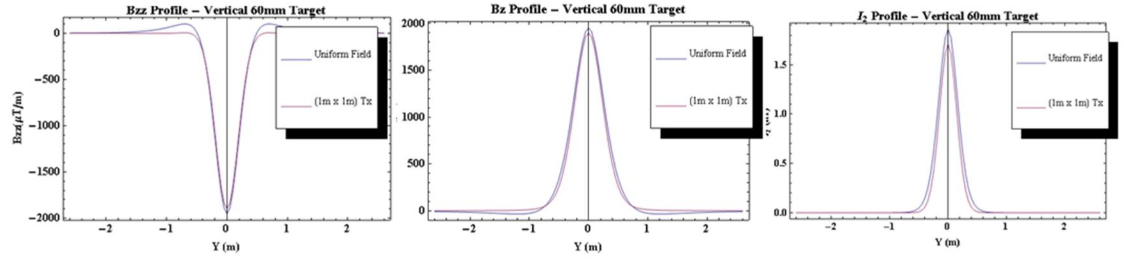

D) Bzz – vertical target (z = 60cm) E) Bz – vertical target (z = 60cm) F) I2 – vertical target (z = 60cm)

Figure 26: Profiles of the vertical gradient (Bzz- A,C) and the vertical field (Bz-B,D) over a 60mm target buried 60mm deep. The parametric curves relate to the nature of the primary field (uniform or 1m x 1m loop).

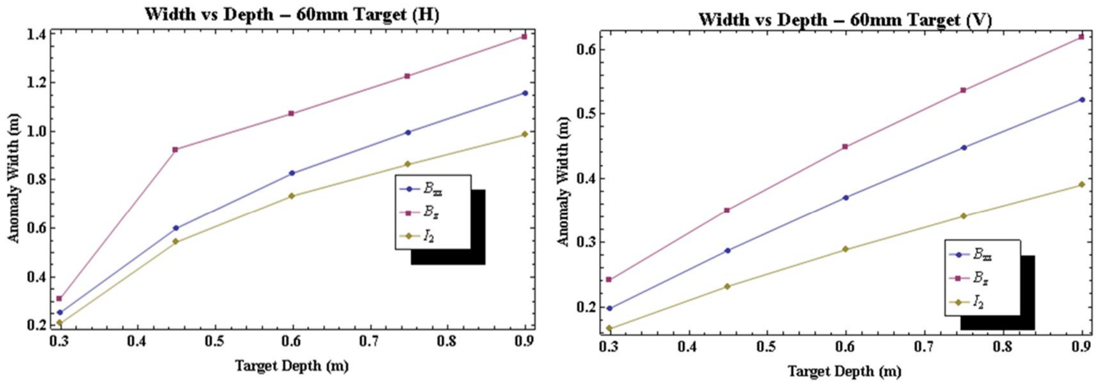

A) Finite loop stimulation, horizontal target B) Finite loop stimulation, vertical target

Figure 27: Figures plotting anomaly width versus target depth for a horizontal target (A) and a vertical target (B). The results are for finite loop transmitter stimulation. The curve parameters are Bzz (vertical gradient), Bz (vertical field), and I_2 (an invariant of the gradient tensor), respectively. The widths are defined as the distance between the points of inflexion on the main anomaly lobe.

4.2.4 Target Resolution: Multiple Targets

Identifying anomalies that result from two or more closely spaced targets is often important in UXO characterization. We know, for example, that it is difficult or impossible to determine that an anomaly is the result of two interfering targets when their lateral separation is less than their depth. In this section, we study the behavior of fields and their gradients for a pair of 60mm targets with identical attitudes (horizontal and vertical) and located at the same depth. Summary plots and profiles for various cases are shown below in Figure 28 through Figure 30.

Figure 28 shows the summary plots for horizontal targets oriented in the y-direction. The targets are 0.6m below the antenna array. Each successive summary plot represents a different horizontal separation between the targets ranging from 0.3m (1/2 the target depth) to 2.4m (4x target depth). There is no visual cue that the anomalies result from 2 targets when they are separated by 0.3m (Figure 28A). At a separation of 0.6m (Figure 28B) there is a subtle clue that there are two targets in the pattern of By, which is strangely elongated. However, the other components have a normal behavior so it would be difficult to identify the anomalies as resulting from two targets without examining the profiles (e.g., Figure 30). Finally at a separation distance of 1.2m (Figure 28C), it becomes obvious that there are two targets involved. The corresponding plots for two vertically oriented 60mm targets are shown in Figure 29. And because we do not have to deal with elongated anomalies that are characteristic of horizontal targets, there are indications of multiple target sources in By, Bz, Bzy, and Bzz.

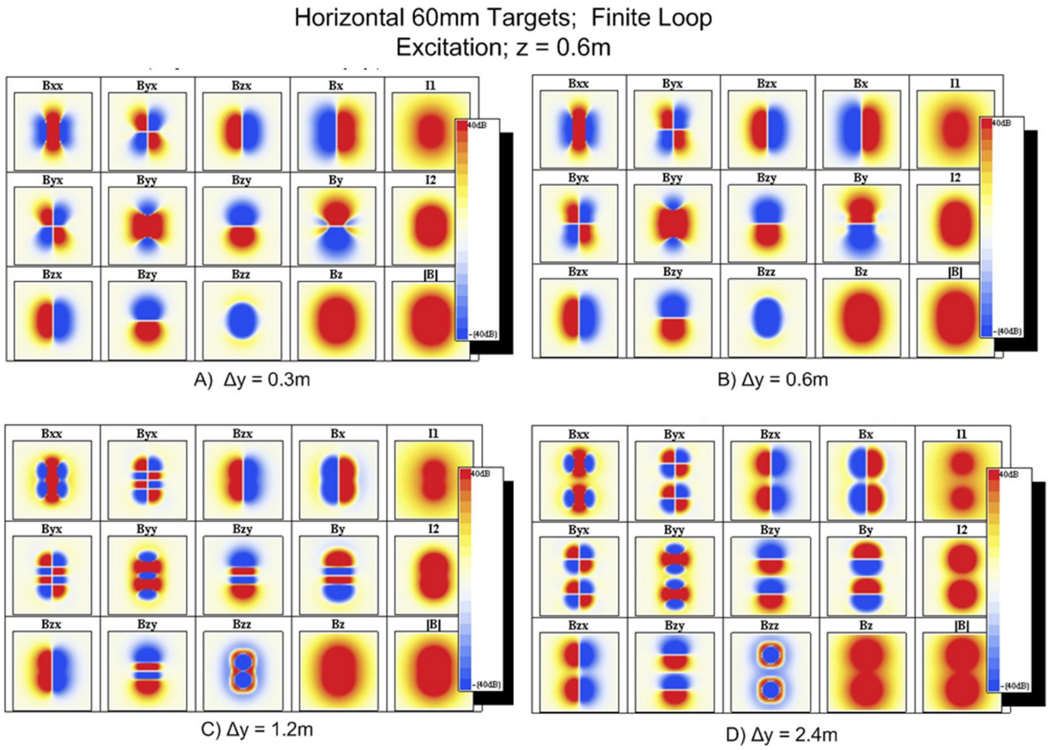

A) Δy = 0.3m

B) Δy = 0.6m

C) Δy = 1.2m

D) Δy = 2.4m

Figure 28: Summary plots of the tensor gradient components ($B_{??}$), the secondary magnetic induction field components ($B_?$), and their associated invariants (I1,I2,|B|). These maps represent the response of 2 horizontal 60mm standard targets with a heading parallel to the y (vertical) axis at a depth of 0.6m below a 1m x 1m finite loop transmitter. The separation of the targets ranges from 0.3m (A) to 2.4m (D).

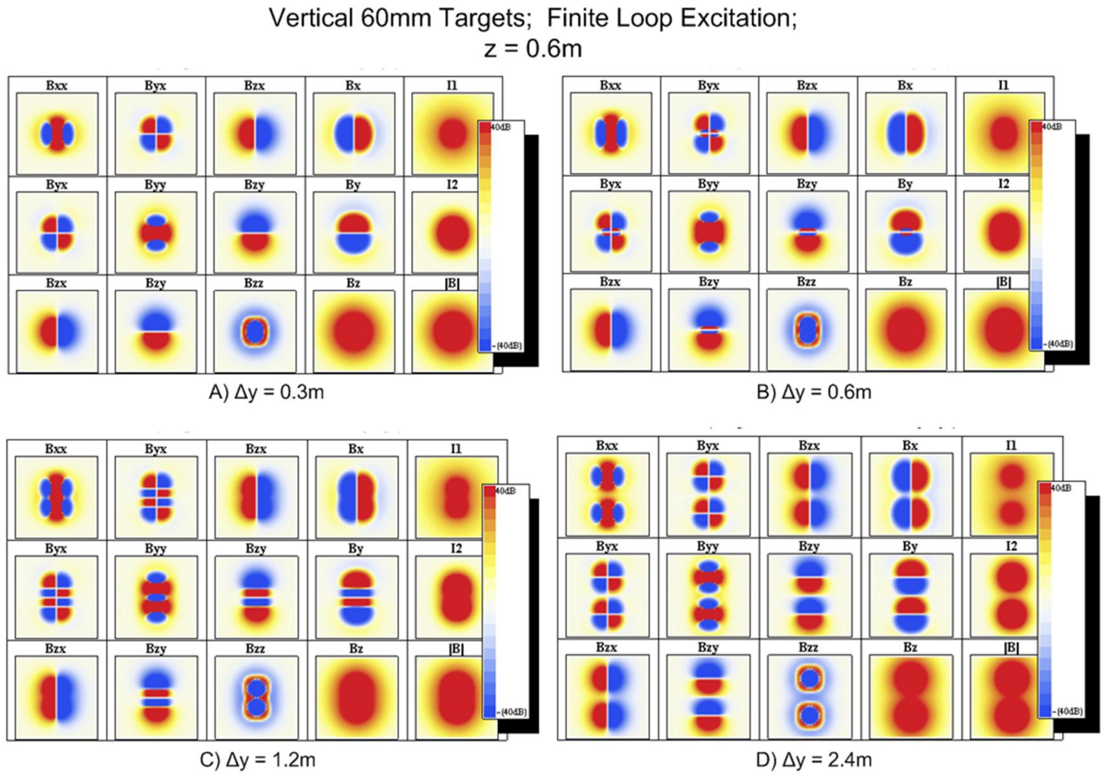

Figure 29: Summary plots of the tensor gradient components ($B_{??}$), the secondary magnetic induction field components ($B_{?}$), and their associated invariants (I1,I2,|B|). These maps represent the response of 2 vertical 60mm standard targets at a depth of 0.6m below a 1m x 1m finite loop transmitter. The separation of the targets ranges from 0.3m (A) to 2.4m (D).

The detailed characteristics of these complex anomalies are best seen in the profiles shown in Figure 30. In the Figure, we have plotted the vertical gradient (Bzz) in the left hand column and the vertical field (Bz) in the right hand column for horizontal targets (top row) and vertical targets (bottom row). For this figure, the targets are separated (in the y-direction) by 0.6m. The following anomaly characteristics are noted:

- **Width –** The anomaly widths suggest a target located at a depth as much as twice as deep as the actual depth.
- **Side-Lobe Distortion(horizontal targets)** – At this “threshold” target separation, the side-lobe distortion “shouldering” on horizontal targets is very subtle and might be missed when the data are noisy.
- **Double Peak Anomaly in Bz –** When looking at the profiles for two vertical targets, they interfere in a way that results in a classical double peak anomaly that might easily be mistaken for a single horizontal target at a much greater depth.
- **Double Peak Anomaly in Bzz and I_2 (vertical targets)–** The Bzz profiles for the vertical targets also form subtle double peaks for the deeper targets. However, unlike the double peaks in Bz, the Bzz and I_2 double peaks are much too widely spaced to be confused with their respective anomalies from a single horizontal target (see Figure 30A).

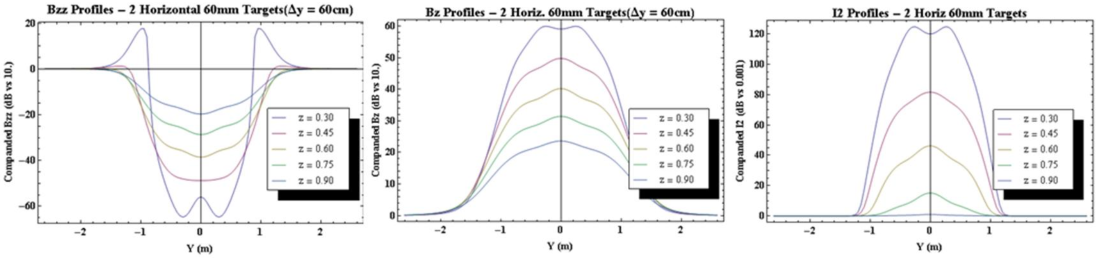

A) Bzz – Horizontal targets B) Bz – Horizontal targets C) I2 – Horizontal targets

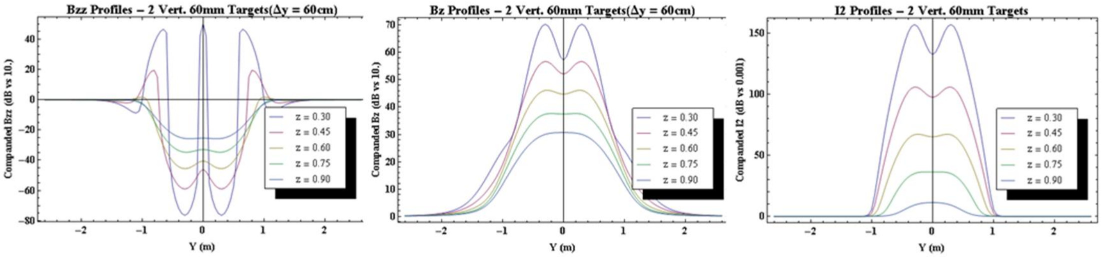

D) Bzz – Vertical targets E) Bz – Vertical targets F) I2 – Vertical Targets

Figure 30: Center-line profiles (in y-direction) over a pair of 60mm targets at 0.6m depth separated by a distance of 0.6m. The profiles in the top row are those for horizontal targets oriented in the y-direction. The bottom row represents profiles when the targets are vertical.

4.2.5 Conclusions – Target Resolution with EMI Metal Detection

Measuring and mapping gradient rather than field components of the secondary magnetic fields arising from induced eddy currents provides marginal improvements in resolution over both single and multiple targets (25% to 35%). The best resolution improvement is realized by using the gradient tensor invariant I_2. Similar to the widths of passive magnetic anomalies, crude depth estimates can be made by scaling the widths from EMI target anomalies. This possibility was originally noted by Das (Das, McFee, Toews, & Gregory, 1990) and this work simply corroborates that original work. It is clear from this work that for non-vertical targets, the anomaly width will be highly dependent on the profile heading relative to the target heading, with the smaller width being observed along profiles normal to the target heading while the larger width will be observed along profiles with the same heading as the target. One must be circumspect when applying a width to depth conversion.

We have noted that the resolution of target anomalies from an EMI metal detector is not as good as that observed over targets that are illuminated by a constant uniform field. In our modeling with a uniform field we normalized the inducing fields at the target so that anomaly amplitude at a point directly over the target was the same for both systems. The difference in resolution must be attributable, therefore, to the fact that the target polarization direction and amplitude changes at each field point. This result has important ramifications since it suggests that passive magnetic surveys (fields and gradients) are better suited to detecting multiple interfering targets than is an EMI survey instrument (with finite loop transmitter) even when the EMI detectors include gradiometer or difference measurements.[10] Along the same lines, we can also state that

---

[10] We assume here that the targets are ferromagnetic so they have associated passive magnetic anomalies.

an EMI system consisting of a large fixed loop transmitter (similar to the SAM system) would perform better both in detection and in target resolution.

All those who interpret EMI metal detector data are aware that elongate targets oriented with a horizontal attitude will generate double-peaked anomalies. This model study has shown that two 60mm targets oriented vertically and spaced at a distance equal to the depth of burial (see Figure 29B and Figure 30D - Figure 30F) can likewise generate double-peaked response curves that are, at least superficially, indistinguishable from those of a single target oriented horizontally Figure 24A Figure 26D - Figure 26F. Thus, when presented with double-peaked anomalies it is well to examine other features. With systems such as the MetalMapper system that can measure the horizontal field components (B_x and B_y) we have noted that the behavior of the horizontal field component in the direction of cart movement provides an early indication of the presence of multiple targets by exhibiting multiple zero crossings. Gradient components such as B_{yz} also exhibit such multiple zero crossing. When they are available, these horizontal components are an invaluable aid in detecting multiple interfering targets. Even so, we conclude that it is very difficult to detect multiple targets when they are separated by a distance less than or equal to their depth of burial. Targets anomalies only become clearly separated (without significant interference, one to another) when they are separated by a distance of 4x their burial depth (See Figure 28D and Figure 29D).

4.3 Dipole Mapping Using a Tensor EM Gradiometer

4.3.1 Background

The terms ***dipole mapping***, ***dipole tracking***, and ***dipole localization*** originate from efforts of the U.S. Navy to detect and track submarines. Efforts to exploit measurements of the magnetic gradient tensor appeared in public literature as early as 1975 (Wynn, Frahm, Carroll, Clark, Wellhoner, & Wynn, 1975) and cite reports from Naval Ship Research and Development Center (Wynn W. , 1972) and the Naval Coastal Systems Laboratory (Frahm, 1972) that date the idea of locating and characterizing dipoles using the gradient tensor to 1972. The basic theory for so-called dipole mapping has been established for nearly 40 years and since that time, the major effort has been focused on developing a useful tensor magnetic gradiometer with sufficient portability, stability, and sensitivity for applications to various problems of interest not only for naval applications but also for environmental applications such as UXO detection. With regard to environmental and UXO applications, current efforts include the development of tensor magnetic gradiometers based on triaxial fluxgate technology by the USGS (Snyder & Bracken, Development and Testing of a Tensor Magnetic Gradiometer, 1995) (Smith & Bracken, 2004) and by the Naval Surface Warfare Center (Panama City, FL) (Wiegert & Oeschger, 2005). The aforementioned efforts have been funded in part by ESTCP and SERDP.

Dipole mapping is of particular interest for applications wherein real-time estimates of target location and dipole moment are important because implementations of the dipole mapping algorithms can perform the necessary calculations in a fraction of a second with portable computing devices. In this section, we will briefly outline a theory for dipole mapping using estimates of the tensor gradients. Then we will apply the theory to model data simulating a TEM gradiometer sensor and to experimental data acquired with a realization of such a TEM gradiometer.

4.3.1.1 *Dipole Mapping with a Gradiometer – Theory*

The basic theory for dipole mapping is outlined in (Wynn, Frahm, Carroll, Clark, Wellhoner, & Wynn, 1975) and more details can be found in the reports that are cited in that paper (Wynn W. , 1972) (Frahm, 1972). For completeness, we outline the theory here so that the reader may be able to understand the process without the need to refer to the references. The development here relies heavily on the original report of Frahm (Frahm, 1972) and the paper (Wynn, Frahm, Carroll, Clark, Wellhoner, & Wynn, 1975).

Refer to Figure 31 where we show a Cartesian coordinate system defined by coordinate axes ($x=x_1$,$y=x_2$,$z=x_3$). We have located a dipole with a moment **M** at the origin and our observation point is at P. The radius vector **R** extends from the origin to P and we have further defined a unit vector **n** in the direction of **R** and the distance $R=|\mathbf{R}|$ so that $\mathbf{R} = R\,\mathbf{n}$. Using this notation, we can define the magnetic field **H** and its gradient as shown below.

$$\vec{\mathbf{H}} = 3\frac{\left(\vec{\mathbf{M}}\cdot\hat{\mathbf{n}}\right)\hat{\mathbf{n}}}{R^3} - \frac{\vec{\mathbf{M}}}{R^3} \tag{6a}$$

$$\nabla\vec{\mathbf{H}} = -\frac{3}{R^4}\left[\left(\vec{\mathbf{M}}\cdot\hat{\mathbf{n}}\right)\left(5\,\hat{\mathbf{n}}\otimes\hat{\mathbf{n}} - \tilde{\mathbf{I}}\right) - \left(\vec{\mathbf{M}}\otimes\hat{\mathbf{n}} + \hat{\mathbf{n}}\otimes\vec{\mathbf{M}}\right)\right] \tag{6b}$$

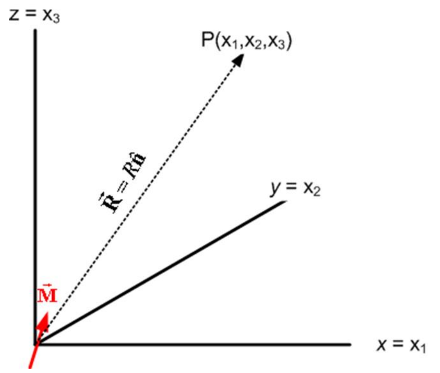

Figure 31: Observation coordinate system and definitions for formulation of dipole mapping problem.

In equation 6b, **I** is the identity matrix and the operator ⊗ represent the Kronecker (tensor) product of two vectors (Davis, 1994).

In our subsequent equations, we replace the vectors with their corresponding Cartesian components and we introduce the Einstein summation convention wherein the product of elements with the identical letter indices implies a sum over the range of those indices ($a_i b_i \Rightarrow \sum_{i=1}^{3} a_i b_i$)

Using this indicial or tensor notation, equation 6 can be rewritten as

$$H_i = \frac{M_j}{R^3}\left(3n_i n_j - \delta_{ij}\right) \tag{7}$$

In equation 6a, the symbol δ_{ij} is the kronecker delta ($\delta_{ij}=1$ if $i=j$ else $\delta_{ij}=0$).

We now introduce a short-hand notation for differentiation ($f_{i,j} \Rightarrow \frac{\partial f_i}{\partial x_j}$). Using this notation, we can define the gradient of the magnetic field ($H_{i,k}$)

$$\begin{aligned} H_{i,k} &= -\frac{3M_j}{R^4}\left(5n_i n_j n_k - \delta_{ij}n_k - \delta_{ik}n_j - n_i\delta_{jk}\right) = -\tilde{M}_j N_{ijk} \\ \tilde{M}_j &= \frac{3M_j}{R^4};\quad N_{ijk} = \left(5n_i n_j n_k - \delta_{ij}n_k - \delta_{ik}n_j - n_i\delta_{jk}\right) \end{aligned} \tag{8}$$

In equation 8, we have introduced a new vector $\tilde{M}_j$ that we can call the “reduced moment”, and a 3rd rank tensor N_{ijk} that is a function only of the elements of the unit vector **n**. In general, there are 3 independent elements in $\tilde{M}_j$, but because of the constraint |**n**|=1, there are only two independent components for **n**. That is, if we know any two components of **n**, we can always calculate the value of the third using the constraint. Therefore, in terms of the components of the “reduced moment” ($\tilde{M}_j$) and the unit vector (n_i) equation 8 shows that the magnetic gradient tensor can be expressed in terms of 5 unknowns, 3 unknown components of the reduced moment plus two (independent) unknown components of the unit vector **n**.

Also notice that the third rank tensor N_{ijk} has the property of symmetry with the interchange of any two of the three indices. Secondly, its trace for any two indices, and by extension therefore all three indices is always 0.

We define a second 3rd rank tensor

$$\tilde{N}_{ijk} = \frac{3}{2} n_i n_j n_k - \frac{1}{2}\left(\delta_{ik} n_j + \delta_{jk} n_i\right) \tag{9}$$

Like its counterpart N_{ijk} this new tensor is symmetric about pair of indices. Moreover, the coefficients (i.e., 3/2 and ½) were selected so that

$$N_{ijk}\tilde{N}_{jkl} = \delta_{il}\,. \tag{10}$$

In a sense, the third rank tensor $\tilde{N}_{ijk}$ behaves as the inverse of N_{ijk}.

Multiplying equation 8 from the right by $\tilde{N}_{ijk}$ and using the symmetry properties of N_{ijk} together with equation (10), we can solve for the 3 elements of the reduced moment ($\tilde{M}_j$) in terms of the elements of the magnetic gradient tensor and the third rank tensor $\tilde{N}_{ijk}$

$$\tilde{M}_j = -H_{i,k}\tilde{N}_{ikj} \tag{11}$$

Equation (11) expresses the 3 components of the unknown reduced moment in terms of the (as yet) unknown unit vector **n** that defines the direction between the source location and the observation point P.

Finally, we can insert equation 11 above into equation 8 to obtain a relation that only involves the unknown elements n_i and the observed gradient elements $H_{i,k}$

$$H_{i,k} = -\tilde{M}_j N_{jik} = \left(H_{l,m}\tilde{N}_{lmj}\right) N_{jik} \tag{12}$$

Since the gradient tensor is symmetric, at any particular observation point there exists a coordinate system in which the tensor consists only of diagonal elements. The value of these elements and the orthogonal transformation (a rotation of coordinates) that will transform the tensors and vectors into this *principal coordinate system* can be found by performing an eigen analysis.of the gradient tensor expressed in its observation coordinate system. We suppose that this has been done with the result that an orthogonal transformation operator T_{ij} has been found such that we can write the following relations:

$$\begin{aligned} H'_{i,j} &= \lambda_{(i)}\delta_{ij} = T_{il}H_{l,m}T_{j,m} \text{ (no sum on index } i\text{)} \\ n'_i &= T_{ij}n_j \end{aligned} \tag{13}$$

In equation 13, $H'_{i,j}$ and n'_i represent the expression of the gradient tensor ($\nabla\vec{\mathbf{H}}$) and the unit vector ($\hat{\mathbf{n}}$) in the principal coordinate system. The values $\lambda_{(i)}$ represent eigenvalues.[11] Although in general there are 3 eigenvalues for the problem, in the case of a potential field, the trace of the gradient tensor is always 0 (i.e. $\lambda_1+\lambda_2+\lambda_3=0$) so there can only be two independent eigenvalues.

Expressing equation 11 in the principal axis coordinate system and using equation 13 to simplify yields a tensor equation for the reduced moment

$$\tilde{M}'_j = n'_j\left(\lambda_{(j)} - \frac{3}{2}\lambda_k n'^2_k\right); \text{ (No sum on j)} \tag{14}$$

We insert equation 14 into equation 12 expressed in the principal coordinate system to get

$$\begin{aligned} 2\lambda_{(l)}\delta_{lm} &= -\lambda_j\left[\nu_j\left(n'_l n'_m + \delta_{lm}\right) - 2\left(\lambda_{(j)}\delta_{jl} + \lambda_{(j)}\delta_{jm}\right)n'_l n'_m\right] \\ \nu_j &= n'^2_j \end{aligned} \tag{15}$$

The left hand side is a diagonal tensor and the right-hand side is obviously symmetric in the two free indices (*l,m*). Therefore, we can write three independent equations for the unknown components n_i’ (unit vector along **R** expressed in the principal coordinate system) for the off-diagonal tensor elements. Those equations are:

$$\left[\lambda_j\nu_j - 2\left(\lambda_1+\lambda_2\right)\right]\nu_1\nu_2 = 0 \tag{16a}$$

$$\left[\lambda_j\nu_j - 2\left(\lambda_2+\lambda_3\right)\right]\nu_2\nu_3 = 0 \tag{16b}$$

$$\left[\lambda_j\nu_j - 2\left(\lambda_1+\lambda_3\right)\right]\nu_1\nu_3 = 0 \tag{16c}$$

There are only two equations for the diagonal elements since $\lambda_1+\lambda_2+\lambda_3=0$. These equations are

$$a\nu_1^2 + b\nu_1\nu_2 + \left(b-2a\right)\nu_1 + b\nu_2 + a - b = 0 \tag{17a}$$

$$a\nu_1\nu_2 + b\nu_2^2 + a\nu_1 + \left(a-2b\right)\nu_2 + b - a = 0 \tag{17b}$$

where

$$a = 2\lambda_1 + \lambda_2 \tag{18a}$$

---

[11] We enclose a repeated index in parentheses to indicate that we have suspended the implicit summation over the index values.

$$b = \lambda_1 + 2\lambda_2 \tag{18b}$$

In writing equations 17d and 17e, we have used the relations

$$\nu_3 = 1 - \nu_2 - \nu_3 , \tag{19a}$$

and

$$\lambda_3 = -(\lambda_1 + \lambda_2) . \tag{19b}$$

Equations 19a and 19b are a consequence of the fact that |**n**|=1 and $\lambda_1 + \lambda_2 + \lambda_3 = 0$.

There are 6 solutions to equations 16, the equations for the off-diagonal terms of the gradient tensor expressed in the principal coordinates:

$$\nu_1 = 0; \nu_2 = 0; \nu_3 = 1 \tag{20a}$$

$$\nu_1 = 0; \nu_2 = 1; \nu_3 = 0 \tag{20b}$$

$$\nu_1 = 1; \nu_2 = 0; \nu_3 = 0 \tag{20c}$$

$$\nu_1 = 0; \nu_2 = \frac{b-a}{b}; \nu_3 = \frac{a}{b} \quad (b \neq 0) \tag{20d}$$

$$\nu_1 = \frac{a-b}{a}; \nu_2 = 0; \nu_3 = \frac{b}{a} \quad (a \neq 0) \tag{20e}$$

$$\nu_1 = \frac{a}{a-b}; \nu_2 = -\frac{b}{a-b}; \nu_3 = 0 \quad (a \neq b) \tag{20f}$$

Except for trivial cases, we can eliminate the first three solutions (20a-20c) because, in general, they do not satisfy equations 17. So we must look to the last 3 solutions (20d-20f) as possibilities.

We use eigen analysis to determine the (eigenvalue) gradients in the principal coordinate system. And from the corresponding eigenvectors we are able to construct the transformation tensor T_{ij} (see equation 13) that allows us to transform between the principal coordinate system and the observation coordinate system. However, there is an ambiguity between the two systems that depends on the ordering of the three eigenvalues. This ambiguity can be eliminated by ordering the eigenvalues such that

$$\lambda_1 \lambda_2 \geq 0 , \tag{21a}$$

and

$$|\lambda_1| \geq |\lambda_2| \tag{21b}$$

The ability to always order the eigenvalues consistent with equations 21 is a consequence of the traceless nature of the gradient tensor which demands that, in general, two of the eigenvalues must have the same sign and be opposite in sign from the third. The only other possibility is that one of the eigenvalues is zero and the other two are equal but have opposite signs. As a consequence of ordering of the eigenvalues in this way, a and b defined in equation 18, will satisfy

$$ab \geq 0 \ , \qquad (22a)$$

and

$$|a| \geq |b| . \qquad (22b)$$

With the qualifications implicit in equations 22, it follows that only solution 20e satisfies both equations 16 and 17.

4.3.1.2 *Solution for the Direction from the Source Point*

Equation 20e provides the solution for the squares ($\nu_1 = n_1'^2 ; \nu_2 = n_2'^2$) of the 2 components of the unit vector **n** from the source point (origin in Figure 31) to the observation point P (Figure 31). However, since we desire the components themselves, we are obliged to take the square root of these positive real values. Thus, from equation 20e, we get the relations

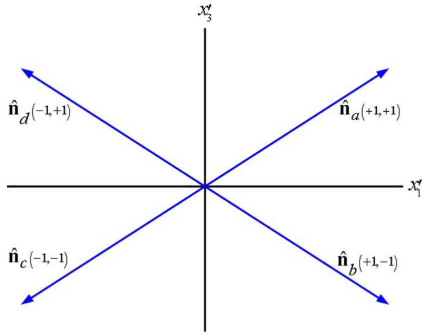

Figure 32: The 1-3 plane of the principal coordinate system showing the 4 possible solutions of the dipole

$$n_1' = \pm\sqrt{\frac{a-b}{a}} \qquad (23a)$$

$$n_2' = 0 \qquad (23b)$$

$$n_1' = \pm\sqrt{\frac{b}{a}} \qquad (23c)$$

The consequence of the sign ambiguity that is introduced by the need to take the square root of these positive solutions is that there, in general, four solutions to the bearing vector as shown in Figure 33. We have labeled the solutions *a*-*d* according to the quadrant indicated by the choice of signs. Once the solutions have been transformed back into the observation coordinate system, it is easy to eliminate two of them since, for all geophysical problems the target must lie beneath the observation plane. However, that still leaves a "ghost" solution that must be distinguished from the real solution in order to "track" the correct solution.

4.3.1.3 *Solution of the Reduced Moment*

Using equations 20e and 23 together with equation 14, we find that there are also 4 moments that have a one-to-one correspondence with the 4 solutions to the bearing vector. After some algebra, these moments may be written in terms of the two parameters a and b

$$\tilde{M}_1' = \pm\frac{1}{3}(5b-a)\sqrt{\frac{a-b}{a}} \qquad (24a)$$

$$\tilde{M}_2' = 0 \qquad (24b)$$

$$\tilde{M}_3' = \pm\frac{1}{3}(5b-4a)\sqrt{\frac{b}{a}} \tag{24c}$$

In Figure 33, we depict the vector solutions together. Although there is a one-to-one correspondence between each bearing vector **n** and a reduced moment vector **M**, they do not necessarily lie in the same quadrants. In Figure 33, we have arbitrarily drawn them that way. But the actual quadrant to which a particular moment vector lies depends on the sign of the terms (*5b-a*) and (*5b-4a*) in equations 24a and 24c. The ordering of the eigenvalues according to equations 21 does not guarantee the sign of these terms. Thus, all we can say is that for any particular solution for **n**, there corresponds a unique reduced moment.

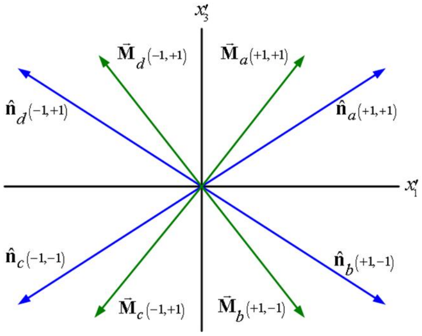

Figure 33: Dipole mapping solutions showing the 4 solution vector pairs (bearing vector n and the magnetic

4.3.1.4 *Computing Distance (R)*

The magnetic gradient tensor is symmetric and its trace is always zero. Thus, it contains only 5 independent pieces of data. In developing this theory for dipole mapping, we have been able to solve the resulting equations by reducing the number of unknown parameters for the gradient tensor from 6 to 5. We combined the moment vector with all references to the unknown distance from the source point to the observation point calling the resulting vector ($\vec{\tilde{\mathbf{M}}}$) the ***reduced moment*** so called because it implicitly contains the 6th unknown (*R*). How then do we now calculate the last unknown? There are many ways to accomplish this. All require the observation of at least one more independent piece of data. Here, we will assume that we have estimates of the vector magnetic field **H** produced by the unknown dipole. The vector magnetic field actually contains 3 independent pieces of data (H_x , H_y , and H_z).

We suppose that we have observed the gradient tensor $\nabla\mathbf{H}$ and the corresponding vector magnetic field $\mathbf{H}$ at the field point. And from our analysis of the gradient tensor, we have calculated values for the bearing vector **n** and the reduced moment $\tilde{\mathbf{M}}$. We have expressed these vectors in the observation coordinate system by transforming their values as determined in the principal coordinate to the observation coordinates using the coordinate transformation we can derive from the results of the eigen analysis of the observed gradient tensor.

Euler's Theorem: One can relate any homogeneous function to its derivative using Euler's theorem for homogenous functions (http://en.wikipedia.org/wiki/Homogeneous_function). The Euler theorem has been used for decades by geophysicists as an aid for determining the depth of source when interpreting passive magnetic and gravity fields (Thompson, EULDPH: A new technique for making computer assisted depth estimates from magnetic data, 1982) (Reid, Allsop, Granser, Millett, & Somerton, 1990). Potential fields are comprised of homogeneous polynomials and therefore Euler's theorem applies to all potential fields. As it applies to an arbitrary anomalous magnetic field **H**, we can write a general Euler's relation

$$\vec{\mathbf{R}}\cdot\nabla\vec{\mathbf{H}} = -k\vec{\mathbf{H}} \tag{25}$$

where k is called the *degree of homogeneity* in mathematical terminology and the *structural index* in its application to geophysical problems. For a magnetic dipole the structural index is *k=3*.

If we write $\mathbf{R} = R\mathbf{n}$ and substitute into equation 15, we can get three equations that can be independently solved for the scalar value R for the distance to the target

$$\begin{aligned} &R(\mathbf{n}\cdot\nabla\mathbf{H}) = -3\vec{\mathbf{H}} \text{ or,} \\ &R = -3\frac{H_k}{n_i H_{i,k}} \ (k = 1,2,3) \end{aligned} \tag{26}$$

4.3.1.5 *Dipole Mapping Algorithm- Computation Steps*

Here, we summarize the steps involved in the dipole mapping algorithm.

1. Using the observed magnetic gradient tensor, perform an eigen analysis to find the 3 eigenvalues plus the eigenvectors.
2. Determine the order of the eigenvalues (λ_i) according to equations 21. Then using the eigenvectors, determine the transformation tensor T_{ij} that will transform vectors from the observation coordinate system to the principal coordinate system and vice versa.
3. Calculate the components of the bearing vectors **n** in the principal coordinate system using equation 23. This results in 4 separate solutions.
4. Calculate the components of the reduced moment vector ($\tilde{\mathbf{M}}$) expressed in the principal coordinate system. There will be 4 such moment vectors that pair with each of the 4 bearing vectors calculated in step 3.
5. Transform the bearing vector/reduced moment vector pairs back to the observation coordinate system. Eliminate 2 of the bearing vectors based on the constraint that a valid solution must have a bearing vector that points down (rather than up). This leaves two feasible solutions, one of which is the ghost.
6. Use the Euler relation (equation 26) together with the measurement of one or more components of **H** to determine the range scalar R.
7. Perform other tests to decide which of the two remaining solutions is the real one and which is the ghost.

4.3.2 Experimental Demonstration

We have implemented the dipole mapping algorithm described above using high-level Mathematica code and we tested the code with synthetic data. Results of synthetic tests to study the effects of using a finite gradiometer together with various physical and electronic imperfections were presented in the White Paper (George & Snyder, A Study of the Feasibility of a Tensor TEM Gradiometer for UXO Detection and Characterization, 2007) we submitted early in this project. Here, we present results from two synthetic models and two experimental models. Our model is the same 60mm prolate spheroid that we used earlier in this report (Section 4.2) to study resolution.

4.3.2.1 *Synthetic Models Using Theoretical Magnetic Gradient*

As in our earlier resolution study (Section 4.2), we calculated the theoretical fields and gradient tensor over a 60mm prolate spheroid with a 3:1 aspect ratio (length = 180mm). We computed fields and gradients along a centerline profile directed along the y-axis. We processed synthetic data for two target attitudes, horizontal and inline with the profile, and vertical. The results are displayed, respectively, as Figure 34 and Figure 35. The results from these calculations confirm that the algorithm is operating correctly. In both cases, the algorithm correctly predicts the target position and moment. The vectors illustrate the strong anisotropic polarizability of the target wherein we see that the induced moment from the horizontal target (Figure 34) remains largely horizontal until the target point is inside the transmitter loop ($|y|<0.5$m). In contrast, the induced moment for a vertical target (Figure 35) remains mostly vertical until target is noticeably outside the footprint of the transmitter loop ($|y|>0.5$m).

4.3.2.2 *Dipole Mapping Results – Experimental Data*

We acquired a number of data sets with the finite gradiometer antenna array described earlier in this report. The array consists 4 tri-axial receiver cubes arranged in a cruciform pattern with an effective differencing baseline of 20cm. Targets were moved dynamically beneath the antenna array while the associated induced fields were sampled continuously at a rate of 10 samples/sec. The resulting data were post-processed to remove the background and estimate the independent elements of the gradient tensor at each field point. The resulting data were then input into our dipole mapping algorithm. Results for two different targets are shown in Figure 36 and Figure 37.

Figure 36 shows dipole mapping results where the target was a 100mm steel sphere. The sphere was moved along a plane (ground surface) that was approximately 70 cm below the plane of the antenna array. The figure shows that the dipole mapping algorithm is able to correctly estimate the position and moment over an interval of approximately 1 m centered on the position of the antenna array.

Figure 37 shows results for a similar experiment conducted using a 60mm mortar round as the target. The mortar was placed at a pitch angle of -45^0. As with the previous example, dipole mapping is able to correctly estimate the targets position and moment over an interval of more than 1m. In this case, notice the asymmetry in the dipole mapping results (Figure 37 lower right). The dipole moments seem to remain stronger and are more vertical for values of y>0 as compared with values on the negative end of the profile. This behavior is consistent with the fact that with a 45° pitch angle, the target will be illuminated along its long axis by the primary magnetic field longer on one side than the other. This behavior is hardly noticeable when viewing the profiles (left side Figure 37).

4.3.3 Dipole Mapping – Summary Remarks

Dipole mapping is a powerful tool for locating and characterizing a dipole source field. The algorithm we describe is relatively simple to implement. The calculations involved take less than 1ms/data point (2.8GHz Intel Xeon processor). The algorithm produces accurate estimates of target depth and moment from dynamic data when the target is sufficiently near that the signal-to-noise ratio is good (>10). Typically, this places the target within a horizontal radius of approximately 0.7m and at a depth that is less than 11 times its diameter (11x rule). The experimental results demonstrate that we can generate good estimates of the gradient tensor from an array of induction sensors with a small baseline (20cm). Assuming, that the antenna array is raised 15-20cm above the ground surface, the gradients estimates will be reasonable for targets at depths $|z|>0.25$m (approximately 2x the 20cm baseline). Although we have not done so either in our numerical model studies or in the processing of our experimental data, the estimation of the polarizability tensor is straight forward when we are given estimates of the position of the source and the corresponding dipole moment. Such calculations would require that we buffer a number of sequential dipole mapping solutions for a particular target as we traverse across it. And even so, the polarizability tensor would be imperfectly resolved since the linear motion along a profile would not guarantee that the target would be adequately illuminated by the primary field along all 3 principal axes.

Dipole tracking is clearly not appropriate for static “cued ID”. When it takes 10-20sec to stack data, it is not of particular concern if the subsequent inversion takes another 10-20 sec. Consequently, conventional non-linear inversion methods that can be applied to one or more spatial data points provide very robust solutions of the target characteristics. However, the speed with which the dipole tracking solutions can be obtained makes the algorithm ideal for use in situations requiring real time reporting. The time it required to process each data point (i.,e., subtract background, perform differencing calculations, calculate dipole mapping solution, and ultimately display the results) will no doubt be on the order of 10ms. Our data acquisition computer can easily maintain an acquisition sample rate of 10 samples/sec while it is continually updating a display that shows the target position, depth, and an estimate of its RMS polarizability.

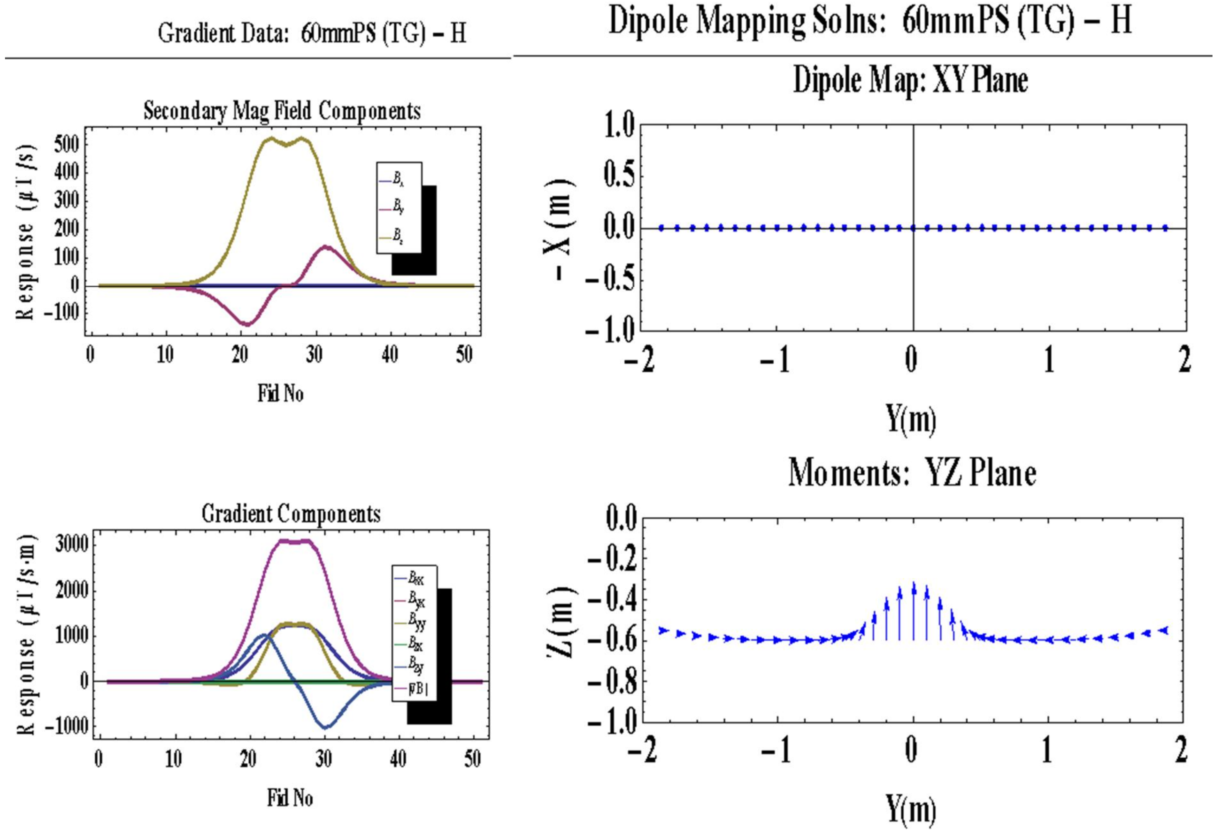

A) Synthetic Data **B) Dipole mapping results**

Figure 34: Dipole mapping results for synthetic data. The target is a 60mm prolate spheroid with a horizontal axis along the y-axis and a depth of -0.6m. The synthetic data are shown in the panels to the left. The dipole mapping results are on the right. The cross-section (lower right) displays the resulting moments with the tail of the vector plotted at the predicted depth. Note how the moment vectors transition from mainly horizontal for |y|≥0.5m (outside the transmitter loop) to mainly vertical for |y|<0.5m (inside the loop).

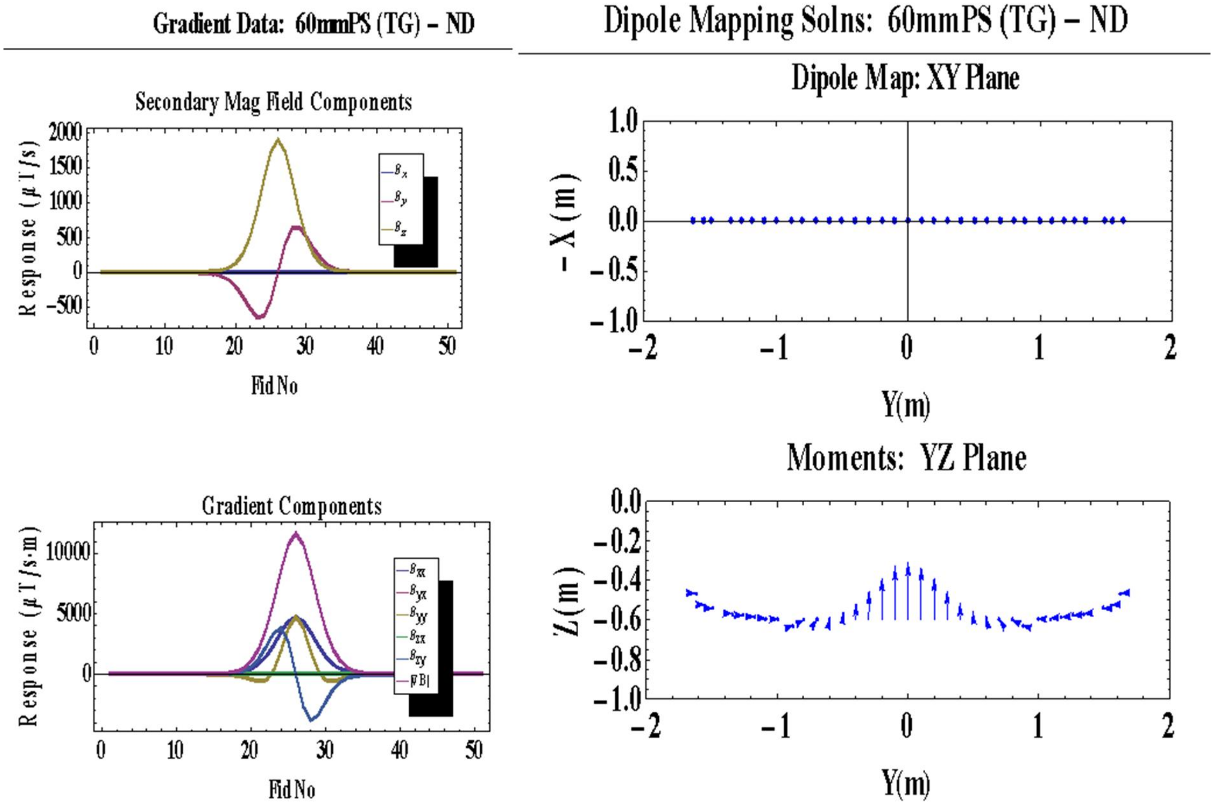

A) Synthetic data profiles

B) Dipole mapping plot

Figure 35: Dipole mapping results for synthetic data. The target is a 60mm prolate spheroid with vertical axis at a depth of -0.6m. The synthetic data are shown in the panels to the left. The dipole mapping results are on the right. The cross-section (lower right) displays the resulting moments with the tail of the vector plotted at the predicted depth. Note that the moment vectors continue to have a strong vertical component in the region immediately outside the transmitter loop (|y|≥0.5m). Compare with the behavior of the horizontal loop in Figure 34.

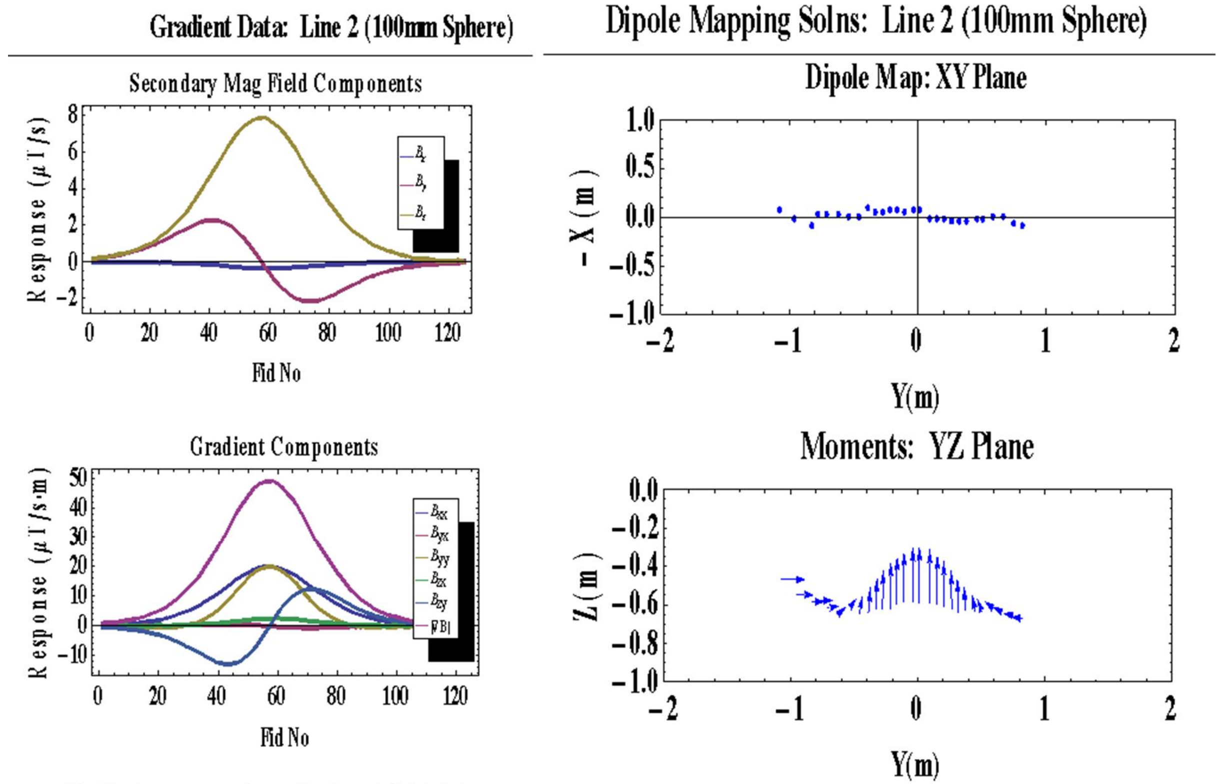

A) Post-processed gradient and field data

B) Dipole mapping results

Figure 36: Dipole mapping results from experimental data. The target is a 100mm diam. Steel sphere at a depth of approximately 65cm. The target was moved continuously while recording data. Note the symmetry of the moment vectors and the approximate uniform depth estimates over the interval -0.6≤Y≤0.6m.

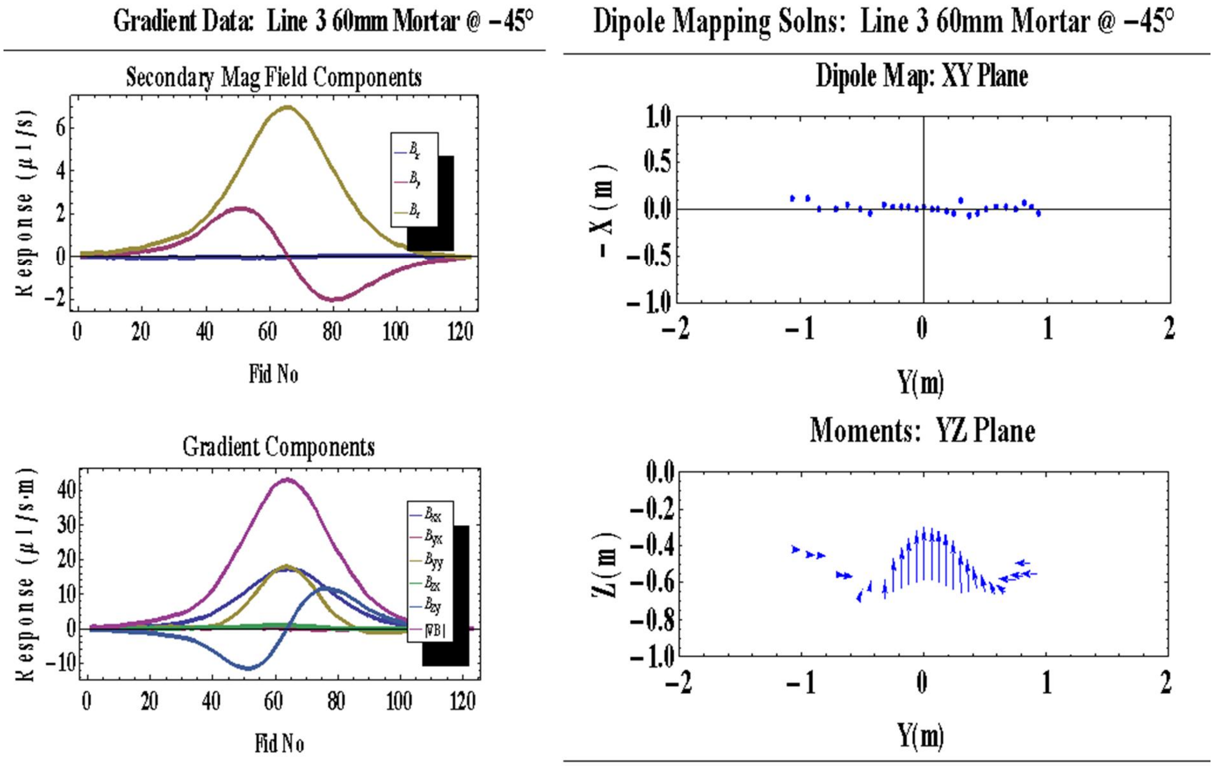

A) Post-processed gradient and field data

B) Dipole mapping results

Figure 37: Dipole mapping results from experimental data. The target is a 60mm mortar at a depth of approximately 65cm. The target was moved continuously while recording data. Note the distinct assymmetry of the moment vectors which are the result of the 45^0 pitch of the target. Also note the systematic (almost sinusoidal) undulations in the depth estimates over the interval $-0.4 \leq Y \leq 0.6$m.

5 Physical Experiments and Measurements

5.1 Proof-of-Concept Experiment

The objective of the Proof-of-Concept work was to experimentally investigate whether a spatial difference of a TEM signal can be reliably observed. The answer to this question, along with results of the numerical modeling study was a *Go-NoGo* milestone for this project. Raising the question of whether a *reliable* observation can be made is justified because TEM signals are typically small, and the difference between two such signals further decreases the signal amplitude.

Given that it is fundamental that signal amplitude is reduced in a difference signal compared to either signal alone, it is reasonable to ask if noise is a severe limitation in the proposed method. It is well-known that noise limits the sensitivity and accuracy of the TEM method, and taking a difference signal would seem to only exacerbate the problem. We submit, however, that the proposed method might actually mitigate the noise problem because the differencing can significantly reduce the noise and possibly increase the signal-to- noise ratio (SNR). Often the noise observed in a TEM measurement is a result of environmental electromagnetic noise (George & Snyder, Noise in Time Domain EM Systems, 2005). Such noise is produced by power lines, radio stations, natural sources (principally thunderstorms), movements of the TEM loop antennas in the earth’s magnetic field, and other sources. If the interfering source is some distance away from two receiving sensors, the noise field will be spatially uniform across the antenna array. Under such conditions, the noise will theoretically be eliminated when the signals from two (identical) sensors are subtracted. Although the signal amplitude will decrease as a result of differencing, there may actually be an improvement in SNR because the noise may be decreased even more.

Therefore, the main focus of this work was to evaluate SNR for both a ‘straight’ signal and a ‘difference’ signal. Since SNR has no accepted standards for TEM measurements, and since SNR is a function of time along a decay curve as well as other factors, we had no simple test to use. Instead, we observed typical signals and evaluated their SNR by the “eyeball” method. We fabricated two receivers and a circuit to produce a signal that is the difference between the outputs of the two receivers. We tested these receivers using the transmitter and data acquisition system from the Navy’s AOL system (G&G Sciences Inc., 2008).

The brief tests presented here unquestionably confirm our postulate that noise is decreased by differencing. Yet the amount of the noise reduction is a complicated function of many factors and parameters. In none of the cases we observed did SNR decrease when comparing the difference signal to either of the signals alone. But in one case, where a symmetrical target was symmetrically located so that the difference signal is theoretically zero, we did observe a poorer SNR in the difference signal.

The reduction in noise is a complicated function of site-specific conditions, particularly environmental noise characteristics at the time of the measurement, and, importantly, the choice of signal parameters such as base frequency, stacking, and gating (George & Snyder, Noise in Time Domain EM Systems, 2005). So, these variables when combined with a nearly unlimited set of geometries for transmitter, receiver, and target, complicates the answer to our postulated question.

5.1.1 Experimental Setup

To complete the needed measurements, we used two of our standard 10 cm tri-axial receiver *cubes*, an experimental transmitter loop that we had on-hand from earlier development of the AOL system, and the data acquisitions system and transmitter from the AOL system. Our tri-axial cube contains three loops arranged in an X,Y,Z configuration. The three loops were connected to an experimental preamplifier circuit that contained three individual amplifier circuits, one for each loop. We modified one preamplifier circuit board so that two of the circuits receive the signals from identical windings on two separate cubes while the third circuit electronically subtracts the signals from the other two circuits.

A block diagram of the hardware and the experimental setup is shown in Figure 38. We used the vertical Z loop of each cube. In the data presented, the signal from the first cube is identified as channel “0Y” while the signal from the second cube is identified as channel “0X.” The difference channel is identified as channel “0Z.” Note that In the amplifiers we took no special precautions to match gains from each of two loops within any of the amplifiers. We used component electronic components with 5% tolerance, so we expected gains of each channel to the same to within and error of ± 5% of each other. Therefore, the results represent the minimum performance gains we expected to gain from differencing. Later, in the second phase, when we

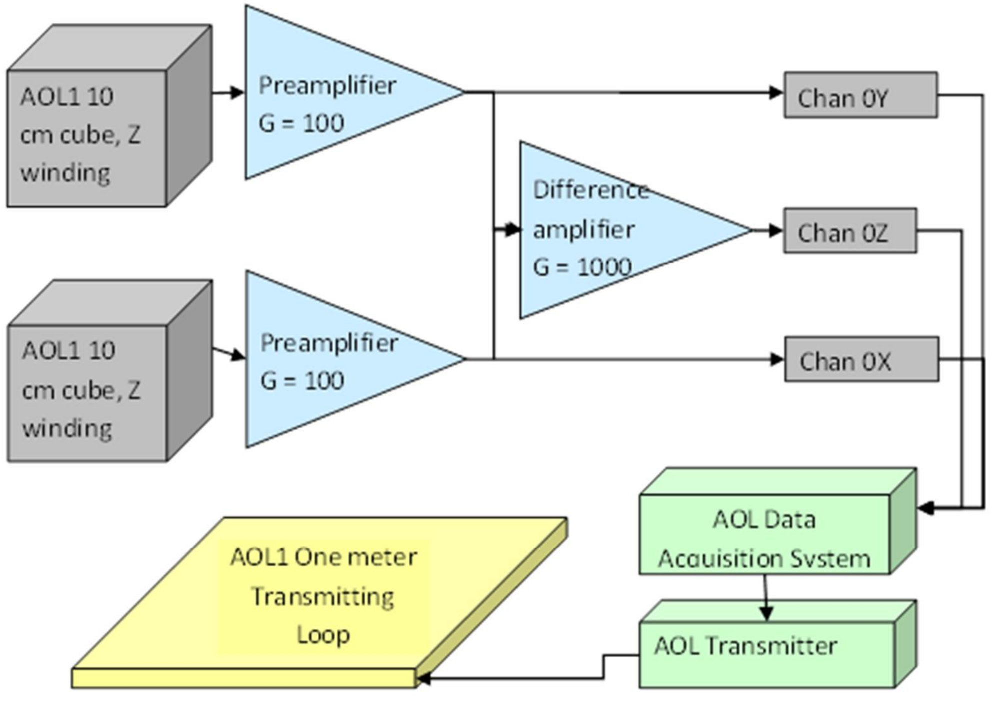

Figure 38: Block diagram of sensors and amplifiers used for Proof of Concept experiments.

constructed the antenna array, we used 1% components and provided trimming capabilities so that gains could be matched precisely. In the data for the Proof-of-Concept phase, 5% components were sufficient to demonstrate our contention that we could decrease noise and increase SNR.

A block diagram of the experimental setup was shown Figure 38. A picture of the loops and of the two cubes positioned for these measurements is shown in Figure 39. To eliminate responses from objects in the ground, we placed all components on a platform elevated about five feet above the ground. The transmitting loop is a 1-meter square loop from the original AOL system consisted of two sections of eight turns each. The photo also shows a 10 cm steel ball used for some of the measurements.

For these measurements, one cube was placed at the center of the transmitter loop and the other cube was placed 20 cm in one ordinal direction. In the data, the dB_z/dt field for the center cube appears in channel 0Z, the dB_z/dt field for the off-center cube appears in channel 0Y, the hardware difference between the two appears in channel 0X, and the software difference between the two appears in channel 1Z.

The cubes were oriented asymmetrically as shown rather than symmetrically across a baseline. This was done because a target located symmetrically under the transmitter coil and symmetrically under a pair of receiver coils would generate a zero difference signal.

In these tests we used two targets. The first target was a 10 cm steel sphere positioned directly below the center cube at a distance of 69 cm below the transmitting loop and 72 cm below the plane of the two receiving loops. The second target was a small aluminum ring: 2-in outside diameter by 0.25 in wide by 0.0625 in thick. The ring was placed 38 cm directly below the "X" (offset) receiver cube.

Figure 39: Picture of experimental setup. The near cube is located at the center of the transmitter loop. The far cube offset by 20 cm. The Z coils (vertical axis) were used on each cube.

5.1.2 Observations

We began our experiments with observations of raw background signal with no target and proceeded to observations of stacked and decimated transients from targets. The objective of these observations was to tabulate improvements or degradations in the SNR for a few sample tests as differentiated from statistically evaluating the overall efficacy of the method.

5.1.2.1 *Noise Reduction – Raw Signals*

Typical time signals from the two sensors and their difference are shown in Figure 40. The signals from the two sensors appear almost identical. The large peaks occur 8.33 ms apart, which identifies them as noise spikes from a power line. Although the signals appear identical at this scale, there are differences that can be seen when one looks closer. The difference signal is shown in the lower part of the figure. This signal is impressive -- it appears to have eliminated all of the power line spikes.

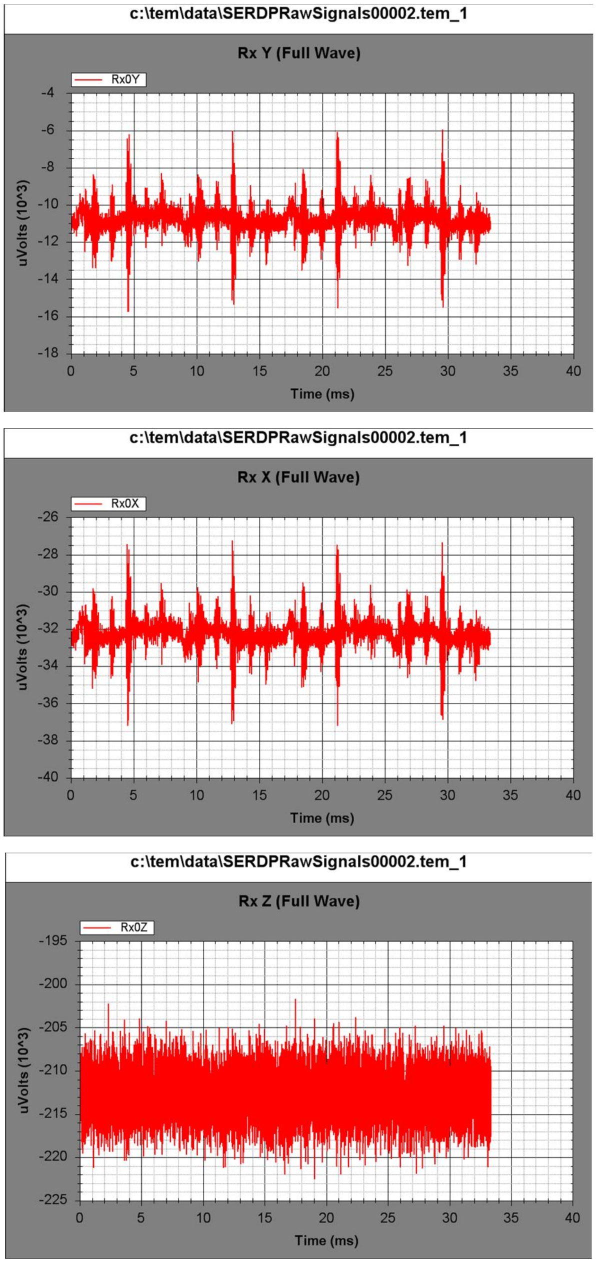

Figure 40: Background signals observed. Rx Y is signal from one sensor. RxX is signal from the other sensor. RxZ is the difference signal with a gain x10 more than the others. No stacking or averaging was done to these signals. The ordinate is microvolts multiplied by 10^3, or equivalently, millivolts.

This example indicates our best expectations. We would expect that the signals from each of the sensors would have at least two components: a received and perfectly correlated component that is uniform environmental noise, and an internal and perfectly uncorrelated component that is thermal noise. The correlated components should subtract and the uncorrelated components should add. The difference signal in Figure 40 is significantly less than 10 times either of the other signals and its appearance is consistent with our preconceptions. While the sensor signals appear to be dominated by 60Hz environmental noise, that noise is effectively eliminated in the difference, and it appears to be dominated by wideband electronic (thermal) noise. This is what we want because thermal noise **should** be the limiting noise, presuming that we have kept thermal noise to a low level.

These signals are further investigated in Figure 41. This figure is the Fourier Transform of the same signals, although over longer blocks (i.e., a longer time period). These spectra are a stack of 300 spectra, each from a 0.3 sec time block of data. In these spectra, the spectral peaks are from repetitive signals, such as power lines, while the baseline is random noise, either environmental random noise or electronic noise. The blue and green traces (overlaying one another) show many spikes while most of the spikes have been

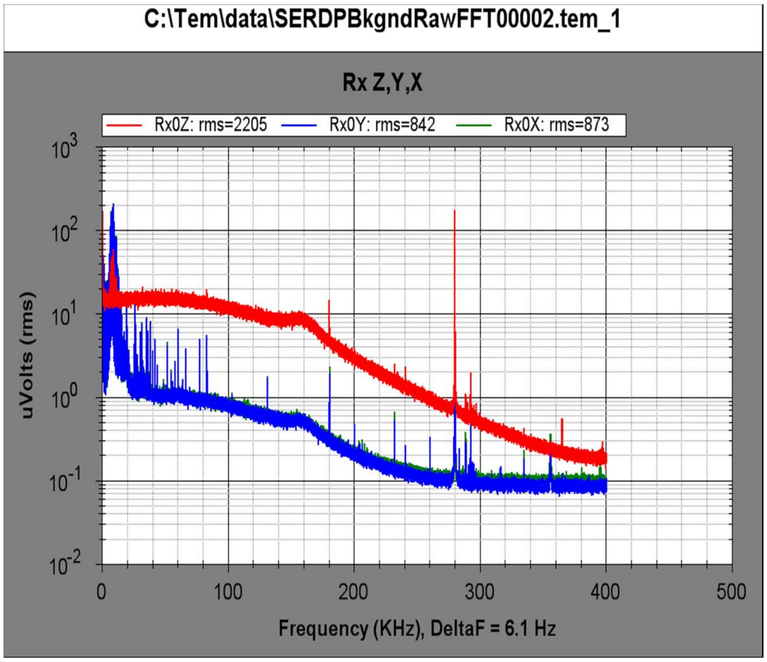

Figure 41: Frequency spectra of signals similar to those in Figure 40. Note that the difference signal (red trace) was amplified by x10 compared to the others.

eliminated in the red trace. In particular, the *swarm* of noise spikes representing power-line signals below about 20 KHz has been substantially attenuated. [12] Note that the baseline, representing random noise for the difference signal, is roughly √2 times the sum of the other two baselines (after considering the x10 gain difference), which confirms our claim that the baseline is due to thermal noise. If the baseline were due to random environmental noise, such as lightning, that noise would also subtract in the difference signal. There is, perhaps, some reduction in the baseline level below 60 KHz, where we expect random environmental noise to be largest. But since the receiver loops were measuring vertical field, they are insensitive to propagating EM noise from lightning. Receiver loops that measure horizontal fields are more sensitive to propagating EM noise. The shape of the baseline above 150 KHz is produced by the anti-aliasing filter in the data acquisition system. The fact that the two baselines converge at high frequencies identifies high frequency noise in the blue and green traces as data acquisition noise, probably digitization noise.

The random noise, thermal noise here but probably lightning noise in seasons and times of day when noise is higher (Chrissan & Fraser-Smith, 1996), (Maxwell & Stone, 1963), is the limiting factor in any of these measurements. We note that the baseline noise in a single amplifier is about 1 μV rms for either sensor alone and about 15 μV rms for their difference. Given that the sensor preamplifiers have a gain of 100, the difference amplifier has a gain of 1000, and the *bin* width for this spectrum is 6.1 Hz, we can compute the noise level at the input to the preamp. That noise level is 40 nV/√Hz, which is equivalent to the thermal noise produced by a 1.0 Kohm resistor. This level of noise performance is reasonable and consistent with the design of our preamplifier. We believe that thermal noise could be reduced by 10 dB or so (to an equivalent resistance level of 100 ohm) with additional development of receiver loop and preamp designs. But this 10 dB is the most we could expect to gain with additional work. Since 10 dB is often inconsequential in TEM measurements that have dynamic ranges of many 10's of dB's, we believe the existing performance was adequate for this project.

5.1.2.2 *Noise Reduction – Stacked and Decimated Signals*

---

[12] The large spike at 280 KHz is from a power supply in our transmitter. Following these tests, we identified that source of noise and reduced it to an inconsequential level.

The discussions above have been based on the raw signal and noise that is received. It is more important to compare noise that would actually be observed in a TEM measurement. Typically, we stack a minimum of several cycles of a waveform and we then decimate (i.e. sum discrete samples into time gates). The objective of this stacking and decimation is to reduce observed noise. The resultant decay curve has an *effective* noise sensitivity function that is a function of frequency (George & Snyder, Noise in Time Domain EM Systems, 2005) and is controlled by the selection of stacking and decimation parameters. Stacking at an appropriate base frequency effectively reduces 60 Hz components and harmonics. Decimating effectively reduces wideband noise at higher frequencies.

To demonstrate, we show the responses that are observed from the 10cm steel sphere target located 67 cm below the center cube. Figure 42 shows the responses that are observed with the simplest possible stacking, that is the stack of a single cycle. The early time response up to about 70 µs is receiver overload caused by direct coupling of the transmitter primary signal into the receivers. The decay from about 70 µs to about 800 µs is the signal from the steel sphere. The signal at later times is the *stacked* noise that is still present after the signal has died away. In this case the noise still shows some remnants of 60 Hz spikes. We know from observation that these spikes are effectively reduced by stacking more cycles as we typically do.

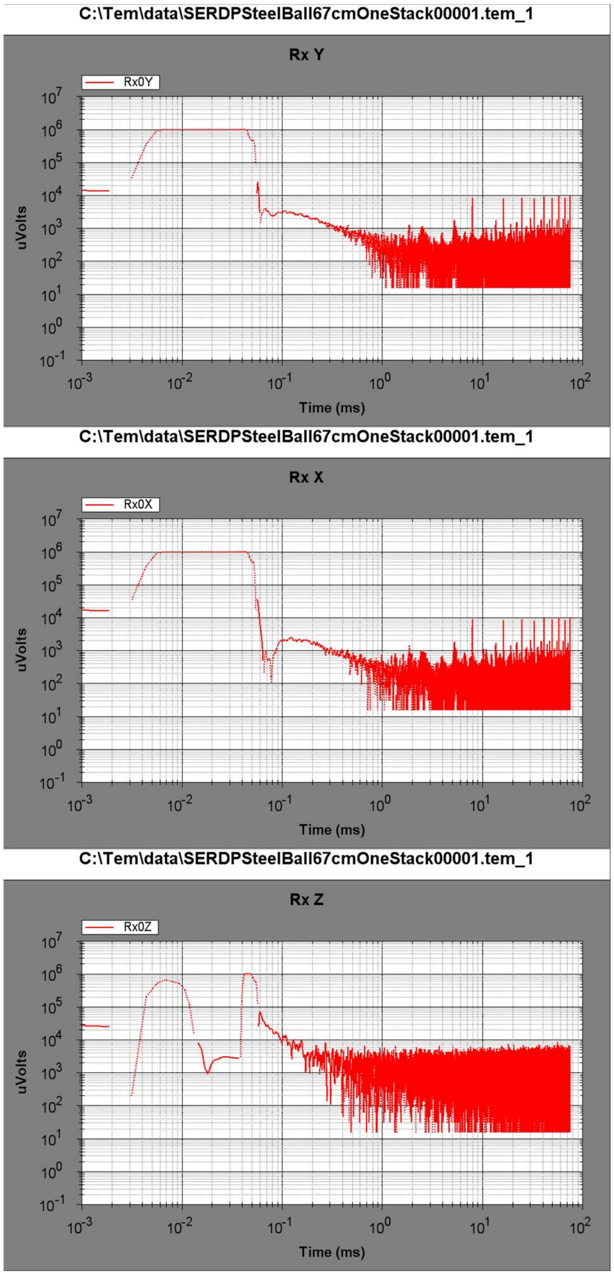

Figure 42: Simply stacked response from a 10 cm sphere. Top two graphs are individual sensors, and bottom graph is the difference.

The difference signal in the lower section Figure 42 of *appears* to be noisier than the sensor signals in that the difference transient disappears into the noise at an earlier time. In this case however, the difference transient has a faster decay rate than both of the direct transients and, in one respect, it has a better SNR. The difference transient is observable over about a full decade in magnitude while direct transients are observable over something less than a decade.

As mentioned earlier, final results should be based on signals that are both stacked **and** decimated. Stacked and decimated results are shown in Figure 43. In this figure, signals from both sensors and the difference signal are displayed in the same plot. The signals shown are a simple stack of a single cycle of signal (one positive and one negative decay), like the signals in Figure 42, followed by decimation into time gates that are so-called 5% time gates. A 5% gate is a gate whose width is 5% of the time delay at which it occurs.

Two cases are shown in Figure 43. The top half shows a signal from the steel sphere corresponding to Figure 42. For comparison, the bottom half is for the small aluminum ring target that was located at 38 cm below the offset (X) receiver cube. This last one is a good example of a decay curve that is somewhat noisy for each of the two individual sensors, but has much better SNR for the difference signal.

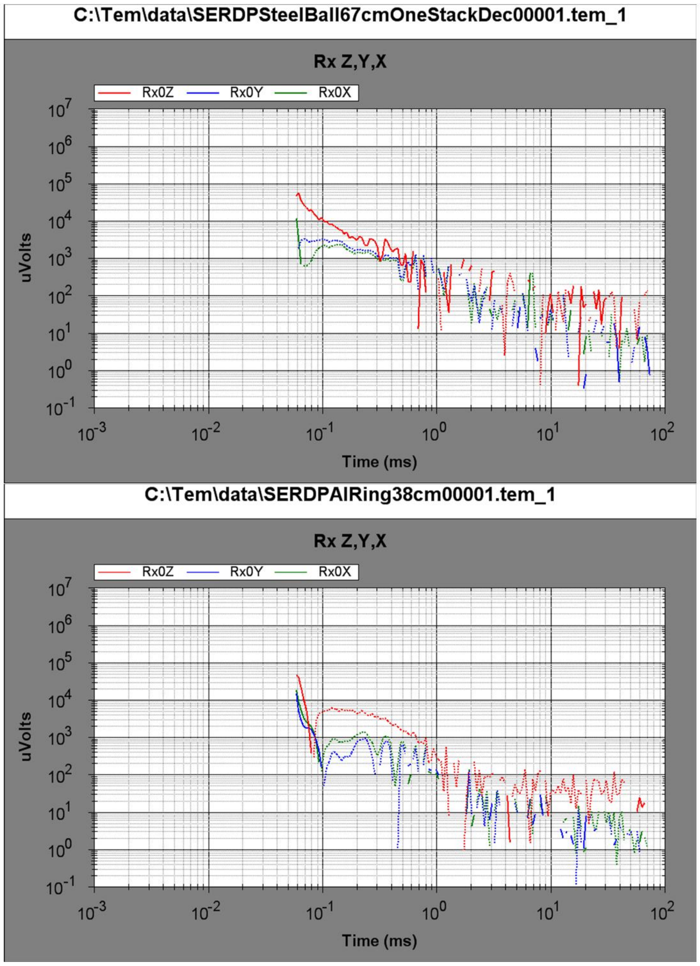

Figure 43: Responses using decimated time gates: Top response is one stack from a 10 cm steel sphere and bottom response is 10 stacks from a small Aluminum Ring. Rx0Z is the difference signal.

5.1.2.3 *Hardware versus Software Differencing*

A secondary objective of this work was to compare two methods of signal differencing: hardware and software. An advantage of hardware subtraction is that fewer channels are required if only the difference signal is digitized; but that becomes a disadvantage when both the individual signals and their difference signal are desired. An advantage of software subtraction is that fewer channels are required in order to acquire both the difference signal and the individual sensor signals. But the dynamic range of software subtraction is limited by the bit-resolution of the analog-to-digital converters used to digitize the signals and represents the case where any errors between two channels would be maximum. On the other hand, software subtraction provides the ability to routinely compare the signals from each of the sensors and to compensate for gain differences and changes in the two channels.

We made several comparisons of the hardware and software methods of obtaining the difference signal but every comparison resulted in the same conclusion: hardware subtraction did not offer significant improvement over software subtraction. In fact, in every test we did, hardware subtraction and software subtraction offered virtually identical signals. An example is shown in

Figure 44. The two signals are virtually identical. Since we believe it advantageous to have both signals as well as the difference signal, and since software subtraction involves less hardware, we used software subtraction for the following stages of work on this project.

In all of these comparisons, we took no extraordinary precautions to match hardware components or to measure differences in gains before making software subtractions. The data we have presented represents the minimum improvement we expect to gain by using pair of sensors. With additional time and effort, we believe we could make the advantages offered by sensor-pair subtraction even better.

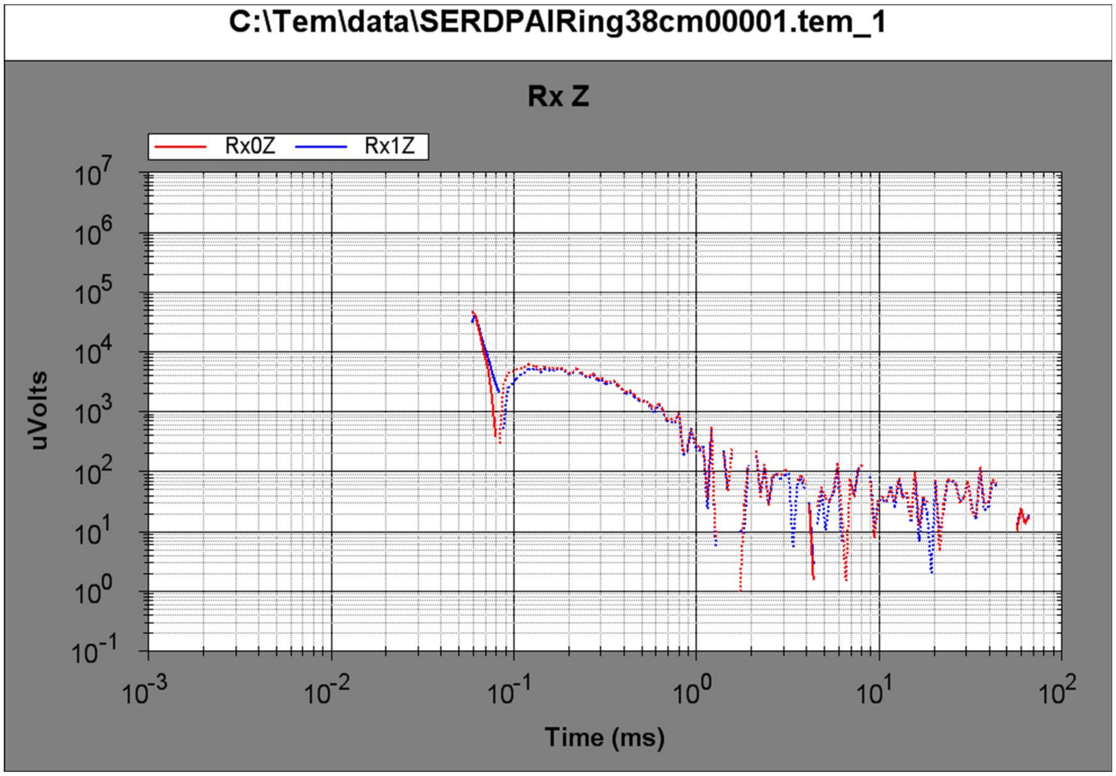

Figure 44: Comparison of hardware and software subtraction. The red curve (Rx1Z) was generated using software subtraction.

5.1.2.4 *Coupling Between Tx Loops and Rx Sensors*

During later tests we observed that there is significant coupling between the large transmitter loops and the receiver sensors. The Rx sensors are usually located near the lower sides of X and Y (horizontal axis) transmitting loops. The Tx loops are mounted on the array such that their lower sides cross just above the center of the Rx array. This geometry is even more important for a gradient receiver array because it would likely be centered directly beneath the point where the X and Y transmitter loops cross. Coupling between loops of any kind is a strong function of the spacing between the loops. Therefore, an Rx sensors in close proximity to a segment of a Tx loop will be susceptible to coupling between them. This is important because the Tx loops are large compared to the Rx loops and thus collect relatively larger signals.

Although it is often assumed that the transmitter loop is an open circuit when the transmitter is off, such is not the case. The transmitter loop has internal capacitance and it must be terminated by a damping resistor. This combination allows some small current to flow in the transmitter winding. Any current at all in that winding is likely to produce an observable signal in the receiver loop if the loops are well coupled.

The signal induced into any loop is stronger at higher frequencies. This makes higher frequency environmental EM noise particularly important. Signals such as Very Low Frequency (VLF), Low Frequency (LF) radio transmissions, as well as atmospheric noise produced by lightning are ubiquitous. Propagating signals in the VLF frequency range, 10–30 KHz, are characterized by a nearly horizontal magnetic field so they induce currents into one or both of the horizontal-axis Tx loops. These currents can couple a signal into one or more of the nearby Rx sensors, depending on the placement of the sensor with respect to the transmitter. Both the orientation of the Tx loops with respect the arriving fields, and the coupling between these Tx loops and the Rx loops is important.

To demonstrate the effect, four 3D-cube receivers were placed in a box pattern arrangement shown in Figure 45. A snapshot of background noise is shown in Figure 46. Each row in Figure 46 shows the Z, Y, and X signals from left to right. The top row shows the raw signals from the four sensors. The bottom row shows the difference signals between the six possible combinations of the four sensors.

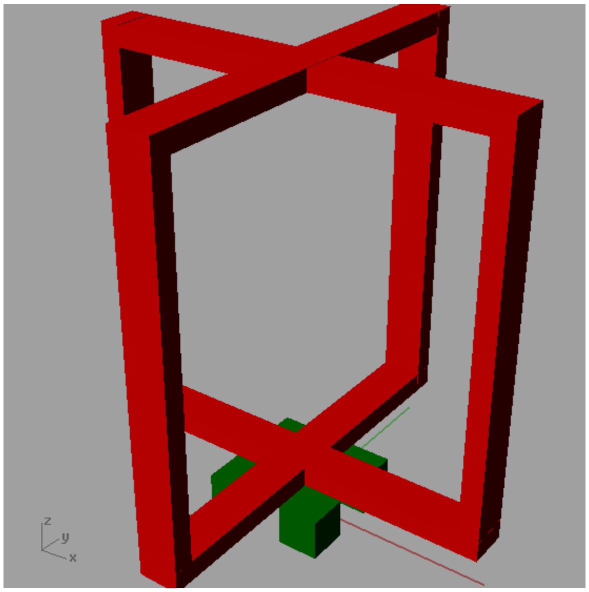

Figure 45: Arrange of transmitter loops and receive cubes for demonstration of coupling effects.

The sinusoidal signal in the Y and X components for the four sensors individually is the propagating LF signal from WWVB at 60 KHz. WWVB is located just 300 km from our measurement site in Grand Junction, CO. Since it is propagating, its magnetic field component is horizontal and thus induces currents in the two horizontal transmitting loops as well as directly in the receiver Y and X components. The top row in Figure 46 confirms that the horizontal components of the WWV signal are significantly stronger than the vertical components and that a reasonably strong signal appears in each of the horizontal receiver loops as a consequence of direct reception. These signals are expected and they do not indicate that there is coupling between the Tx loops and the Rx loops. Because the WWVB signal is a plane wave, we expect the common components of each sensor, for example the X components, to be similar if not identical in all four sensors. Thus we expect to substantially reduce the WWVB signal when common components are subtracted. And subtraction does so for the Y and X components. However, it does not do so for the Z component – in fact it in the Z-Z difference the WWVB signal level increases. Using the right hand rule to determine the field directions for currents flowing in the transmitter winding shows that a current induced into the Tx loop by the WWVB signal will additively couple into the Z-Z difference signal from pairs of sensors. The additive coupling from the large vertical transmitter loops is demonstrated in the lower left traces in the figure. This experiment shows that it is important to attempt to place gradient receiver cubes away from the transmitter windings because coupling is strongly dependent on spacing, especially for small spacings. The coupling will reduce the quality of the gradient signal.

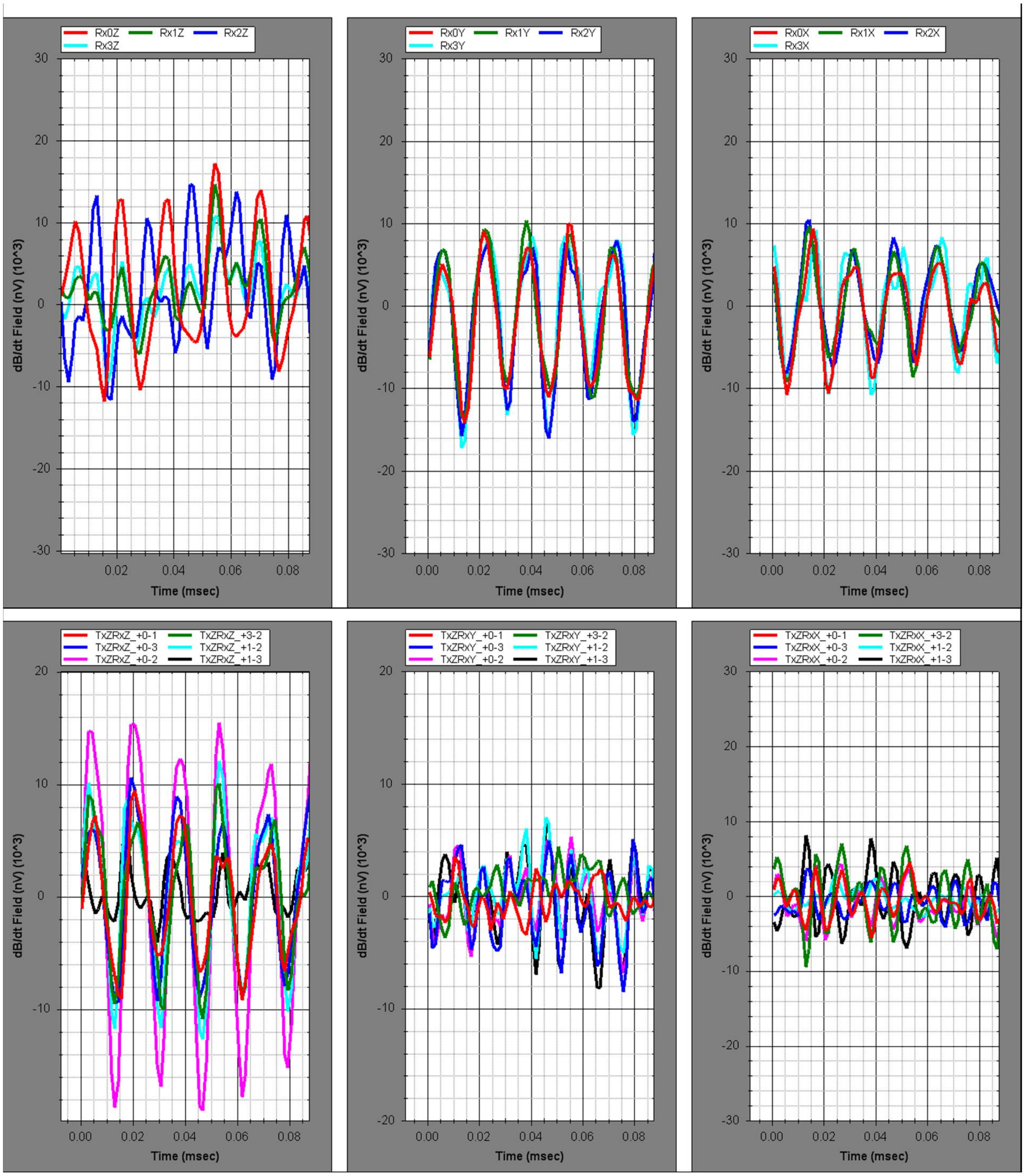

Figure 46: Signals showing strong coupling between horizontal axis transmitting loops and receiver sensors. Z components are on the left, Y components are center, and X components on the right. The upper traces are raw data from each of four sensors arranged in a box pattern. The lower traces are traces from each of the six possible combinations of two sensors, component by component.

5.1.2.5 *Improvement in Profile using Gradient Array*

A sample of a profile that would be observed if making a continuous profile, as in a dynamic survey, is shown in Figure 47. In this profile, four cube sensors were arranged in a 20cm cruciform pattern in the center of a Z-only transmitting loop. The X and Y transmitter loops were removed. A 60cm mortar was dragged at 11X depth in a 45 degree nose-down attitude under the array. The whole field results in the upper half of Figure 47 show the expected offsets in responses as individual sensors pass over the target. The figure shows the individual responses as well as the magnitude of the response from each 3D cube sensor. The slight imbalance in magnitudes is a result of the mortar being at a 45 degree nose-down attitude.

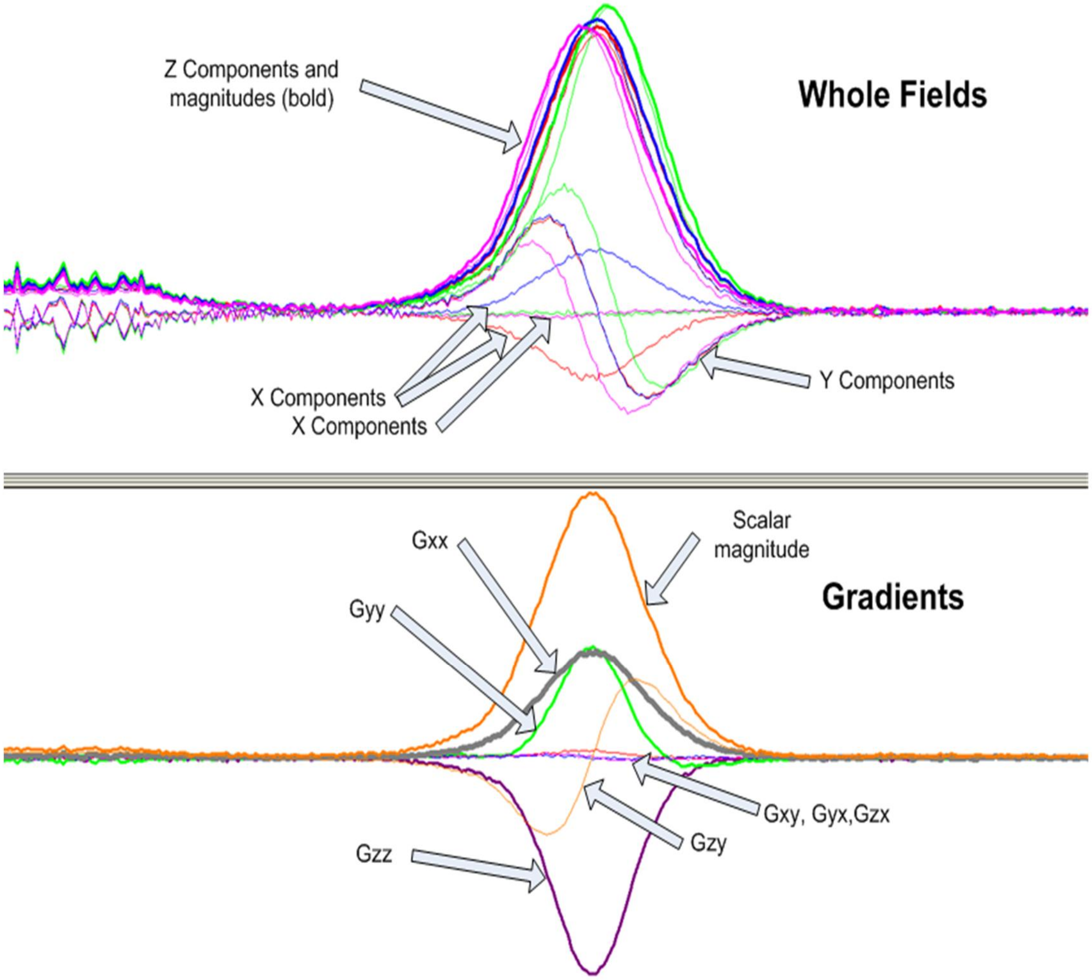

Figure 47: Comparison of profiles observed with conventional sensors and gradiometer sensors

The gradient results from the same data set are plotted in the bottom half of Figure 47. It is apparent that the gradient results exhibit a nice improvement when compared to the conventional results. There is substantially less noise and the profiles are symmetric.

We would expect these results to be better in the case of a real-life survey because in this demonstration, there was no motion noise in the Rx sensors. A comparison of profiles in a usual survey would likely show even more improvement in the gradient profiles. This demonstration was not a planned part of the results in this project so no further work was done. However, the result will be kept in mind for future applications.

6 Conclusions and Implications for Future Research

We make the following conclusions from our numerical study of finite gradients:

- Finite differences provide useful estimates of the true gradient provided that the range (*R*) to the target is greater than twice the gradient baseline distance ($R/h > 2$). At a range of twice the baseline distance, the error in the gradient anomaly is approximately 10% of the peak anomaly value.
- Our study of ***dipole tracking*****,** which is based on the use of the gradient tensor**,** as a method for rapid location of the target demonstrates that it can provide useful estimates of target position provided $R/h > 2$. At the shorter ranges ($2<R/h<3$), however, estimates of position will be semi-quantitative. Clearly, it is important to assemble our gradiometer with the smallest practical baseline distance. Given the dimension of our sensor cubes (10 cm), a baseline as small as 30cm – 35cm is possible.[13]
- The restriction on range when using differences as approximations for the gradient field means that precise extraction of target parameters must continue to be affected using conventional non-linear inversion techniques because these methods can take into account the finite dimensions of the receiver array. Clearly, however, dipole tracking remains an attractive method for real-time target detection and location.
- This numerical study was carried out using a cruciform array of 5 sensors. With this array it is easy to implement the form of electronic differencing discussed in Section 4 of this report. As a result of the study presented in Section 4, it appears that numerical differencing does as well as electronic differencing. If the gradiometer is implemented with numerical differencing of the signals, we are free to consider higher order differencing formulas. In particular, we note that the AOL data acquisition system that was used in this project is capable of supporting acquisition with 9 cubes. Therefore by using a gradiometer array consisting of 9 co-planar cubes distributed in an array such as shown in Figure 48, it may be possible to improve

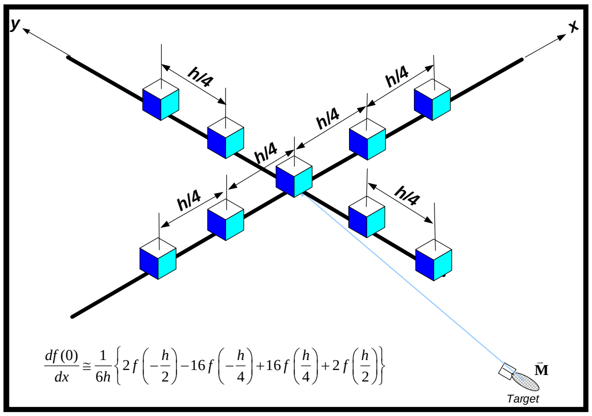

Figure 48: A 9-cube finite tensor gradiometer configuration that can be realized using numerical differencing. Such a configuration may reduce the gradient errors arising from the difference approximation.

---

[13] Because of a desire to include a sensor at the center of the array, a gradiometer with a 30cm baseline would mean that there is only 5cm clearance between adjacent cubes. At this distance there may be cross-talk between receiver cubes. Some experimentation may be required to determine the minimum acceptable clearance between sensors. This problem disappears if we remove the center cube.

gradient estimates and thereby mitigate the range *R/h >2* restriction. Additional modeling using this array would be required before we would be in a position to modify our guidelines.

- The modeling with noise suggests that the signal-to-noise ratio (SNR) for gradient signals, notwithstanding the more rapid attenuation of gradients with distance, actually improves – at least for the standard target we used in our study. This improvement is predicated on the assumption that we can reduce common-mode noise by 30-40dB. The results obtained in Section 4 suggest that we are nearly there without taking "*…extraordinary precautions to match hardware components or to measure differences in gains before making software subtractions.*" This is very encouraging.
- We have established that systematic gradient errors caused by sensor imbalance or sensor orthogonality/positioning errors are second order errors when compared with the gradient errors that arise when using a finite baseline approximation at close range. This of course assumes that reasonable care is taken in the construction of the sensor array.

We make the following conclusions from experimental measurements relative to improvement of signal to noise ratio.

- Differencing of signals from two identical sensors substantially reduces noise that is produced by sources that are distant enough to produce a noise field that is effectively uniform at the sensors.
- Differencing of signals from two sensors will sometimes, if not often, improve the SNR that is effective in making computations that use those signals.
- Sensor differences give good SNR improvement (~20 dB) for raw signal (no stacking, no windowing
- But sensor differences give less improvement for well-stacked and gated signals (e.g. 20 sec 60Hz synchronous stacking, broad windows, 8 ms decay
- Differencing of signals in this method can be done with relatively simple methods. The antennas we have already developed and the electronics that amplifies the signals are adequate to produce usable differences.
- Difference signals can be reliably produced with software, thus allowing use and storage of both the dB/dt field signals and the difference signals.
- A gradiometer sensor provides better results for dynamic profiles

These conclusions are amplified in the following table. It shows the types of noise we conclude are significantly reduced by use of a gradiometer-type sensor.

Table 1 Types of noise reduced (or not) by a gradiometer receiver

Environmental EM Noise for un-stacked, un-gated signals	Significant
Environmental EM Noise for static, well-stacked and gated signals	Insignificant
Constant ('mysterious') background signals	Significant
Non-60Hz synchronous interference (e.g. mechanical vibrations from a tractor)	Significant

Dynamic motion noise	Significant
Target/sensor geometry motion noise	Insignificant

Overall we make the following simplified conclusions and implications for future research.

- A reasonable array for gradient observations is a 20 cm, horizontal cruciform array (six gradient observations). A fifth central sensor could be needed to improve depth estimates
- The horizontal cruciform array is best used for mapping surveys with a Z-only transmitter loop
- For characterization of targets using 3D Transmitter loops:
  - A cruciform array must be physically separated from Tx loops. Therefore array design for AOL/MM/BUD 3D-Tx arrays is problematic
  - The gradient sensors do not significantly improve static measurements that are well-stacked and well-windowed.
  - The gradient sensors do not improve our ability to distinguish multiple targets with overlapping signatures
- Dipole tracking works
- Altogether, gradient sensors would likely improve dynamic mapping surveys but do not provide significant advantages for static characterization.
- Our experiments have established the need to separate a gradient array from close coupling to a horizontal-axis Tx loops in order to avoid coupling unwanted noise into the received signal. Moreover, this study has also established that the advantages of gradient methods accrue primarily to dynamic-mode target-detection surveys and not to static-mode Cued-ID surveys. Thus we observe and make a “note-to-self,” that a good target detection array would consist of one or more, perhaps even four, cruciform receiver arrays arranged inside a Z-only transmitter loop.

7 References

Barrow, B., & Nelson, H. H. (2001). Model-Based Characterization of Electromagnetic Induction Signatures Obtained with the MTADS Electromagnetic Array. *IEEE Trans Geosci & Rem. Sensing, 39*(6), 1279-1285.

Baum, C. (1999). *Detection and Identification of Visually Obscured Targets* (1 ed.). (C. E. Baum, Ed.) Philadelphia: Taylor & Francis.

Becker, A. E. (2006, November 22). Concerning the CMRR of LBL coil pairs. Berkeley, CA: Lawrence Berkely National Labs.

Bracken, R. E., & Brown, P. J. (2006). *Concepts and Procedures Required for Successful Reduction of Tensor Magnetic Gradiometer Data Obtained from a UXO Detection Demonstration at Yuma Proving Ground, Arizona.* U.S. Geological Survey. U.S. Geological Survey.

Cattech, M. K., Lee, J. M., Stanley, J. M., & Boyd, G. W. (1993). Sub-Audio Magnetics (SAM) -- A High Resolution Technique for Simultaneously Mapping Electrical and Magnetic Properties. *24,* 387-400.

Chrissan, D. A., & Fraser-Smith, A. C. (1996). *Seasonal Variations of Globally Measured ELF/VLF Radio Noise.* Stanford Dept of Electrical Engineering, Palo Alto, CA.

Das, Y., McFee, J. E., Toews, J., & Gregory, C. S. (1990). Analysis of an Electromagnetic Induction Detector For Real-Time Location of Buried Objects. *IEEE Trans Geosci & Rem. Sensing, 28*(3), 278-288.

Davis, P. J. (1994). *Circulant Matrices.* New York: Chelsea Publishing.

Frahm, C. P. (1972). *Inversion of the Magnetic Gradient Equations for a Magnetic Dipole.* Informal Report, Naval Coastal Systems Laboratory, Panama City, FL.

G&G Sciences Inc. (2008). *Advanced Ordnance Locator for Standoff Detection and Classification of Surface and Buried UXO.* Indian Head, MD: Navsea Indian Head.

George, D. C., & Snyder, D. D. (2005). Noise in Time Domain EM Systems. *SAGEEP 2005.* Atlanta, GA: Envir. & Eng. Geophys. Soc.

George, D. C., & Snyder, D. D. (2007). *A Study of the Feasibility of a Tensor TEM Gradiometer for UXO Detection and Characterization.* G&G Sciences, Inc, Grand Junction, CO.

MacInnes, S. C., Snyder, D. D., George, D. C., & Zonge, K. L. (2002). Model-Based UXO Classification Based on Static 3-Component TEM Measurements. *SAGEEP 2002.* Las Vegas, NV: Environ. & Eng. Geophys. Soc.

Macnae, J. C., Lamontagne, Y., & West, G. F. (1984). Noise processing techniques for time-domain EM systems. *Geophysics, 49*(7), 934-948.

Maxwell, E. L., & Stone, D. L. (1963, May). Natural Noise Fields 1cps to 100kc. *IEEE Trans Ant & Prop, AP-11*(3), 339-343.

McCracken, K. G., Oristglio, M. L., & Hohmann, G. W. (1986, March). Minimization of noise in electromangetic exploration systems. *Geophysics, 51*(3), 819-832.

Meloy, J. (n.d.). *What and Where is the Natural Noise Floor?* Retrieved from http://www.vlf.it/naturalnoisefloor/naturalnoisefloor.htm.

Nelson, H. H., Bell, T. H., McDonald, J. R., & Barrow, B. (2003). *Advanced MTADS Classification for Detection and Discrimination of UXO.* Final Report, Naval Research Laboratory, Washington, D.C.

Pasion, L. R. (2007). *Inversion of Time Domain Electromagnetic Data for the Detection of Unexploded Ordnance.* The University of British Columbia, Geophysics. Vancouver, B.C.: The University of British Columbia.

Pedersen, L. B., & Rasmussen, T. M. (1990). The gradient tensor of potential field anomalies: Some implications on data collection and data processing. *Geophysics, 55*(12), 1558-1566.

Reid, A. (1980). Aeromagnetic survey design. *Geophysics, 45*(5), 973-976.

Reid, A. B., Allsop, J. M., Granser, H., Millett, A. J., & Somerton, I. W. (1990). Magnetic interpretation. *Geophysics, 55*(1), 80-91.

San Filipo, W. A., & Hohmann, G. W. (1983, September). Computer simulation of low-frequency electromagnetic data acquisition. *Geophysics, 48*(9), 1219-1232.

Schmnidt, P. W., & Clark, D. A. (2006). The magnetic gradient tensor: Its properties and uses in source characterization. *The Leading Edge, 25*(1), 75-84.

Slack, H. A., Lynch, V. M., & Langan, L. (1967). The Geomagnetic Gradiometer. *Geophysics, 32*(5), 877-892.

Smith, D. V., & Bracken, R. E. (2004). Field experiments with the magnetic gradiometer system at Yuma Proving Ground, Arizona. *Proc. SAGEEP-2004.* Colo. Spgs., CO: Eng. & Env. Geophys. Soc.

Smith, D. V., & Bracken, R. E. (2004). Field experiments with the tensor magnetic gradiometer system for UXO surveys: a case history. *SEG Technical Program Expanded Abstracts* (pp. 806-809). Soc. Expl. Geohys.

Smith, J. T. (2004). Estimating Equivalent Dipole Polarizabilities for the Inductive Response of Isolated Conductive Bodies. *IEEE Trans. on Geosc. & Rem. Sens., 42*(6), 1208-1214.

Smith, J. T., & Morrison, H. F. (2002, March-April). Approximating Spheroid Inductive Responses Using Spheres. *Geophysics, 71*(2), G21-G25.

Smith, J. T., Morrison, H. F., & Becker, A. (2004). Parametric Forms and the Inductive Response of a Permeable Sphere. *Jour. Envir. & Eng. Geophys, 9*(4), 213-216.

Snyder, D. D., & Bracken, R. (1995). Development and Testing of a Tensor Magnetic Gradiometer. *SAGEEP 1995. 1*, pp. 482-492. Orlando, FL: Environ. & Eng. Geophys. Soc.

Snyder, D. D., & George, D. C. (2004). *Deployment of a Dual-Mode (EM and Magnetic) System for Detection and Classification of UXO at Blossom Point, MD.* Blackhawk Geoservices, Inc, Golden, CO.

Spies, B. R. (1988). Local noise preduction filtering from central induction transient electromagnetic sounding. *Geophysics, 53*(8), 1068-1079.

Stanley, J. M., & Griffin, S. M. (n.d.). Sub-Audio Magnetics. Miniature Sensor Technology for Simultaneous Magnetics and Electromagnetic Detection of UXO. Unpublished.

Thompson, D. (1982). EULDPH: A new technique for making computer assisted depth estimates from magnetic data. *Geophysics*, *47*(1), 31-37.

Thompson, D. (1982). EULDPH: A new technique for making computer assisted depth estimates from magnetic data. *Geophysics*, *47*(1), 31-37.

Wiegert, R., & Oeschger, J. (2005). Generalized Magnetic Gradient Contraction Based Method for Detection, Localization and Discrimination of Underwater Mines and Unexploded Ordnance. *MtS/IEEE OCEANS*, *2005*, *2*, pp. 1325-1332. Washington, DC.

Wynn, W. (1972). *Dipole Tracking with a Gradiometer.* Informal Report, Naval Ship Research and Development Laboratory, Panama City, FL.

Wynn, W. M., Frahm, C. P., Carroll, P. J., Clark, R. H., Wellhoner, J., & Wynn, M. J. (1975). Advanced Superconducting gradiometer/Magnetometer Arrays and a Novel Signal Processing Technique. *IEEE Trans. on Magnetics, MAG-11*(2), 701-707.

Appendix A: The TEM Gradient Field

In this section, we look at the response of an ideal point gradiometer to dipolar fields produced by eddy currents induced in small targets by a primary field generated by passing a current through a multi-turn loop. For ground surveys, the transmitter coil typically has dimensions of 1m x 1m with 10-30 turns of copper or aluminum wire. Current levels are typically on the order of 10 A.[14] The dipole theory for modeling the EM response of small highly conductive and permeable target such as a UXO has been published by a number of authors (Barrow & Nelson, 2001), (MacInnes, Snyder, George, & Zonge, 2002), (Smith J. T., 2004), (Baum, 1999), so we only outline that theory here in order to define our notation and to show how it can be easily extended in order to calculate the tensor gradient of the induced secondary field. The reader is referred to the papers we cite for a more detailed explanation.

The EMI response of a small isolated target characterized by very high conductivity and, perhaps, high permeability is well approximated by a point dipole whose moment **M** is determined by the amplitude and direction of the transmitter field $\mathbf{H}^{p}$ at the location of the dipole (assumed to be approximately at the geometric centroid of the target body). The target properties are embodied in a time-varying [15] ***polarizability*** tensor **P(t)**. Mathematically, the theory is summarized by the equations

$$\vec{\mathbf{M}} = \tilde{\mathbf{P}}\vec{\mathbf{H}}^{p} \qquad \text{(A-1)}$$

$$\vec{\mathbf{B}}^{s} = \mu_0 \tilde{\mathbf{G}}\vec{\mathbf{M}} \qquad \text{(A-2)}$$

where in equation A-2, $\mathbf{B}^{s}$ is the secondary magnetic induction field generated by a point dipole with magnetic moment **M** which is related to the transmitter field at the target ($\mathbf{H}^{p}$) by means of the polarizability tensor **P** using equation A-1. The factor **G**, in equation A-2 is another tensor called the dipole Green's function. EMI measurements are sensitive either to the time rate of change of the secondary magnetic induction field ($\mathbf{B}^{s}$) in the time domain, or to its equivalent Fourier transform in the frequency domain. The dipole Green's function is a simple function of position coordinates and simply describes the behavior of the dipole field at any point in space.

A.1 Indicial Notation

---

[14] The NAVEODTECHDIV AOL system uses 16T with 10A. The Z transmitter loop on the LBL system has a split transmitter loop with 22T on each loop (44T total). The transmitter loop is driven with a resonance transmitter that generates a half-sine current waveform with a peak current of approximately 15A.

[15] We choose a variation in polarizability with time because we work in the time domain. Equally valid would be a complex-valued polarizability tensor that is a function of frequency, which is appropriate for those who work in the frequency domain.

The vectors in equations A-1 and A-2 can each be expressed by their 3 components in a particular spatial coordinate system. Likewise, the tensors (i.e., **P** and **G**) are of second rank and can be expressed as a symmetric 3x3 table of components (a matrix if you will). It is convenient to rewrite equations A-1 and A-2 in terms of their indexed components as we show below. In this case, we adopt the usual summation convention (i.e., duplicated indices indicate an implicit summation over the range of the index). In rewriting equations A-1 and A-2 in indicial notation, we have also taken the time derivative of the fields so that equation A-2a is directly related to the voltage we see at the receiver.

$$\dot{M}_i = \dot{P}_{ij} H_j^p \text{; where } \dot{M}_i = \frac{dM_i}{dt} \text{ and } \dot{P}_{ij} = \frac{dP_{ij}}{dt} \tag{A-1a}$$

$$\dot{B}_i^s = \mu_0 G_{ij} \dot{M}_j \text{ ; } \mu_0 = 4\pi \times 10^{-7} \frac{h}{m} \tag{A-2a}$$

The receiver point *P* coordinates are given by the 3 values x_i and the dipole is located at position *Q* defined by the 3 values u_i. The elements of the dipole tensor G_{ij} are given by the relation

$$\begin{aligned} G_{ij} &= \frac{1}{4\pi R^3}\left(3n_i n_j - \delta_{ij}\right) \\ \text{where, } R &= \sqrt{\sum_{i=1}^{3}(x_i - u_i)^2} \text{ , } n_i = \frac{(x_i - u_i)}{R} \text{ ,} \\ \text{and } \delta_{ij} &= 0(i \neq j); \delta_{ij} = 1(i = j) \end{aligned} \tag{A-3}$$

Upon taking the derivatives of the Green's function (equation A-3) with respect to the receiver coordinates x_k we can write its gradient, a tensor of rank 3, as

$$G_{ij,k} = \frac{\partial G_{ij}}{\partial x_k} = \frac{3}{4\pi R^4}\left(\delta_{ik} n_j + \delta_{jk} n_i + \delta_{ij} n_k - 5 n_i n_j n_k\right) \tag{A-4}$$

In equation A-2a, the components of the dipole moment M_j (and its time derivative) are functions of the primary field and hence the coordinates of the transmitter location. Therefore, to find the gradient of the secondary field, we need only know the gradient of the dipole Green's function, which we have written in equation A-4. The theoretical gradient field due to the induced dipole located at point *Q* with coordinates u_i is given by

$$\dot{B}^{s}_{i,k} = \mu_0 \, G_{ij,k} \, \dot{M}_{j} \tag{A-5}$$

where the elements of the 3rd rank tensor $G_{ij,k}$ are given in equation A-4.

We can combine equations A-5 and A-1a to get the final modeling equation that relates the gradient of secondary field at the receiver point (P) to the target parameters embodied in the notion of a time variation of a polarizability tensor characterizing the target (P_{ij} and its time derivative), and the amplitude and direction of the primary field which induces eddy currents in the target (H^{p}_{i}). The 3rd rank Green's function tensor (equation A-4) governs the spatial behavior of the resulting tensor gradient field.

$$\dot{B}^{s}_{i,k} = \mu_0 \, G_{ij,k} \, \dot{P}_{jl} \, H^{p}_{l} \tag{A-6}$$

In this explanation, we have omitted for brevity the relation for the primary field ($\mathbf{H}^{p}$) at the target location. This can take many forms depending on the exact shape of the transmitter. In any case, it is the same relation whether we choose to measure fields with an induction loop or gradients with either an ideal gradiometer receiver or an array of induction fields that approximate differences proportional to the required spatial derivatives. In the next section and in subsequent sections where we compare finite gradients with theoretical gradients, we have used equations A-4 and A-6 together with an appropriate relation for computing H^{p} from a finite current loop to calculate the theoretical gradient.

A.2 Target Polarizability

The polarizability tensor P_{ij} introduced in equations A-1 and A-1a provides a linear constitutive relationship between intrinsic properties of the target and the magnetic polarization, which we can measure indirectly through the magnetic induction field that it generates. In the time domain, polarizability is a real symmetric tensor. In general, therefore, it is characterized by six independent elements, the other three being dictated by the tensor's symmetry property. Because it is real and symmetric, there exists a coordinate system that we call the ***principal coordinate system*** in which the polarizability tensor is expressed as a diagonal tensor. In the principal coordinate system, therefore, the polarizability tensor is defined by three time-varying functions that are the diagonal elements of tensor and are in fact the tensor's eigenvalues. Mathematically, the elements of the polarization tensor in its principal system can therefore be expressed by

$$\dot{P}'_{ij}(t) = \begin{bmatrix} \dot{p}'_1(t) & 0 & 0 \\ 0 & \dot{p}'_2(t) & 0 \\ 0 & 0 & \dot{p}'_3(t) \end{bmatrix} . \tag{A-7}$$

In coordinate systems other than the principal coordinate system, the polarizability tensor can be expressed in terms of its three elements in the principal system through an orthonormal coordinate transformation $\mathbf{U}(\phi,\theta,\psi)$, where the three angles (ϕ,θ,ψ) are often termed the *Euler Angles*. The transformation relation between the tensor in it principal coordinate system to its expression in any other coordinate system is

$$\tilde{\mathbf{P}} = \tilde{\mathbf{U}}^{\mathbf{T}}\tilde{\mathbf{P}}'\tilde{\mathbf{U}} \text{ ; where } \tilde{\mathbf{U}}^{\mathbf{T}} \text{ denotes matrix transpose } . \qquad \text{(A-8)}$$

Using indicial notation (with implied summation over repeated indices), equation A-8 is equivalent to the equation

$$P_{ij} = U_{ki} P'_{kl} U_{lj} \ . \qquad \text{(A-8a)}$$

In using the polarizability concept, the properties of the target are totally expressed by its three principal polarizability components $p_i(t)$. The Euler angles (ϕ,θ,ψ) describe the attitude of the principal coordinate system with respect to the measurement system and therefore are not properly considered to be target parameters.

For the purpose of the numerical experiments and examples, we will use an approximation to the polarizability of a conductive and permeable prolate spheroid having a diameter of 60mm and a length of 180mm (3:1 aspect ratio). The approximation is based on work published by Smith, et. al. (Smith & Morrison, Approximating Spheroid Inductive Responses Using Spheres, 2002) that establishes a basis for approximating the response of moderate oblate or prolate spheroidal conductive and permeable shapes based on the response of conductive permeable spheres. Using the parametric relationship for the polarizability transient of a sphere (Smith, Morrison, & Becker, Parametric Forms and the Inductive Response of a Permeable Sphere, 2004), which is reproduced below, the 3 polarizability transients of the 60mm baseline target model are given in Table A-1. The parametric relationship for the transients is

Table A-2: Parameters for the principal polarizability transients approximating a conductive permeable prolate spheroid target diameter 60mm and length 180mm. The relative permeability of the body is 180 and its conductivity is 10^8 S/m.

Axis Index	**κ (cm^3)**	**α (μs)**	**β**	**γ (1/μs)**
1	3349.21	776.11	1.337	7.33E-07
2	1363.97	86.23	1.337	6.60E-06
3	1363.97	86.23	1.337	6.60E-06

Polarizability		Time Gate (μs)	
1	973	400	900
2	247	400	900
3	247	400	900

$$\dot{p}(t) = k\left[\gamma + \frac{\beta}{2\left(\sqrt{\alpha t}+t\right)}\right]\left(1+\sqrt{\frac{t}{\alpha}}\right)^{-\beta} e^{-\gamma t}\ . \qquad \text{(A-9)}$$

The objective of our modeling here is to determine the specifications for a gradiometer that will provide information that is useful for the UXO problem. Therefore, rather than model the full time variations in the gradient field, we have selected a time window that is typical of that used in commercially available TEM systems such as the Geonics EM-61 (e.g., 400-900 us). Using the parameters in Table A-1 and integrating equation A-9 over the gate interval yields the three principal polarizability constants for the target gate. These numbers correspond to the “3 beta values” mentioned by Nelson et. al. (Nelson, Bell, McDonald, & Barrow, 2003). At the bottom of Table A-1, we have tabulated the 3 values of polarizability for our spheroid test target corresponding to a standard EM61 time gate.

A.3 Units

Equation A-6 is the basic response equation that relates the gradient of the secondary induction field (B^s) to the primary field at the target (H^p), and the polarizability rate tensor d*P/dt*. From an analysis of the dimensions involved in equation A-6, we can determine that when induction field is measured in units of Teslas (T), the polarizability tensor must have dimensions of m^3/s in order that the units in equation A-6 balance on each side.[16] But our EM instruments do not directly measure the induction field or its rate. Instead, they measure voltages or, perhaps, voltage differences with the voltage proportional to the time rate of change of flux which has units of T-m^2/s = Volts. Thus, in order to change the values of secondary induction field gradient into an equivalent voltage gradient, we need to calculate the time rate of change of flux ($d\Phi/dt$) through each receiver coil. For sufficiently small receivers, we can assume the induction field is approximately constant over the area of the receiver and hence, to the extent that this is a good assumption, the voltage measured by a particular receiver is simply the product of the receiver’s effective area (A_e) of the receiver (turns x area x gain) times the time rate of change of the component of the field normal to the plane of the receiver $V_s \cong A_e(\hat{\mathbf{n}}\cdot\dot{\mathbf{B}}_s)$. Therefore, we can turn our calculated field gradients into measured voltage gradients simply by multiplying the theoretical gradients by the effective area of the receiver(s) m^2. We report the voltage gradients we calculate in units of (□V-□□s) /m by assuming an effective area of 100 m^2, the effective area of the 3 loops on the AOL receiver cubes, as the area of gradiometer receiver loops. The strange unit of (V·s) arises because we have defined and used polarizability values (see bottom of Table A-1) that are the integration of the polarizability rate curve defined by equation A-9 over a 500□□s time gate.

---

[16] In table A-1, we have provided polarizability parameters in units of cm^3 and μs. Note that 1 cm^3/ μs = 1 m^3/ s.

A.4 Synthetic Profiles and Maps

As we mentioned in section A.1.2 above, the gradient tensor of the secondary magnetic induction field (equation A-6), is a second rank symmetric tensor. Therefore, in general it has 6 independent elements. In order to summarize the spatial behavior of these elements we have developed a summary plot containing 15 separate plots. Figure A-1 is an example of the summary plot for a short profile (x = 0; -2.6<y<2.6; z = 0) computed over our standard target when it is buried at a depth of 1m. The vertical scale on the plots has been companded (i.e., compressed) using the algorithm

$$V_c = 20Log_{10}\left(e\right)\sinh^{-1}\left(\frac{V}{2V_0}\right), \tag{A-10}$$

where V_c = companded result, V = input value, and V_0 = reference value.

Gradiometer Summary Plot: Theoretical Gradient (60mm ND @ 1m)
(Companded Scale w• 20dB tick marks relative to 100(μV·μs)

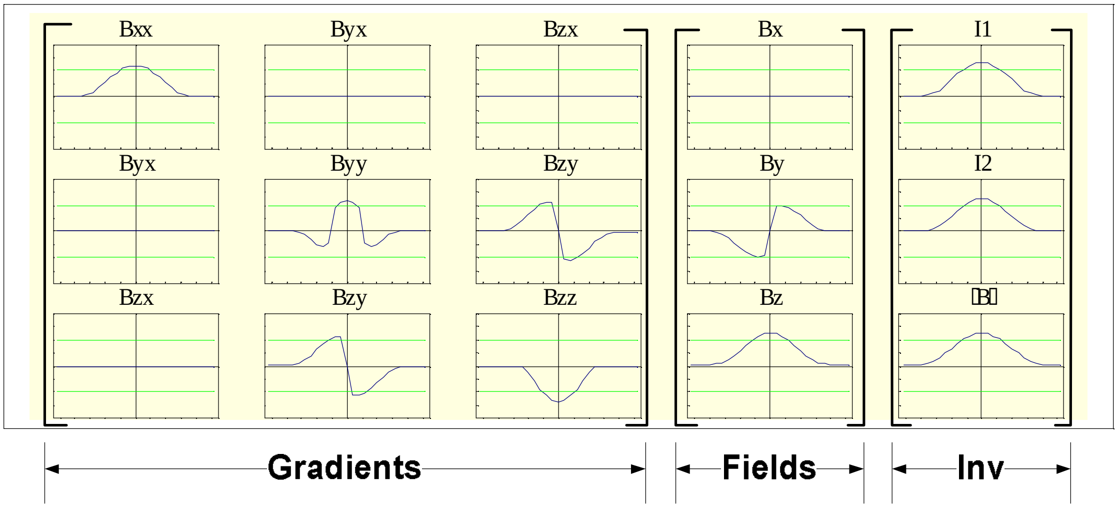

Figure A-1: Summary plot showing theoretical TEM gradient profiles over a 60mm test target buried 1m beneath the plane of the transmitter coil. The profile ranges from –2.6m to + 2.6m. The vertical tick marks represent a companded scale that approximates a bipolar logarithmic scale for signal levels greater than the indicated threshold [100 (µV·µσ)]. The green lines are

The green lines in Figure A-1 represent a signal level that is 40dB above (below) the indicated threshold value. Signals with peak amplitudes of 30dB or more above the noise-level are generally regarded as "interpretable" using physics-based modeling methods. Therefore, at noise-levels on the order of 100 µV·µs or less, our physics-based interpretation methods should work well.

Figure A-1 also identifies 3 column groups:

1. **Gradients –** This group represents the 9 gradients of the secondary field gradient tensor. As we mentioned previously, the tensor is symmetric and plot elements show that symmetry. Note also that the elements along the main diagonal sum to 0.
2. **Fields –** These 3 profiles represent the components of the vector field along the simulated profile.
3. **Invariants –** Vectors and tensors have invariant properties -- scalars values that are independent of the coordinate system in which the vector or tensor is expressed. The amplitude of a vector field, for example, is invariant under coordinate transformations. Likewise, a tensor of the second rank has 3 invariants. In the case of the gradient field, only two of the invariants are useful.[17] The 3 invariants, I_1, I_2, and |**B**| (column 5 in Figure A-1) are derived from the gradient tensor and the vector field (Pedersen & Rasmussen, 1990). The definitions of the invariants in terms of elements of the gradient tensor (*dB_{ij}/dt*) and vector field components (*dB_i/dt*) are shown in equation A-11 below:

$$
\begin{aligned}
I_1 &= \left(\dot{B}_{xx}\dot{B}_{yy} + \dot{B}_{yy}\dot{B}_{zz} + \dot{B}_{xx}\dot{B}_{zz} - \dot{B}_{xy}^2 - \dot{B}_{yz}^2 - \dot{B}_{xz}^2\right)^{\frac{1}{2}} \\
I_2 &= \left(\dot{B}_{xx}\left(\dot{B}_{yy}\dot{B}_{zz} - \dot{B}_{yz}^2\right) + \dot{B}_{xy}\left(\dot{B}_{yz}\dot{B}_{xz} - \dot{B}_{xy}\dot{B}_{zz}\right) + \dot{B}_{xz}\left(\dot{B}_{xy}\dot{B}_{yz} - \dot{B}_{xz}\dot{B}_{yy}\right)\right)^{\frac{1}{3}} \\
\left|\dot{\mathbf{B}}\right| &= \sqrt{\dot{B}_x^2 + \dot{B}_y^2 + \dot{B}_z^2}\text{; where} \qquad \text{(A-11)} \\
\dot{B}_i\Big|_{i=\{x,y,z\}} &= \text{ The time derivative of the secondary induction field.} \\
\dot{B}_{ij}\Big|_{i,j=\{x,y,z\}} &= \text{ The gradient of the induction field (e.g., } \dot{B}_{xy} = \frac{dB_{xy}}{dt} = \frac{d}{dt}\left(\frac{\partial B_x}{\partial y}\right)\text{)}
\end{aligned}
$$

In equation A-11 we have taken the square root and cube root in the expressions for I_1 and I_2, respectively, so that the units of the invariant quantities will remain the same as the elements of the gradient tensor (i.e., (µV-µs) /m).

The summary maps have a layout that is identical to that of the profile summary display with the profiles replaced with the corresponding color map display. In all of our model computations, we have defined a standard display area encompassing the x and y coordinate ranges $-2.6<x<2.6$, and $-2.6<y<2.6$ with coordinate values in meters. As in the profile summary plots, we again plot companded data in order to provide a better indication of the dynamic range of the anomalous values. Figure A-2 is an example of the standard map display, and it corresponds to the same model shown in Figure A-1.

---

[17] We have already noted that the trace of the gradient tensor (i.e., the sum of its diagonal elements) always sums to 0. This is a property of all potential fields and arises from the fact that potential fields are irrotational (i.e., $\nabla \times \dot{\mathbf{B}}_s = 0$). The trace of the gradient tensor is one of the invariants.

A.5 Comments

Although we have yet to address the practical issues of approximating gradients by measuring the differences in the field components over finite spatial distances, the model data in Figures A-1 and A-2 provide us with an order of magnitude for the sensitivity required not only to detect targets of interest but also to characterize or otherwise identify these targets. The standard target, whose parameters we tabulated in Table A-1, approximates a 60mm mortar. Generally speaking, when buried at a depth of 1m (say, 75cm below ground level) a 60mm mortar is near the threshold of detection for most EM systems. Therefore, the results from the theoretical gradient models for this target indicate that gradient signal levels that are on the order of ±1000 µV-µs/m, or equivalently order ±2 µV/m in terms of average voltage at the gate center instead of an integrated gate value should be interpretable.[18]

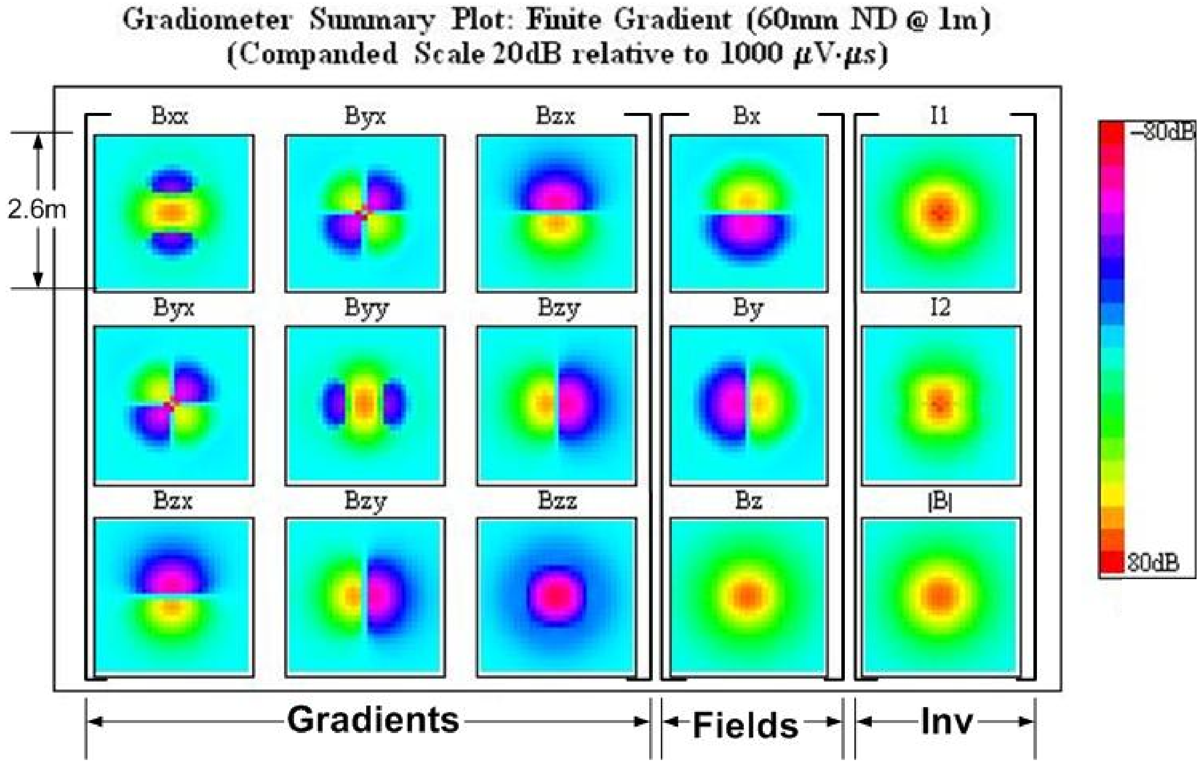

Figure A-2: Summary plot showing theoretical TEM gradient maps over a 60mm test target buried 1m beneath the plane of the transmitter coil. The maps cover a 5.2m x 5.2m area centered over the target. The color scale represents the companded values and approximates a bipolar logarithmic scale for signal levels greater than the indicated threshold [100µV·µs].

---

[18] The reader can easily convert this threshold to a simple voltage gradient by recalling that the responses used to plot our curves arise from integrating along the received dB/dt voltage transients over a time window of 500µs that is centered at a time delay after current shut-off of 650 µs. Thus if we divide (µV· µs)/m by 500, we end up with µV/m, the average receiver voltage at 650µs.